Fundamental Studies on Metal-Organic Framework Functionalization and Reactivity

by

Kyle A. McDonald

A dissertation submitted in partial fulfillment
of the requirements for the degree of
Doctor of Philosophy
(Chemistry)
in the University of Michigan
2017

Doctoral Committee:

Professor Adam J. Matzger, Chair
Professor Bart M. Bartlett
Emeritus Professor David W. Gidley
Professor Anne J. McNeil

Kyle A. McDonald

kylemcd@umich.edu

ORCID iD: 0000-0001-8379-5475

DEDICATION

To my family, you have given me a lifetime of love, support, and laughter. You are all God-sent and enrich my life.

And

For the 49 angels who lost their lives on June 12, 2016.

ACKNOWLEDGEMENTS

It is not news to anyone in the Chemistry Department at the University of Michigan, but Prof. Adam J. Matzger is bluntly honest in the best way possible. Over the last few years I have come appreciate and respect this quality. As a mentor, Prof. Matzger (hereafter referred to as "Matzger" – a colloquially accepted way of addressing him) has helped me to become a better scientist, thinker, learner, and person in my very short time here. His honesty (and good sense of humor) enabled me to identify my strengths and weaknesses at an early stage. This allowed me to focus on strengthening my approach to science. In addition, Matzger has always been very helpful with project/experiment design, writing, presenting, etc. Matzger has been very supportive of my career goals and always pushed me to strive for excellence. Matzger has allowed me to work on grant writing and help develop projects in the lab; an invaluable skill set we develop in the Matzger lab. Matzger is truly a great mind in science and I credit all of my future accomplishments to my great experiences as a graduate student here in the Matzger Lab.

I'd like to also thank my committee members: Prof. Anne J. McNeil, Prof. Bart M. Bartlett, and Prof. David W. Gidley. I am very thankful for the support and helpful guidance of my committee. It was always very easy to drop by Prof. Bartlett or Prof. McNeil's office with a question. While not part of this thesis, I have had the pleasure of working with Dr. Gidley on characterization of heterogeneous pore space and pore-size evolution during gas adsorption using positron annihilation lifetime spectroscopy (PALS). This experience has taught me a great deal. Our frequent meetings and intellectual conversations over Maxwell House Coffee were something I looked forward to, and helped me to learn how to ask myself important research questions. During the last few months of my PhD, I have been working with Prof. McNeil, who has made it her mission to increase diversity and inclusion among students in the LGBTQ+ community in the chemistry department. I truly admire you and am very thankful for the efforts you have made and grateful for having been a part of this mission.

It goes without saying, but we in the Matzger Lab are extremely silly and overly affectionate. The atmosphere created by the sum of current and former labmates has made it a great place to call work over the last few years. I would like to thank all of the Matzger Lab (past and present): Laura, Jeremy, Ananya, Ping, Ly, Rachel, Leah, Brianna, Nipuni, Nilanjana, Yiyang, Ramanpreet, Matias, Jon, LiZi, Rosalyn, Jialiu, Kortney (aka: Vanna White), Jake, Greg, Ren, Chengcheng, Saona, Derek, Shantel, Ryan, Andy, and Ri. Of course, very special thank you to Antek for all of his help over the last several years, without you the Matzger Lab would certainly not function the same. Thank you for always taking the time to help me with research questions, instrument/computer software issues, etc (the list could go on and on). I would like to finally extend a very special thank you to my labmate and friend, Rosalyn Kent. Particularly over the last few years, you have been a rock for me and you have helped get me through the tough times with constant laughter. I'd like to thank Jim Windak (Mass Spec/GPC Services, etc.) and Dr. Jeff Kampf (crystallography). I would like to extend my endless thanks to all of the "1500" staff for their constant help and support, especially Liz and Cornelius.

The Chemistry Department here at the University of Michigan has been a great place to be over the last few years. I want to thank my fellow graduate students; you have made this experience fun. Special thanks to Melissa, Amanda, Eric, Bryant, Emilia, Ahlam, Bradley, Kim, Jimmy, Justin, Hilary, Matthew, Becky, Ariana, Andy, Jessi, Kayla, Frances, Yvonne, Chen, Sam, Nicole, Stephen, Amy, Danielle, Jordan, Cassie, Casey, Matt, Wendi, and Pablo. Of course, I'd like to extend a VERY special thank you to Kendra. She was my first friend in Michigan and we haven't stopped laughing ever since. Whether it's good, bad, or ugly, Kendra has been a great friend all the way through and will continue to be a cherished friend that I admire ("you are smart, you are kind, you are …").

I have many friends outside of the department (but in Rackham) to thank. I would like to extend a special thank you to Autumn, Aeriel, Nina, Ciara, Lauren, Corine, Princess, Aixa, Oleta, Christian, Yasmine, Nkemka, Arcelia, Crystal, Tasha, and Asya; you girls have kept me sane at times where I needed it most. In addition, I have learned so much about the importance of diversity, culture, understanding, and friendship from you all and will continue to cherish our friendships.

I wouldn't have made it through graduate school if it wasn't for my Detroit family: Bryce, James, Derek, crazy Derek, Jon, Jimmy, Tom, Matt, Ken, Janinne, Frank, Dante and Ashley (best brunch hosts in Detroit), Jason, Scott, Anthony, Chris and Tony, Christine and Dawie, and of course Trevor. You all keep my "work-life balance" in check and keep me from feeling homesick.

I would like to also say a special thank you to my Organic Chemistry Professor from my undergrad (whom I have kept in touch with) Prof. Eric Crumpler. In addition, I would like to acknowledge the two professors who allowed me to begin my research experience during undergrad: Prof. Michael Zaworotko and Prof. Brian Space. The experiences I had in your labs were instrumental in my early development as a scientist and laid the foundation for my future here at Michigan and beyond.

Since accepting my job offer from Dow Chemical I have had the pleasure of getting to know some amazing people in the "Dow Family". This has made it really easy to begin transitioning into my next journey and I am forever in debt to my very good friend Lidaris for bringing my partner and me into your home and introducing us to so many great people in the area. Special thanks to: Lidaris, Beata, Dan, Cory, Matt Belowich, Matt Remmy, John, Anna, Randi, Andrea, and Vanessa.

This brings me to my final, but most significant THANK YOU. Thank you to my family: especially, Mom, Dad, Taylor, Melissa, Mark, Evelyn, Ethan, Harrison, Dawn and Mariann (best friends and partners in life), Porfirio and Elisa, Titi Angie, Mike, Alexis, Titi Myra, Titi Maritza, Tio Rafa, Titi Lala, Titi Felicia, Tio Toni, Mema Joyce, Pa Charles, Pa Norton, Gladys, Carlos, little Carlos (C4), Stacy, Titi Betti, Tio Chucho, Maria, Hiram, Alejandro, Lara, Gabriel, Julian, Berta and Carlos, The Millers, Aunt Brenda and Uncle Kenny (and family), Aunt Sherron (and family), and Aunt Vicki (and family). You have all given me the most wonderful environment to thrive, grow, and learn in; I could not have asked for better. Thank you for all of your constant support and love throughout the years. You have been integral in my growth as a person and I am forever thankful for you loving me for who I am. Thank you mom and dad for always believing in me, supporting in my dreams, and accepting me for me; you gave me the power to accept myself. Finally, a very special thank you to my partner in life, Hussein

“Sammy” Chouman and our amazing dog Lilly; you make all the hard work pay off and I look forward to our life together.

TABLE OF CONTENTS

LIST OF FIGURES

LIST OF TABLES

ABSTRACT

Metal-organic frameworks (MOFs) are an emerging class of porous materials that have been widely studied over the last three decades and have been proposed for numerous applications. Recently, the hybridization of MOFs and polymers has shown potential to combat some of the major drawbacks of this class of materials. Their structural modularity makes MOFs ideal for producing functional hybrids with enhanced properties and improved stability/processability. However, polymer intrusion into the internal pore space is often problematic in some cases for enabling optimal accessibility of the desired high surface area of the MOF.

A core-shell approach is applied to produce MOF-polymer composites where the growth of polymer is restricted to the outer shell, leaving a pristine, high surface area internal core (chapter 2). The tethering of initiators by post-synthetic modification from amine groups on the IRMOF-3 shell enables the selective growth of polymer localized to the outer shell of an IRMOF-3@MOF-5 crystal. Spatial confinement of initiators leads to composites having high internal surface area. Although the hydrolytic stability is marginally increased, defects in the shell can allow for direct entry of guests.

A second facile approach to MOF-polymer hybridization is explored wherein polymer is evenly distributed throughout the crystals of MOF-5, eliminating problems with shell defects (chapter 3). Simply heating neat styrene with MOF-5 initiates the grafting of polystyrene with polymer incorporation precisely controlled by varying reaction time. Polystyrene grafting alters the physiochemical properties of MOF-5, evident by examining the solvatochromic behavior of dye molecules adsorbed into the MOF-5-PS composites. Furthermore, the CO_2 adsorption capacity is increased in certain composites relative to MOF-5. Polymer incorporation increases the hydrophobicity of these hybrids enabling them to maintain their high surface areas after 3 months in 53 % relative humidity.

Chapter 4 introduces an emerging application of MOFs and coordination polymers (CPs) as energetic materials. These materials show promise as a new class of tunable energetics for applications from munitions to mining. Among the reported energetic MOFs and CPs, there are few examples of nitro-aromatic linkers, motifs consistent with more traditional energetics. The thermal decomposition pathways of extensively nitrated MOFs shows that deflagration transforms cubic MOFs into anisotropic carbon structures that contain highly dispersed metal. The mechanism of thermal decomposition is investigated through decomposition gas analysis, high-speed imaging, and chemical characterization of the decomposition product. The importance of intimate mixing for the efficient anisotropic decomposition of CuNbO-1 highlights the utility of the pore space and regularity in the MOF.

A new method for the synthesis of energetic MOF composites using the same principle of intimate molecular mixing is described in chapter 5. This method for producing energetic MOFs enables the use of the vast library of highly fuel-rich non-energetic MOFs for the adsorption of oxidants resulting in a molecularly mixed fuel and oxidant. The adsorption of oxidants tetranitromethane (TNM) and hexanitroethane (HNE) into MOF-5 results in composites with high heat released upon decomposition, neutral oxygen balances, and suppressed vapor pressure of the volatile oxidant guest. Moreover, the prototype system (MOF-5-TNM and MOF-5-HNE) results in primary energetics, materials very sensitive to impact. This method enables the safe transportation of the individual components, which can be combined at the source generating the energetic composite.

Chapter I

Introduction to Porous Materials

Porous materials, including activated carbon,[1] silica gel,[2,3] activated alumina,[4] and zeolites[5-7] are some of the oldest and most well studied adsorbents, and are still in broad use today. Metal-organic frameworks (MOFs), a subset of coordination polymers (CPs), are a relatively new class of porous solids that have seen increasing attention for their tunability and modularity.[8,9] This thesis discusses fundamental studies on the functionalization and reactivity of MOFs and coordination polymers (CPs) through polymer hybridization.[10,11] In addition, this thesis highlights a new application of MOFs and CPs as energetic materials.[12,13] To contextualize this work, classical sorbents are initially discussed.

1.1 Activated Carbon

Carbonaceous adsorbents, collectively referred to as activated carbon, are porous materials having internal surface areas in the range of ~400-3000 m^2/g.[1,14] These materials are comprised of a heterogeneous porous structure (macropores, mesopores, and micropores), which contain very small graphitic crystallites mixed with amorphous carbon. Historically, the use of activated carbons and charcoals dates back to as early as 1550 B.C.; however, the first modern industrially manufactured activated carbon was not until in the early 1900s.[1] During the first several decades of the 20th century, activated carbon was heavily used for water purification[15,16] and the purification of pharmaceuticals.[17] Broadly, activated carbons can be produced starting with nearly any carbon-containing material, such as wood and coal.[1] These raw materials undergo either physical or chemical activation to produce the activated carbon.[18,19] The particular

method of activation employed influences factors such as pore sizes, distribution of pore sizes and if surface oxidation is present; this in turn affects the properties of the activated carbon.[1] Physical activation or gas activation involves pyrolysis of the starting material under either an inert or oxidizing atmosphere.[1,19] In chemical activation, the starting material is impregnated with dehydrating agents, such as zinc chloride or phosphoric acid and subsequently heated.[1,18] The varying activation methods result in activated carbon with differing pore size distribution and surface properties.

Hydrophobic surface properties and a high number of micropores present in activated carbon give these materials unique adsorption properties that are widely used in the chemical industry for a variety of applications, namely as molecular sieves,[20] decolorizing agents,[21] and catalysts.[22,23] Activated carbons with fine pore sizes are typically used for gas separation specifically for separations of H_2 from CO_2/CH_4.[24,25] This dates back to the introduction of the first pressure-swing adsorption plants in the 1960s.[1,26] Other commercial applications of activated carbon in the area of gas separation and storage include trace impurity removal of contaminated gases by temperature swing adsorption such as odor forming agents, solvent vapors, and organic impurities and purification of nitrogen from air using a class of activated carbons known as carbon molecular sieves.[1] Another major area for the commercial application activated carbons is the use of these materials as catalysts for redox reactions and as supports for heterogeneous catalysis.[22,23] The catalytic activity of activated carbons is based on lattice vacancies on outer edges of graphitic layers and surface functionality, such as carbonyl groups, carboxyl groups, and hydroxyl groups, which can participate in redox chemistry.[1] The pore structure of activated carbons and their surface areas have enabled the generation of a class of industrially relevant heterogeneous catalysts with a high dispersion of noble metal active sites; for example, palladium on activated carbon for hydrogenation reactions.[27]

1.2 Activated Alumina and Silica Gel

Porous transition metal oxides, including activated alumina,[4] silica,[2,7] and zeolites[5,7] (discussed in section 1.3), remain some of the most widely used and industrially relevant porous materials today. Activated aluminas are useful for a variety

of applications including adsorbents, desiccants, and catalysts as well as catalyst supports.[4] Activated alumina is typically prepared by heating bayerite, a well-defined crystalline form of aluminum trihydroxide, in a furnace at high temperatures (typically between ~300 °C and 1500 °C).[28] The activation process results in a material with surface areas ~300 m^2/g.[4] Post-treatments of the activated product are often used to enhance the properties of the material for a targeted application.[29,30]

Silica gel is the synthetic form of silica (SiO_2), which is composed of microporous voids made up of silicate micelles.[2,3] These silicate micelles can be between 2 nm and 10 nm in diameter and form a randomly oriented series of channels resulting in a material, which possesses surface areas typically in-between 300 – 1000 m^2/g.[2] Silica gel typically contains tetrahedrally oriented SiO_2 moieties in the interior and a hydroxylated outer surface, which, in addition to the high porosity, results in a material which is suitable for a range of applications including adsorbent applications,[31,32] stationary phases in chromatography,[33,34] and catalyst supports.[35,36] These materials have been commercialized since the early 1900s and are typically prepared by neutralizing sodium silicate (or some other alkali metal silicate) with a strong acid.[2] This initiates a polymerization reaction, forming silicate micelles that make up silica gel. Subsequent to the polymerization step, gelation occurs, and crosslinking of the silicate micelles results in the final silica gel product, which then undergoes a drying step using, in some cases, supercritical CO_2.[2] The surface area, influenced by the size of the micelle, and surface chemistry (i.e.: degree of hydroxylation) can be attributed to the extensive use of silica gel in industry for applications including desiccants, adsorbents, coatings, electronics, and catalysts.[2,3]

1.3 Zeolites

Synthetic zeolites represent a large portion of industrial adsorbents and catalysts today. Zeolites are crystalline three-dimensional microporous frameworks constructed from tetrahedral $[SiO_4]^{4-}$ and $[AlO_4]^{5-}$ units.[5] The oxygen atoms are shared between two tetrahedral metal centers in the crystal structure. These porous aluminosilicate materials encapsulate water molecules and cations that balance the framework charge and can be readily exchanged.[5,7] The basic building unit for many zeolite structures is known as the

sodalite unit, or β–cage, which consists of 24 $[SiO_4]^{4-}$ and $[AlO_4]^{5-}$ units linked together to form a truncated octahedron. Other cavities commonly observed in zeolite structures are the cuboctohedron and truncated cuboctohedron.[7] The regular arrangement of the pores, their thermally and chemically stable structures, tunable hydrophilicity/hydrophobicity, and acidity has resulted in the use of zeolites for a variety of applications from adsorbent materials and desiccants to catalysts.[5,6,37] The discovery of the naturally occurring zeolite stilbite in the mid-1700s initiated a large interest among academic researchers for their exchangeable cations and ability to act as adsorbents and desiccants. The first definitive synthesis of a zeolite by Barrer in the late 1940s has subsequently led to the synthesis of zeolites A, Y, and X, which have significant commercial relevance.[7,38,39] These early synthetic examples of zeolite frameworks quickly lead to vast commercial utilization during the 1950s. The physiochemical properties of zeolites can be tuned by the Al/Si ratio that makes up their frameworks.[5] Also, the number of rings that make up the windows can change the geometry of the pore and influence the transport of guests through the framework; this becomes a key feature of these materials in shape selective catalysis.[7,37] The structural variances of zeolites also have an effect on the adsorption properties of these materials, which are highly utilized in industry as molecular sieves and ion exchangers.[37] Moreover, utilization of zeolites in membrane-mediated separations by incorporation into mixed matrix membranes has enabled coupling of the high selectivity and permeability of zeolites with the processability of amorphous polymers.[37]

1.4 Discovery and Design of "Infinite Polymeric Frameworks"

Over the last few decades there has been an increasingly growing interest in the synthesis and design of MOFs, also referred to as microporous coordination polymers (MCPs) or porous coordination polymers (PCPs; although these terms are used interchangeably at times, there are some important distinctions[40]), as ideal candidates for a range of applications including gas storage,[41] separations,[42] heterogeneous catalysts,[43] ion exchange, energetic materials,[44,45] etc. MOFs, a sub-class of CPs, are composed of metal nodes or clusters connected to organic bridging linkers to form a regularly ordered two or three-dimensional crystalline material.[8,40] The vast interest in these materials is

primarily due to their highly modular Nature., which can be composed of an assortment of metal ions or clusters and a wide range of organic linkers with varying connectivity and geometry (mostly pyridyl or carboxylate coordinating; Figure 1.1).[8] This high modularity results in an abundance of different framework compositions leading to materials with a range of pore sizes, shapes, and functionalities.

The rapidly growing field of MOF chemistry saw its kickoff with the pioneering work of Robson, who first proposed the deliberate design of what he referred to as "infinite polymeric frameworks".[46] Although the successful desolvation of the reported framework, composed of 4,4`,4``,4```-tetracyanotetraphenylmethane and Cu^{I}, was yet to be realized, this work first highlighted a design strategy that would become crucial in MOF chemistry; the geometry of the precursors determines the geometry of the resulting framework (Figure 1.2).[46,47] Initially, the proposed application of these materials focused on anion exchange in a similar manner to the materials discussed above (sections 1.1 – 1.3).[48-50] Other applications of these materials proposed by early pioneers, such as Robson[46,51] and Kitagawa[48-50], included the utilization of these materials as sorbents and heterogeneous catalysts; however, synthetic challenges related to interpenetration and framework stability remained a challenge.[52-55]

1.5 Renaissance of Permanently Porous Metal-Organic Frameworks

Considering that MOFs contain large amounts of potential voids, the design and synthesis of permanently porous frameworks became a key challenge early on for the future application of these materials as adsorbents. In the late 1990s Kitagawa and Rosseinsky exploited the use of rigid frameworks, based on bipyridine linkers, to examine the effects of desolvation and gas adsorption on the microporosity of the material.[48,56] Around the same time, Yaghi first reported the synthesis of a rigid framework using the building block approach where a MOF, composed of 1,4-benzenedicarboxylate and Zinc paddlewheels, was shown to maintain structural integrity and microporosity upon guest evacuation.[57] In 1999, Yaghi reported the synthesis of MOF-5, based on a tetranuclear Zn_4O octahedral cluster and linear 1,4-benzenedicarboxylate linker (Figure 1.3a).[58] MOF-5 ($[Zn_4O(BDC)_3]_n$, BDC = 1,4-benzenedicarboxylate) was shown to maintain its permanent porosity upon guest removal

resulting in a material with the lowest density for any crystalline material reported to date.[58] In a separate publication the same year, Williams introduced HKUST-1 (HKUST = Hong Kong University of Science. and Technology, $[Cu_3(TMA)_2(H_2O)_3]_n$, TMA = benzene-1,3,5-tricarboxylate) which contains open coordination sites that could readily exchange guest molecules (Figure 1.3b).[59] Additionally, HKUST-1 maintained its permanent porosity and gas accessibility upon desonvation.[59] Both MOF-5 and HKUST-1 are comprised of rigid carboxylate ligands which are coordinated to metal clusters forming secondary building units (SBUs), which come together forming an overall robust framework with gas accessible high surface area.[58,59] This approach to MOF synthesis, and that presented in the case of isoreticular MOFs published soon after where linker extension/functionalization highlights the true modularity of these materials,[60] has since lead to tremendous growth in the field.

One limitation of MOFs is that many of these materials are susceptible to ligand displacement by water.[61,62] This is a particularly troubling problem that often plagues utilization of these materials in industry making them difficult to handle and also underperform as sorbents in humid environments.[62] Other drawbacks of MOFs are poor processability and organic phase immiscibility in mixed matrix membrane (MMM) systems.[63] Recently, there have been an increasingly large number of studies dedicated to enhancement of processability and stability of MOFs; this work takes advantage of the porosity and modularity of MOFs to form hybrid porous solids with polymers; this will be the subject of section 1.6.[63]

This thesis is divided into two parts, where two novel approaches to MOF-polymer hybridization are outlined in chapters 2 and 3.[10,11] Chapters 4 and 5 are dedicated to an emerging application of coordination polymers (CPs) and MOFs as energetic materials (introduced in section 1.7).[44] These chapters introduce (a) fundamental approaches to understanding the effects of CP formation on energetic molecule decomposition pathway[13] and (b) a method to render non-energetic MOFs explosive[12].

1.6 Interfacing Porous Crystalline Materials with Polymers for the Synthesis of Hybrid Porous Solids

Of the many applications, which MOFs have shown promise; there are still numerous drawbacks that plague these materials compared to more traditional porous materials commonly used today.[63] As mentioned above, hydrolytic instability of these materials stemming from framework degradation by ligand displacement or water coordination to primary sites of adsorption, are two examples of drawbacks for many MOFs in the literature.[61,62,64] Furthermore, the oftentimes-brittle MOF crystals are difficult to process, particularly for the fabrication of membranes, which is important in many separation processes. As highlighted in section 1.3, zeolites have been combined with amorphous polymers in MMMs to enable a synergistic combination of the permeability and selectivity of zeolites with the processability of polymers.[65-68] However, miscibility/compatibility of the inorganic zeolite crystals with the organic polymer film is challenging. For the reasons outlined above, hybridization of MOFs and polymers have recently shown promise to combat some of the drawbacks of MOFs, while enabling the development of a new class of totally tunable hybrid materials with enhanced properties.[10,11,63,69,70]

Hybridization of MOFs and polymers began with the use of the confined pore space in MOFs for the polymerization of monodisperse polystyrene with controlled tacticity by Kitagawa.[71] The modularity of MOFs allows for the polymerization of larger monomers in the confined pore space resulting in polymers with controlled architectures, unlike polymerization in zeolites which are limited in pore size.[71] This pioneering work then lead to the generation of polymers with controlled tacticity, structure, and sequence. For example the preparation of cross-linked polymers with precise architectural control was achieved by incorporation of cross-linkable ligands in the MOF.[72] The MOF containing cross-linkable ligands was then loaded with monomer and after polymerization; MOF degradation yielded a cross-linked polymer with precisely controlled architecture.[72]

Soon after Kitagawa's pioneering work in 2005 much research attention was focused on combating some of the drawbacks of MOFs by post-synthetic tethering of polymers using grafting from or grafting too approaches to MOF-polymer hybridization.

For example, grafting of thermally switchable polymers from MOFs through surface initiated atom transfer radical polymerization (ATRP) resulted in a thermally switchable MOF-polymer hybrids where the composites can be readily dispersed in water and recollected at high temperatures.[70] This method for MOF-polymer hybridization highlights one approach to the synthesis of more processable MOFs by enabling the formation of dispersions, which can lead to more facile membrane fabrication. Another example of MOF-polymer hybridization for the fabrication of functional and processable membranes involved a concept referred to as photo-induced post-synthetic polymerization. Post-synthetic modification (PSM)[73,74] of microcrystalline UiO-66-NH_2 with methacrylic anhydride allowed formation of polymerizable methacrylamide groups on UiO-66. The crystals were then mixed with butyl methacrylate and a photo-initiator, and then subsequently poured into a Teflon mold. The mixture was exposed to UV light, which initiated the polymerization of butyl methacrylate from the MOF. This resulted in the formation of a flexible membrane with highly dispersed MOF crystals embedded in the matrix.[69] One drawback of the two methods highlighted above is that polymer tethering and hybridization does not enable a high degree of control on the depth of polymer incorporation into the MOF crystals, which can intrude into the crystal space and reduce the desired surface area of the material. Moreover, many of the MOF-polymer hybridization methods reported in the literature are labor intensive and therefore, more facile approaches to functional hybrids are warranted.

1.7 Coordination Polymers with High Energy Density: An Emerging Class of Explosives*

Among the numerous applications proposed for coordination polymers (CPs and in particular the subset referred to as metal-organic frameworks or MOFs), including separations,[75,76] gas storage,[77-79] catalysis,[80-83] and sensing,[84,85] a surprising potential application has recently emerged to use CPs as energetic materials (explosives, propellants, and pyrotechnics).[86-114] In the case of explosives, this class of high energy-density materials typically derives from the combination of fuel (carbon, hydrogen) and oxidizer covalently bonded with the inclusion of atoms such as nitrogen, which can

* Adapted from McDonald, K. A.; Seth, S.; Matzger, A. J. *Cryst. Growth. Des.*, **2015**, *15*, 5963. Copyright 2015 American Chemical Society.

provide additional heat upon decomposition. At first there appears to be a tension between the need for energetic materials to have high density, a requirement to achieve superior detonation velocity/pressure, and the tendency of CPs to be among the most porous (least dense) crystalline materials.[115] However, in addition to having high-energy density, the ideal energetic material should also display good thermal stability, controllable impact sensitivity, and produce environmentally benign reaction products upon detonation.[116,117] These requirements point to the potential advantages of CP tunability in producing tailored energetics.

Explosives can be divided, according to their sensitivity, into primary and secondary explosives. Primary explosives can be initiated via a small stimulus; this class of energetic materials has characteristically fast deflagration to detonation transitions upon initiation.[118] Sensitive functionality in the form of azides, for example, often leads to the high sensitivity of primary explosives. Traditional primary explosives, including mercury (II) fulminate and lead azide, itself a CP, have been widely used in commercial applications since the late 1800s.[119,120] However, due to health and environmental concerns, much attention has been given to replacing these primary explosives with new materials having decreased toxicity and environmental impact.[116,118] As discussed below CPs are of potential interest for this application. With regard to the use of CPs as secondary (low sensitivity, high power) explosives the challenges are considerable as there are many high energy-density organic molecules manufactured safely and on large scale (TNT, RDX, HMX, CL-20, etc.) for applications from munitions to mining.[117] However, there is a potential advantage with CPs over the dominant class of organic molecular materials; by being connected in one or more dimensions the weak (distant) intermolecular interactions of common (molecular) explosives might be replaced with shorter coordination bonds leading to higher density.

Incorporation of energetic linkers into CPs is the most straightforward route to produce energetic CPs. Unfortunately the ubiquitous metal-carboxylate coordination chemistry is undesirable for energetic materials since the nearly fully oxidized carbons detract from performance. Fortunately, metal-nitrogen as well as other coordination chemistries that have been developed are much more attractive for this application.[121-124] CPs based on energetic linkers, such as hydrazines,[96,99-101,125] triazoles,[102,104,111-113] and

tetrazoles,[98,103,107,110] can form one, two, and three-dimensional structures and have emerged as promising candidates for primary or secondary explosives wherein energetic properties such as sensitivity and stability can be modulated. MOFs derived from energetic linkers have been present in the literature for well over a decade,[126-128] although the energetic properties of materials derived from such building blocks have only been explored in detail over the last ten years.[86-97,114] Recently, progress in energetic metal complexes and CPs has been cataloged by Gao and coworkers.[118]

1.8 Figures

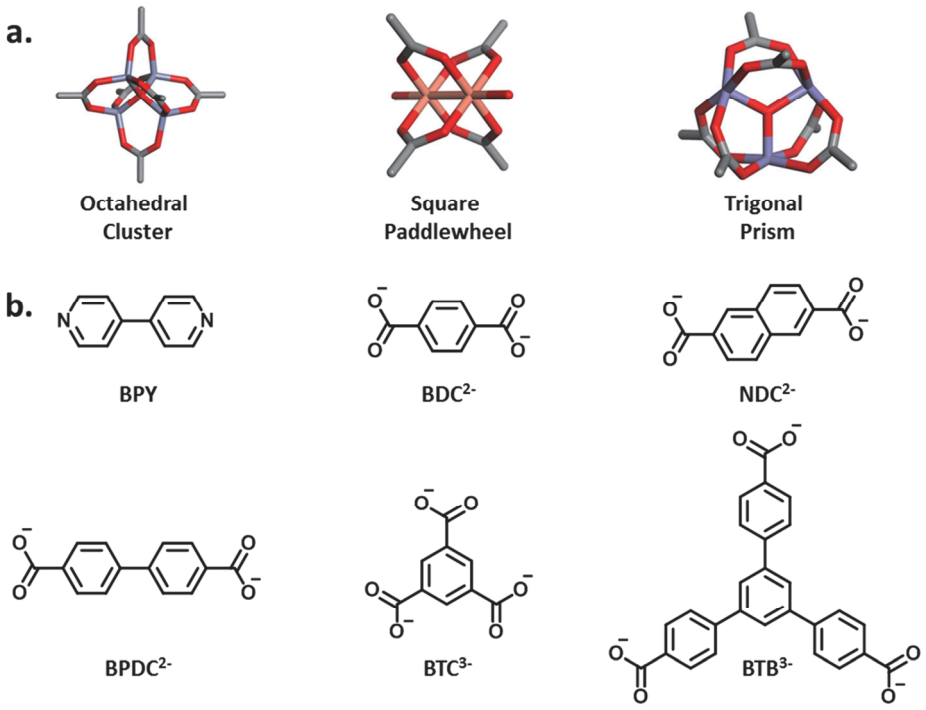

Figure 1.1. Examples of the variety of metal clusters (a) and organic linkers (b) that MOFs can be constructed from. BPY = 4,4′-bipyridine, BDC^{2-} = 1,4-benzenedicarboxylate, NDC^{2-} = 2,6-napthalenedicarboxylate, $BPDC^{2-}$ = biphenyl-4,4′-dicarboxylate, BTC^{3-} = benzene-1,3,5-tricarboxylate, BTB^{3-} = 1,3,5-tris(4-carboxyphenyl)benzene.

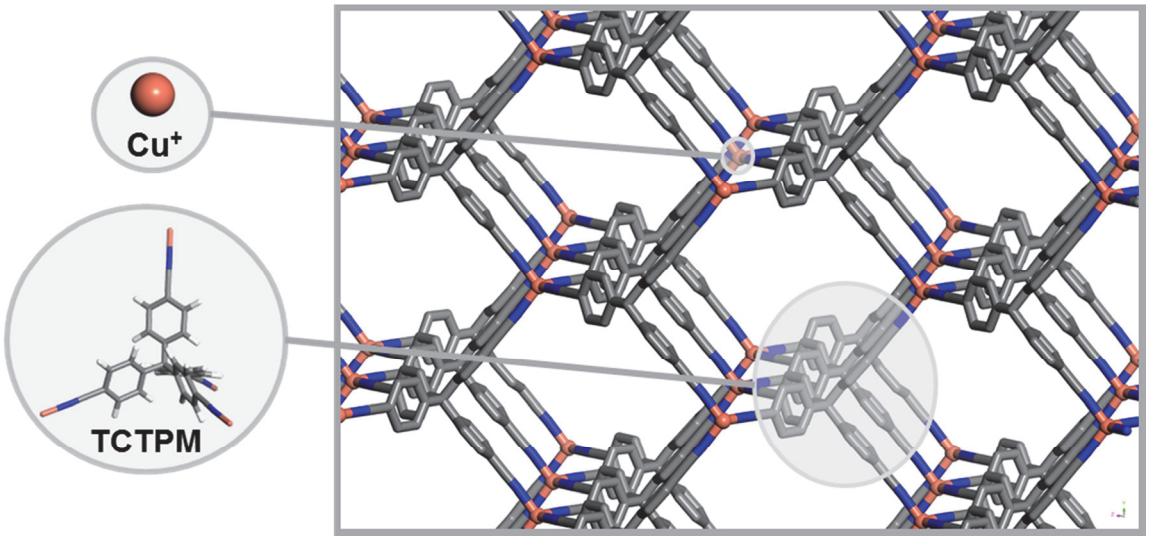

Figure 1.2. (left) Basic building units and (right) extended structure of $[Cu(TCTPM)]_n$ with hydrogen atoms omitted for clarity.

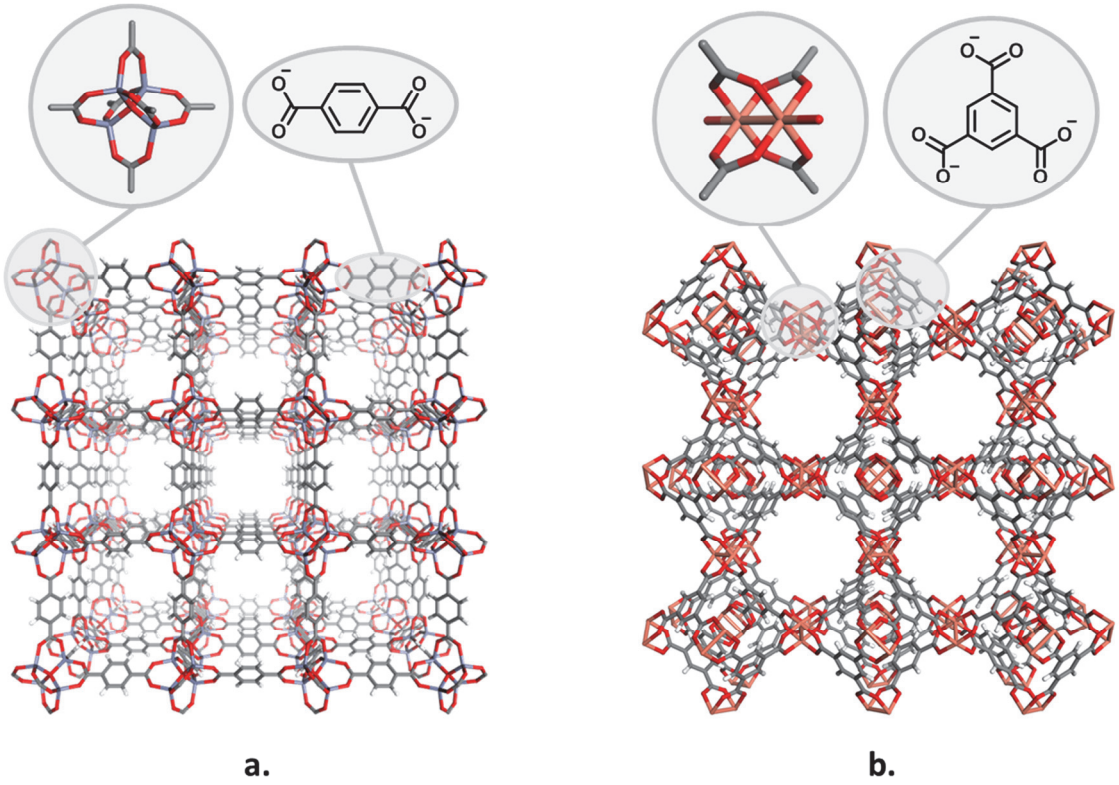

Figure 1.3. The metal clusters, linkers, and extended structures of MOF-5 and HKUST-1. (a; top) the octahedral metal cluster and 1,4-benzenedicarboxylate linker which make up the framework structure of MOF-5 (a; bottom) and (b; top) the copper paddlewheel and benzene-1,3,5-tricarboxylate linker which make up the HKUST-1 framework (b; bottom).

1.9 references

(1) Henning, K.-D.; von Kienle, H. Activated Carbon. *Ullmann's Encyclopedia of Industrial Chemistry*; Wiley-VCH Verlag GmbH & Co. KGaA: Weinheim, Germany, 2000; DOI: 10.1002/14356007.n05_n04 (accessed July 10, 2017).

(2) Flörke, O. W.; Graetsch, H. A.; Brunk, F.; Benda, L.; Paschen, S.; Bergna, H. E.; Roberts, W. O.; Welsh, W. A.; Libanati, C.; Ettlinger, M.; Kerner, D.; Maier, M.; Meon, W.; Schmoll, R.; Gies, H.; Schiffmann, D. Silica. *Ullmann's Encyclopedia of Industrial Chemistry*; Wiley-VCH Verlag GmbH & Co. KGaA: Weinheim, Germany, 2000; DOI: 10.1002/14356007.a23.583.pub3 (accessed July 10, 2017).

(3) Edler, K. J. Mesoporous Silicates. In *Porous Materials*; Bruce, D. W.; O'Hare, D.; Walton, R. I., Eds.; John Wiley & Sons, Ltd: Chichester, West Sussex, U.K. ; Hoboken, N.J., 2011, pp 69-145.

(4) Hudson, L. K.; Misra, C.; Perrotta, A. J.; Wefers, K.; Williams, F. S. Aluminum Oxide. *Ullmann's Encyclopedia of Industrial Chemistry*; Wiley-VCH Verlag GmbH & Co. KGaA: Weinheim, Germany, 2000; DOI: 10.1002/14356007.a01_557 (accessed July 10, 2017).

(5) Broach, R. W.; Jan, D.-Y.; Lesch, D. A.; Kulprathipanja, S.; Roland, E.; Kleinschmit, P. Zeolites. *Ullmann's Encyclopedia of Industrial Chemistry*; Wiley-VCH Verlag GmbH & Co. KGaA: Weinheim, Germany, 2000; DOI: 10.1002/14356007.a28_475.pub2 (accessed July 10, 2017).

(6) Camblor, M. A.; Bong Hong, S. Synthetic Silicate Zeolites: Diverse Materials Accessable through Geoinspiration. In *Porous Materials*; Bruce, D. W.; O'Hare, D.; Walton, R. I., Eds.; John Wiley & Sons, Ltd: Chichester, West Sussex, U.K. ; Hoboken, N.J., 2011, pp 265-325.

(7) *Solid State Chemistry: An Introduction*; 4th edition ed.; Lesley E. Smart, E. A. M., Ed.; CRC press, 2012.

(8) James, S. L. *Chem. Soc. Rev.* **2003**, *32*, 276.

(9) Kepert, C. J. Metal-Organic Framework Materials. In *Porous Materials*; Bruce, D. W.; O'Hare, D.; Walton, R. I., Eds.; John Wiley & Sons, Ltd: Chichester, West Sussex, U.K. ; Hoboken, N.J., 2011, pp 1-67.

(10) McDonald, K. A.; Feldblyum, J. I.; Koh, K.; Wong-Foy, A. G.; Matzger, A. J. *Chem. Commun.* **2015**, *51*, 11994.

(11) Gamage, N.-D. H.; McDonald, K. A.; Matzger, A. J. *Angew. Chem. Int. Ed.* **2016**, *55*, 12099.

(12) McDonald, K. A.; Bennion, J. C.; Leone, A. K.; Matzger, A. J. *Chem. Commun.* **2016**, *52*, 10862.

(13) McDonald, K. A.; Ko, N.; Noh, K.; Bennion, J. C.; Kim, J.; Matzger, A. J. *Chem. Commun.* **2017**, *53*, 7808.

(14) Sircar, S.; Golden, T. C.; Rao, M. B. *Carbon*. **1996**, *34*, 1.

(15) Stoquart, C.; Servais, P.; Bérubé, P. R.; Barbeau, B. *J. Membr. Sci.* **2012**, *411*, 1.

(16) Yin, C. Y.; Aroua, M. K.; Daud, W. M. A. W. *Sep. Purif. Technol.* **2007**, *52*, 403.

(17) Putra, E. K.; Pranowo, R.; Sunarso, J.; Indraswati, N.; Ismadji, S. *Water Res.* **2009**, *43*, 2419.

(18) Juan, Y.; Ke-qiang, Q. *Environ. Sci. Technol.* **2009**, *43*, 3385.
(19) Demiral, H.; Demiral, İ.; Karabacakoğlu, B.; Tümsek, F. *Chem. Eng. Res. Des.* **2011**, *89*, 206.
(20) Xia, Y.; Yang, Z.; Mokaya, R. Templated Porous Carbon Materials: Recent Developments. In *Porous Materials*; Bruce, D. W.; O'Hare, D.; Walton, R. I., Eds.; John Wiley & Sons, Ltd: Chichester, West Sussex, U.K. ; Hoboken, N.J., 2011, pp 217-264.
(21) Anjaneyulu, Y.; Sreedhara Chary, N.; Samuel Suman Raj, D. *Rev. Environ. Sci. Biotechnol.* **2005**, *4*, 245.
(22) Jüntgen, H. *Fuel.* **1986**, *65*, 1436.
(23) Rodríguez-reinoso, F. *Carbon.* **1998**, *36*, 159.
(24) Gil, M. V.; Álvarez-Gutiérrez, N.; Martínez, M.; Rubiera, F.; Pevida, C.; Morán, A. *Chem. Eng. J.* **2015**, *269*, 148.
(25) Ismail, A. F.; David, L. I. B. *J. Membr. Sci.* **2001**, *193*, 1.
(26) Sircar, S. *Ind. Eng. Chem. Res.* **2002**, *41*, 1389.
(27) Gruber, M.; Chouzier, S.; Koehler, K.; Djakovitch, L. *Appl. Catal., A: General.* **2004**, *265*, 161.
(28) Hind, A. R.; Bhargava, S. K.; Grocott, S. C. *Colloids Surf., A: Physicochemical and Engineering Aspects.* **1999**, *146*, 359.
(29) Trimm, D. L.; Stanislaus, A. *Applied Catalysis.* **1986**, *21*, 215.
(30) Busca, G. *Catal. Today.* **2014**, *226*, 2.
(31) Srivastava, N. C.; Eames, I. W. *Appl. Therm. Eng.* **1998**, *18*, 707.
(32) Menon, V. C.; Komarneni, S. *J. Porous Mater.* **1998**, *5*, 43.
(33) Chester, T. L. *Anal. Chem.* **2013**, *85*, 579.
(34) Tanaka, N.; Kobayashi, H.; Ishizuka, N.; Minakuchi, H.; Nakanishi, K.; Hosoya, K.; Ikegami, T. *J. Chromatogr. A.* **2002**, *965*, 35.
(35) Angeletti, E.; Canepa, C.; Martinetti, G.; Venturello, P. *J. Chem. Soc., Perkin Trans. 1.* **1989**, 105.
(36) Shen, Y.; Zhu, S.; Pelton, R. *Macromol. Rapid. Commun.* **2000**, *21*, 956.
(37) Yuan, W.; Lin, Y. S.; Yang, W. *J. Am. Chem. Soc.* **2004**, *126*, 4776.
(38) Barrer, R. M. *Zeolites* **1981**, *1*, 130.
(39) Masters, A. F.; Maschmeyer, T. *Microporous Mesoporous Mater.* **2011**, *142*, 423.
(40) Seth, S.; Matzger, A. J. *Cryst. growth. des.* **2017**, *17*, 4043.
(41) Morris, R. E.; Wheatley, P. S. *Angew. Chem. Int. Ed.* **2008**, *47*, 4966.
(42) Li, J.-R.; Sculley, J.; Zhou, H.-C. *Chem. Rev.* **2012**, *112*, 869.
(43) Liu, J.; Chen, L.; Cui, H.; Zhang, J.; Zhang, L.; Su, C.-Y. *Chem. Soc. Rev.* **2014**, *43*, 6011.
(44) McDonald, K. A.; Seth, S.; Matzger, A. J. *Cryst. growth. des.* **2015**, *15*, 5963.
(45) Zhang, S.; Yang, Q.; Liu, X.; Qu, X.; Wei, Q.; Xie, G.; Chen, S.; Gao, S. *Coord. Chem. Rev.* **2016**, *307*, 292.
(46) Hoskins, B. F.; Robson, R. *J. Am. Chem. Soc.* **1989**, *111*, 5962.
(47) Hoskins, B. F.; Robson, R. *J. Am. Chem. Soc.* **1990**, *112*, 1546.
(48) Kondo, M.; Yoshitomi, T.; Matsuzaka, H.; Kitagawa, S.; Seki, K. *Angew. Chem. Int. Ed.* **1997**, *36*, 1725.

(49) Noro, S.-i.; Kitaura, R.; Kondo, M.; Kitagawa, S.; Ishii, T.; Matsuzaka, H.; Yamashita, M. *J. Am. Chem. Soc.* **2002**, *124*, 2568.
(50) Kitagawa, S.; Kitaura, R.; Noro, S.-i. *Angew. Chem. Int. Ed.* **2004**, *43*, 2334.
(51) Gable, R. W.; Hoskins, B. F.; Robson, R. *J. Chem. Soc., Chem. Commun.* **1990**, 762.
(52) Yaghi, O. M.; Li, H.; Davis, C.; Richardson, D.; Groy, T. L. *Acc. Chem. Res.* **1998**, *31*, 474.
(53) Yaghi, O. M. *Nat. Mater.* **2007**, *6*, 92.
(54) Snurr, R. Q.; Hupp, J. T.; Nguyen, S. T. *AIChE J.* **2004**, *50*, 1090.
(55) Merlau, M. L.; del Pilar Mejia, M.; Nguyen, S. T.; Hupp, J. T. *Angew. Chem. Int. Ed.* **2001**, *40*, 4239.
(56) J. Kepert, C.; J. Rosseinsky, M. *Chem. Commun.* **1999**, 375.
(57) Li, H.; Eddaoudi, M.; Groy, T. L.; Yaghi, O. M. *J. Am. Chem. Soc.* **1998**, *120*, 8571.
(58) Li, H.; Eddaoudi, M.; O'Keeffe, M.; Yaghi, O. M. *Nature.* **1999**, *402*, 276.
(59) Chui, S. S.-Y.; Lo, S. M.-F.; Charmant, J. P. H.; Orpen, A. G.; Williams, I. D. *Science.* **1999**, *283*, 1148.
(60) Eddaoudi, M.; Kim, J.; Rosi, N.; Vodak, D.; Wachter, J.; O'Keeffe, M.; Yaghi, O. M. *Science.* **2002**, *295*, 469.
(61) Low, J. J.; Benin, A. I.; Jakubczak, P.; Abrahamian, J. F.; Faheem, S. A.; Willis, R. R. *J. Am. Chem. Soc.* **2009**, *131*, 15834.
(62) Guo, P.; Dutta, D.; Wong-Foy, A. G.; Gidley, D. W.; Matzger, A. J. *J. Am. Chem. Soc.* **2015**, *137*, 2651.
(63) Kitao, T.; Zhang, Y.; Kitagawa, S.; Wang, B.; Uemura, T. *Chem. Soc. Rev.* **2017**, *46*, 3108.
(64) Kizzie, A. C.; Wong-Foy, A. G.; Matzger, A. J. *Langmuir* **2011**, *27*, 6368.
(65) Vinh-Thang, H.; Kaliaguine, S. *Chem. Rev.* **2013**, *113*, 4980.
(66) Zimmerman, C. M.; Singh, A.; Koros, W. J. *J. Membr. Sci.* **1997**, *137*, 145.
(67) Chung, T.-S.; Jiang, L. Y.; Li, Y.; Kulprathipanja, S. *Prog. Polym. Sci.* **2007**, *32*, 483.
(68) Kemp, D. R.; Paul, D. R. *J. Polym. Sci., Part B: Polym. Phys.* **1974**, *12*, 485.
(69) Zhang, Y.; Feng, X.; Li, H.; Chen, Y.; Zhao, J.; Wang, S.; Wang, L.; Wang, B. *Angew. Chem.* **2015**, *127*, 4333.
(70) Liu, H.; Zhu, H.; Zhu, S. *Macromol. Mater. Eng.* **2015**, *300*, 191.
(71) Uemura, T.; Kitagawa, K.; Horike, S.; Kawamura, T.; Kitagawa, S.; Mizuno, M.; Endo, K. *Chem. Commun.* **2005**, 5968.
(72) Distefano, G.; Suzuki, H.; Tsujimoto, M.; Isoda, S.; Bracco, S.; Comotti, A.; Sozzani, P.; Uemura, T.; Kitagawa, S. *Nat. Chem.* **2013**, *5*, 335.
(73) Wang, Z.; Cohen, S. M. *J. Am. Chem. Soc.* **2007**, *129*, 12368.
(74) Tanabe, K. K.; Cohen, S. M. *Chem. Soc. Rev.* **2011**, *40*, 498.
(75) Li, J.-R.; Kuppler, R. J.; Zhou, H.-C. *Chem. Soc. Rev* **2009**, *38*, 1477.
(76) Li, J.-R.; Sculley, J.; Zhou, H.-C. *Chem. Rev.* **2012**, *112*, 869.

(77) Getman, R. B.; Bae, Y.-S.; Wilmer, C. E.; Snurr, R. Q. *Chem. Rev.* **2012**, *112*, 703.
(78) Suh, M. P.; Park, H. J.; Prasad, T. K.; Lim, D.-W. *Chem. Rev.* **2012**, *112*, 782.
(79) Sumida, K.; Rogow, D. L.; Mason, J. A.; McDonald, T. M.; Bloch, E. D.; Herm, Z. R.; Bae, T.-H.; Long, J. R. *Chem. Rev.* **2012**, *112*, 724.
(80) Lee, J.; Farha, O. K.; Roberts, J.; Scheidt, K. A.; Nguyen, S. T.; Hupp, J. T. *Chem. Soc. Rev.* **2009**, *38*, 1450.
(81) Ma, L.; Abney, C.; Lin, W. *Chem. Soc. Rev.* **2009**, *38*, 1248.
(82) Corma, A.; García, H.; Llabrés i Xamena, F. X. *Chem. Rev.* **2010**, *110*, 4606.
(83) Yoon, M.; Srirambalaji, R.; Kim, K. *Chem. Rev.* **2012**, *112*, 1196.
(84) Kreno, L. E.; Leong, K.; Farha, O. K.; Allendorf, M.; Van Duyne, R. P.; Hupp, J. T. *Chem. Rev.* **2012**, *112*, 1105.
(85) Liu, D.; Lu, K.; Poon, C.; Lin, W. *Inorg. Chem.* **2014**, *53*, 1916.
(86) Xia, Z.; Chen, S.; Wei, Q.; Qiao, C. *J. Solid State Chem.* **2011**, *184*, 1777.
(87) Wang, S.-W.; Yang, L.; Feng, J.-L.; Wu, B.-D.; Zhang, J.-G.; Zhang, T.-L.; Zhou, Z.-N. *Z. Anorg. Allg. Chem.* **2011**, *637*, 2215.
(88) Xu, C.-X.; Zhang, J.-G.; Yin, X.; Jin, X.; Li, T.; Zhang, T.-L.; Zhou, Z.-N. *J. Solid State Chem.* **2015**, *226*, 59.
(89) Wu, B.-D.; Bi, Y.-G.; Li, F.-G.; Yang, L.; Zhou, Z.-N.; Zhang, J.-G.; Zhang, T.-L. *Z. Anorg. Allg. Chem.* **2014**, *640*, 224.
(90) Wang, S.-H.; Zheng, F.-K.; Wu, M.-F.; Liu, Z.-F.; Chen, J.; Guo, G.-C.; Wu, A. Q. *CrystEngComm* **2013**, *15*, 2616.
(91) Wu, B.-D.; Zhang, T.-L.; Li, Y.-L.; Tong, W.-C.; Zhou, Z.-N.; Zhang, J.-G.; Yang, L. *Z. Anorg. Allg. Chem.* **2013**, *639*, 2209.
(92) Wu, B.-D.; Zhou, Z.-N.; Li, F.-G.; Yang, L.; Zhang, T.-L.; Zhang, J.-G. *New J. Chem.* **2013**, *37*, 646.
(93) Tao, G.-H.; Parrish, D. A.; Shreeve, J. n. M. *Inorg. Chem.* **2012**, *51*, 5305.
(94) Yang, L.; Wu, B.; Zhang, T.; Liu, Z.; Zhang, J. *Propellants Explos. Pyrotech.* **2010**, *35*, 521.
(95) Cudziło, S.; Nita, M. *J. Hazard. Mater.* **2010**, *177*, 146.
(96) Liu, Z.; Zhang, T.; Zhang, J.; Wang, S. *J. Hazard. Mater.* **2008**, *154*, 832.
(97) Tang, Z.; Zhang, J.-G.; Liu, Z.-H.; Zhang, T.-L.; Yang, L.; Qiao, X.-J. *J. Mol. Struct.* **2011**, *1004*, 8.
(98) Zhang, K.-L.; Pan, Z.-C.; Chang, Y.; Liu, W.-L.; Ng, S. W. *Mater. Lett.* **2009**, *63*, 2136.
(99) Wu, B.-D.; Yang, L.; Wang, S.-W.; Zhang, T.-L.; Zhang, J.-G.; Zhou, Z.-N.; Yu, K.-B. *Z. Anorg. Allg. Chem.* **2011**, *637*, 450.
(100) Bushuyev, O. S.; Brown, P.; Maiti, A.; Gee, R. H.; Peterson, G. R.; Weeks, B. L.; Hope-Weeks, L. J. *J. Am. Chem. Soc.* **2012**, *134*, 1422.
(101) Bushuyev, O. S.; Peterson, G. R.; Brown, P.; Maiti, A.; Gee, R. H.; Weeks, B. L.; Hope-Weeks, L. J. *Chem. Eur. J.* **2013**, *19*, 1706.
(102) Li, S.; Wang, Y.; Qi, C.; Zhao, X.; Zhang, J.; Zhang, S.; Pang, S. *Angew. Chem. Int. Ed.* **2013**, *52*, 14031.

(103) Lin, J.-D.; Wang, S.-H.; Cai, L.-Z.; Zheng, F.-K.; Guo, G.-C.; Huang, J.-S. *CrystEngComm.* **2013**, *15*, 903.

(104) Gao, W.; Liu, X.; Su, Z.; Zhang, S.; Yang, Q.; Wei, Q.; Chen, S.; Xie, G.; Yang, X.; Gao, S. *J. Mater. Chem. A*. **2014**, *2*, 11958.

(105) Liu, X.; Yang, Q.; Su, Z.; Chen, S.; Xie, G.; Wei, Q.; Gao, S. *RSC Adv.* **2014**, *4*, 16087.

(106) Zhang, Q.; Shreeve, J. M. *Angew. Chem. Int. Ed.* **2014**, *53*, 2540.

(107) Zhang, S.; Liu, X.; Yang, Q.; Su, Z.; Gao, W.; Wei, Q.; Xie, G.; Chen, S.; Gao, S. *Chem. Eur. J.* **2014**, *20*, 7906.

(108) Bennion, J. C.; McBain, A.; Son, S. F.; Matzger, A. J. *Cryst. Growth Des.* **2015**, *15*, 2545.

(109) Blair, L. H.; Colakel, A.; Vrcelj, R. M.; Sinclair, I.; Coles, S. J. *Chem. Commun.* **2015**, *51*, 12185.

(110) Feng, Y.; Liu, X.; Duan, L.; Yang, Q.; Wei, Q.; Xie, G.; Chen, S.; Yang, X.; Gao, S. *Dalton Trans.* **2015**, *44*, 2333.

(111) Liu, X.; Gao, W.; Sun, P.; Su, Z.; Chen, S.; Wei, Q.; Xie, G.; Gao, S. *Green Chem.* **2015**, *17*, 831.

(112) Qu, X.; Zhang, S.; Yang, Q.; Su, Z.; Wei, Q.; Xie, G.; Chen, S. *New J. Chem.* **2015**, 39, 7849.

(113) Chen, S.; Shu, S.; Gao, S. *Inorg. Chim. Acta.* **2009**, *362*, 3043.

(114) Friedrich, M.; Gálvez-Ruiz, J. C.; Klapötke, T. M.; Mayer, P.; Weber, B.; Weigand, J. J. *Inorg. Chem.* **2005**, *44*, 8044.

(115) The advantages of dense MOFs in certain applications is increasingly being recognized. See for example: Tominaka, S.; Hamoudi, H.; Suga, T.; Bennett, T. D.; Cairns, A. B.; Cheetham, A. K. *Chem. Sci.* **2015**, *6*, 1465.

(116) Steinhauser, G.; Klapötke, T. M. *Angew. Chem. Int. Ed.* **2008**, *47*, 3330.

(117) Sikder, A. K.; Sikder, N. *J. Hazard. Mater.* **2004**, *112*, 1.

(118) Oyler, K. D. In *Green Energetic Materials*; John Wiley & Sons, Ltd: 2014, p 103.

(119) Glen, G. L. *J. Am. Chem. Soc.* **1963**, *85*, 3892.

(120) Beck, W.; Evers, J.; Göbel, M.; Oehlinger, G.; Klapötke, T. M. *Z. Anorg. Allg. Chem.* **2007**, *633*, 1417.

(121) Xue, H.; Gao, Y.; Twamley, B.; Shreeve, J. M. *Chem. Mater.* **2005**, *17*, 191.

(122) Wang, K.; Zeng, D.; Zhang, J.-G.; Cui, Y.; Zhang, T.-L.; Li, Z.-M.; Jin, X. *Dalton Trans.* **2015**, *44*, 12497.

(123) Yang, Q.; Wei, Q.; Chen, S.-P.; Zhang, G.-C.; Zhou, C.-S.; Gao, S.-L. *J. Anal. Appl. Pyrolysis.* **2013**, *99*, 66.

(124) Talawar, M. B.; Sivabalan, R.; Mukundan, T.; Muthurajan, H.; Sikder, A. K.; Gandhe, B. R.; Rao, A. S. *J. Hazard. Mater.* **2009**, *161*, 589.

(125) Shunguan, Z.; Youchen, W.; Wenyi, Z.; Jingyan, M. *Propellants Explos. Pyrotech.* **1997**, *22*, 317.

(126) Jiang, C.; Yu, Z.; Wang, S.; Jiao, C.; Li, J.; Wang, Z.; Cui, Y. *Eur. J. Inorg. Chem.* **2004**, *2004*, 3662.

(127) Su, C.-Y.; Goforth, A. M.; Smith, M. D.; Pellechia, P. J.; zur Loye, H.-C. *J. Am. Chem. Soc.* **2004**, *126*, 3576.

(128) Dincă, M.; Dailly, A.; Liu, Y.; Brown, C. M.; Neumann, D. A.; Long, J. R. *J. Am. Chem. Soc.* **2006**, *128*, 16876.

Chapter II

Polymer@MOF@MOF: "grafting from" atom transfer radical polymerization for the synthesis of hybrid porous solids[†]

2.1 Introduction

Zeolites, metal oxides, and activated carbons currently dominate industry-scale small molecule adsorption and separation applications;[1-4] combining these types of materials with polymers to form hybrid porous materials has the potential to enhance sorbent properties by combining the characteristics of inorganic and organic components.[5,6] Organic-inorganic hybrid materials derived from grafting polymers to zeolites,[7] silica nanoparticles,[8] and carbon nanotubes,[9] for example, have received increasing attention in the past few years. These materials have shown promise in membrane mediated separations.[10, 11] However, compatibility between inorganic and organic components in hybrids can pose problems for the fabrication of functional and robust composites stemming from issues such as defects and poor polymer-inorganic adhesion.[11,12] Metal-organic frameworks (MOFs), materials composed of metal clusters connected by organic bridging linkers, have tunable pore sizes/shapes and modular structures[13-16] that lend themselves to functionalization of the sort ideally suited to produce robust hybrid materials[17] that maintain excellent compatibility between MOF and polymer components.[12,18] Recently, hybrid MOF materials have emerged, taking advantage of the porosity and tunability of MOFs to form composites with polymeric materials.[19-26] Many of the advancements that have been made in the realm of MOF-polymer composites have aimed to improve upon or combat some of the drawbacks of MOFs including poor processability and organic phase immiscibility. Grafting polymers from MOFs[24] or post synthetic polymerization to link MOF crystals together[19] are both promising routes to

---

[†] McDonald, K. A.; Feldblyum, J. I.; Koh, K.; Wong-Foy, A. G.; Matzger, A. J. *Chem. Commun.*, **2015**, *51*, 11994. Adapted by permission of The Royal Society of Chemistry.

address these problems. However, the inclusion of polymers into MOF void space can be problematic for maximizing the accessibility of internal pores. Herein, polymer grafting and coating on MOFs is achieved by utilizing a core-shell architecture[27-30] that enables control over the extent to which polymer intrudes into the internal crystal pores. This strategy achieves polymer hybridization while maintaining the internal pore structure of the un-functionalized MOF.

A hybrid polymer-MOF architecture, polymer@MOF@MOF, in which polymer chains are covalently tethered to the outer shell of a core-shell MOF was targeted. Synthetic parameters were chosen with the goal of maintaining MOF rigidity and obtaining uniform polymer coverage on the surface of the MOF without substantially compromising internal porosity. In order to tether a polymer to a MOF, "grafting to" and "grafting from" approaches were considered as having the potential to yield the desired hybrid polymer-MOF.[31] "Grafting to" would involve the reaction of end-functionalized polymers with functional groups located on the MOF albeit with the risk that sterically bulky polymer chains might cause a decrease in the grafting density on the MOF. Therefore "grafting from" was chosen. This approach involves polymerization from active sites on the MOF, enabling the growth of polymer from initiator sites. Initiator sites can be incorporated onto the MOF by post-synthetic modification (PSM)[32] of a 2-aminoterephthalate linker with the carboxylic acid anhydride of the initiator for polymerization, thereby generating the tethered initiator. PSM of a MOF derived solely from 2-aminoterephthalate would result in initiator-carrying linker (and thus polymer) inclusion throughout the framework, thereby blocking significant amounts of pore space. To overcome this challenge, a core-shell architecture was utilized in which a shell of IRMOF-3, containing the 2-aminoterephthalate linker, was grown from the surface of MOF-5 to form IRMOF-3@MOF-5 (Figure 2.1a).[27,28] MOF-5 was chosen because of its high surface area, reproducible synthesis, and broad use as a prototype system in the literature. Initiator carrying sites can be installed onto the IRMOF-3 outer shell by PSM.[32] This sequence enables formation of the initiator carrying linker selectively onto the outer shell for the polymerization of vinyl-type monomers.

2.2 Results and Discussion

PSM was carried out by reaction of the amine groups of the IRMOF-3 shell with 2-bromoisobutyric anhydride and the resultant MOF is referred to as ICL@IRMOF-3@MOF-5 (initiator carrying linker@IRMOF-3@MOF-5, Figure 2.1b). With a MOF bearing a selectively placed polymerization initiator in hand, copper mediated Atom Transfer Radical Polymerization (ATRP)[33] was carried out using methyl methacrylate (Figure 2.1c). The polymer@MOF@MOF materials, as exemplified by poly(methyl methacrylate)@IRMOF-3@MOF-5 (hereafter referred to as PMMA@IRMOF-3@MOF-5) is described here. PMMA@IRMOF-3@MOF-5 was washed thoroughly (see experimental details in chapter 2.4) and activated under reduced pressure (~20 mTorr). Powder X-ray diffraction (PXRD) of MOF-5, IRMOF-3@MOF-5, ICL@IRMOF-3@MOF-5, and PMMA@IRMOF-3@MOF-5 demonstrates that the framework maintains its structure after shell formation, PSM, and polymer grafting (Figure 2.2). Thermogravimetric analysis (TGA) of activated PMMA@IRMOF-3@MOF-5 reveals the depolymerization of PMMA at ~415 °C and subsequent degradation of MOF-5 at ~530 °C (Figures 2.3 an 2.4).

In order to determine the effects of functionalization and polymerization on the gas-accessible surface area of the core-shell MOF, the Brunauer-Emmett-Teller (BET) approximation was applied to data obtained from N_2 sorption experiments (Figure 2.5 and Figures 2.6-2.9). The initial, activated MOF-5 isotherm shows a surface area of 3530 m^2g^{-1}. The surface area of the ICL@IRMOF-3@MOF-5 is 3381 m^2g^{-1} indicating that the shell formation and functionalization occurs with minimal erosion of surface area. PMMA@IRMOF-3@MOF-5 displays a surface area of 2857 m^2g^{-1} after polymerization for 5 minutes and 2289 m^2g^{-1} after polymerization for 1 hour indicating that the MOF-5 core is intact and the porosity accessible. We hypothesize that the loss of surface area after polymerization is due primarily to the additional mass of the polymer, which does not contribute to the surface area. TGA of PMMA@IRMOF-3@MOF-5 shows the depolymerization of ~19 wt. % PMMA after polymerization for 5 minutes and ~23 wt. % PMMA after polymerization for 1 hour (Figure 2.4), consistent with this notion although the observed further decrease in surface area of PMMA@IRMOF-3@MOF-5 after a

longer polymerization time is also attributed to a greater role of the occupancy of the pore space by the growing polymer chains.

Understanding degree of polymerization and polymer molecular weight distribution (PDI) is necessary for optimization of the polymer segment properties and is expected to influence guest transport into the MOF core. In order to free the polymer chains from the MOF, hydrolysis of the framework is required. Although MOF-5 readily disintegrates in water, PMMA@IRMOF-3@MOF-5 crystals remain intact initially consistent with poor wetting behavior of these hydrophobic hybrids. However, treatment with 1M NaOH accompanied by intense shaking for several minutes, led to the disappearance of the PMMA@IRMOF-3@MOF-5 crystals. The polymer was then isolated by CH_2Cl_2 extraction. The ability to harvest the PMMA and determine molecular weight by gel permeation chromatography (GPC) was observed to be sensitive to digestion protocol; this is likely the result of a balance between achieving complete framework degradation and avoiding extensive hydrolysis of the methyl ester side chains. GPC analysis found consistently high molecular weight polymer with narrow PDI (Mn = 421 kDa-615 kDa, PDI = 1.36-1.44, Figure 2.10). Initial results suggest that the molecular weight of the polymer does not increase linearly with time, which suggests that this is not a simple living polymerization without termination. To confirm that the polymerization depends on the presence of the initiator carrying functional group, polymerizations were conducted under identical conditions as those used to produce PMMA@IRMOF-3@MOF-5. The polymerization with IRMOF-3@MOF-5 and no copper catalyst resulted in no polymer grafted to the framework; the same result was found when using ICL@IRMOF-3@MOF-5. Therefore catalyst is necessary to initiate polymer grafting.

Raman microspectroscopy was applied to determine the depth of polymerization from the external surface of the MOF hybrid material. Single crystals were cleaved mechanically to expose the internal cross-section, and the intensity of the peak corresponding to the CH_2 stretch of the PMMA backbone was mapped as a function of the distance from the crystal surface (Figure 2.11). Raman mapping of PMMA@IRMOF-3@MOF-5 cross-sections demonstrate that the polymer extends to a depth of ~10 μm into the crystal. Furthermore, Raman mapping of freshly cut single crystals of IRMOF-

3@MOF-5 (Figure 2.12) demonstrates that the fluorescence background signal is much more pronounced in the IRMOF-3 shell (again extending ~10 μm into the MOF crystal); taken in combination these results demonstrate co-localization of shell and polymer consistent with the selective initiation of polymerization from the sites where the initiator-carrying linker is present. Hence, by modulating the thickness of the initiator-carrying shell, the thickness of the polymer film can likewise be controlled.

2.3 Conclusions

PMMA@IRMOF-3@MOF-5, a hybrid polymer-MOF composite, was produced through a combination of core-shell and post-synthetic modification techniques. The use of core-shell architectures ultimately allows for polymer chains to be tethered to the outer shell of MOF-5, thereby, maintaining the inner porosity of the MOF. "Grafting from" using ATRP enables polymerization of PMMA on the outer shell of a MOF crystal, and opens the possibility to produce a complex polymer microstructure to modulate the accessibility of guests to a MOF.

2.4 Experimental Methods

Zinc nitrate tetrahydrate, $Zn(NO_3)_2 \bullet 4H_2O$. Zinc nitrate tetrahydrate was prepared as previously described.[34]

IRMOF-3@MOF-5. IRMOF-3@MOF-5 was prepared by a method slightly modified from the literature procedure.[27] H_2ABDC (48.0 mg, 0.265 mmol) and H_2BDC (0.100 g, 0.602 mmol) were added to separate 20 mL vials. $Zn(NO_3)_2 \bullet 4H_2O$ (0.500 g, 1.91 mmol) dissolved in 15 mL of DEF was added to the vial containing H_2BDC and $Zn(NO_3)_2 \bullet 4H_2O$ (0.208 g, 0.795 mmol) dissolved in 10 mL of DEF was added to the vial containing H_2ABDC. The two mixtures were sonicated for 15 minutes and heated to 100 °C for 12 hours. Both solutions were decanted and the supernatants were exchanged. The mixtures were heated at 100 °C for another 4 hours. The products were then washed with DEF (4×15 mL over 24 hours) and washed/soaked in CH_2Cl_2 (4×15 mL over 24 hours).

Post-synthetic modification to form initiator carrying linker@MOF-5 (ICL@IRMOF-3@MOF-5). ICL@IRMOF-3@MOF-5 was prepared by a method slightly modified from the literature procedure by Cohen and coworkers[32] 2-

Bromoisobutyric anhydride (2-BIBA) (71.2 mg, 0.225 mmol) was added to a 20 mL septum-capped vial in a glovebox. The 2-BIBA was taken out of the glovebox and dissolved in 15 mL of degassed DCM. IRMOF-3@MOF-5 crystals, in CH_2Cl_2, were transferred to a separate 20 mL septum capped vial, the CH_2Cl_2 solution was decanted from the crystals and the vial was capped and purged with nitrogen. The solution of DCM and 2-BIBA was then injected into the vial containing IRMOF-3@MOF-5 using a 25 mL degassed syringe. The mixture was allowed to shake at room temperature for 72 h and subsequently washed thoroughly with DCM 4×15 mL over 24 hours. The sample was then activated and the product was weighed yielding ~40.3 mg of ICL@IRMOF-3@MOF-5.

Atom transfer radical polymerization to generate PMMA@IRMOF-3@MOF-5. ATRP of methyl methacrylate (MMA) at ICL@IRMOF-3@MOF-5 was carried out under air-free conditions. In an N_2 filled glovebox, ICL@IRMOF-3@MOF-5 (20.0 mg) was weighed into a 20 mL septum-capped vial (vial 1). 1,4,8,11-Tetraaza-1,4,8,11-tetramethylcyclotetradecane (Me_4Cyclam) (15.0 mg, 0.0585 mmol) and CuBr (1.20 mg, 0.00836 mmol) were weighed out into another 20 mL septum-capped vial (vial 2). Xylenes (4 mL) were added to vial 2 and the solution was sonicated and heated gently for 20 minutes. The catalyst solution (vial 2) was added to vial 1 using a cannula. After the reaction mixture was stirred for 10 minutes, methyl methacrylate (2 mL) was introduced via a degassed syringe and the reaction mixture was heated slowly to 65 °C, then shaken for one hour. The reaction mixture was cooled and the crystals were washed thoroughly with xylenes (4×15 mL over 24 hours), THF (4×15 mL over 24 hours), and then washed in DCM (4×15 mL over 24 hours) prior to activation. The product was weighed and yielded ~30.8 mg of PMMA@IRMOF-3@MOF-5.

Activation. Samples were activated by exposure to a dynamic vacuum (10^{-2} Torr) for 24 hours.

Powder X-ray diffraction. Powder X-ray diffraction (PXRD) patterns were collected using a Rigaku R-axis Spider diffractometer with an image plate detector and graphite monochromated Cu-Kα radiation (1.5406 Å). The patterns were collected with the tube operating at 40 kV and 44 mA. Images were collected in transmission mode with χ set at 45°, ϕ rotating at 10°/min, and ω oscillating between 5° and 50° to minimize the effects

of preferred orientation. Integration of the resulting images was performed in the AreaMax (2.0) software package with a step size of 0.1 in 2θ.

Gas sorption measurements. Sorption experiments were carried out using a NOVA *e*-series 4200 surface area analyser (Quantachrome Instruments, Boynton Beach, Florida, USA). N_2 (99.999%) was purchased from Cryogenic Gases and used as received. For N_2 measurements, a glass sample cell was charged with ~20 mg sample and analysed at 77 K. Sorption isotherms were collected in the NOVAwin software.

Thermogravimetric Analysis. A TA Instruments Q50 TGA was used to obtain thermogravimetric data in which the analyte was heated from 25 °C to 600 °C at a rate of 10 °C/min and analysed in a platinum pan under flowing nitrogen.

Gel Permeation Chromatography. GPC of PMMA@IRMOF-3@MOF-5 was performed after a basic digestion using 1M NaOH and isolation of the polymer by a CH_2Cl_2 extraction. The isolated polymer samples were dissolved in THF. The GPC analysis was performed on a Shimadzu GPC containing three columns in series with a refractive index detector and a diode array UV-Vis detector. The GPC was calibrated with narrow polydispersity polystyrene standards and the molecular weights are reported as polystyrene equivalents based on UV-Vis detection.

Raman Spectroscopy. For Raman mapping of PMMA@IRMOF-3@MOF-5, a single crystal was cleaved mechanically to expose the internal cross-section; the same procedure was followed for the Raman mapping of IRMOF-3@MOF-5. Raman spectra were obtained using a Renishaw inVia Raman microscope equipped with a RenCan CCD detector, 532 nm laser, 1800 lines/mm grating, and 50 μm slit was used for collecting data. Spectra were collected using the mapping setting in which a region of the cross-section (interior to exterior) was selected for analysis. The spectra were collected using a static scan mode in the range of 950-1475 cm^{-1} for IRMOF-3@MOF-5 and 700-1200 cm^{-1} for PMMA@IRMOF-3@MOF-5 and then analysed using the Wire 3.4 software package. Calibration of the instrument was performed using a silicon standard for all experiments.

2.5 Figures

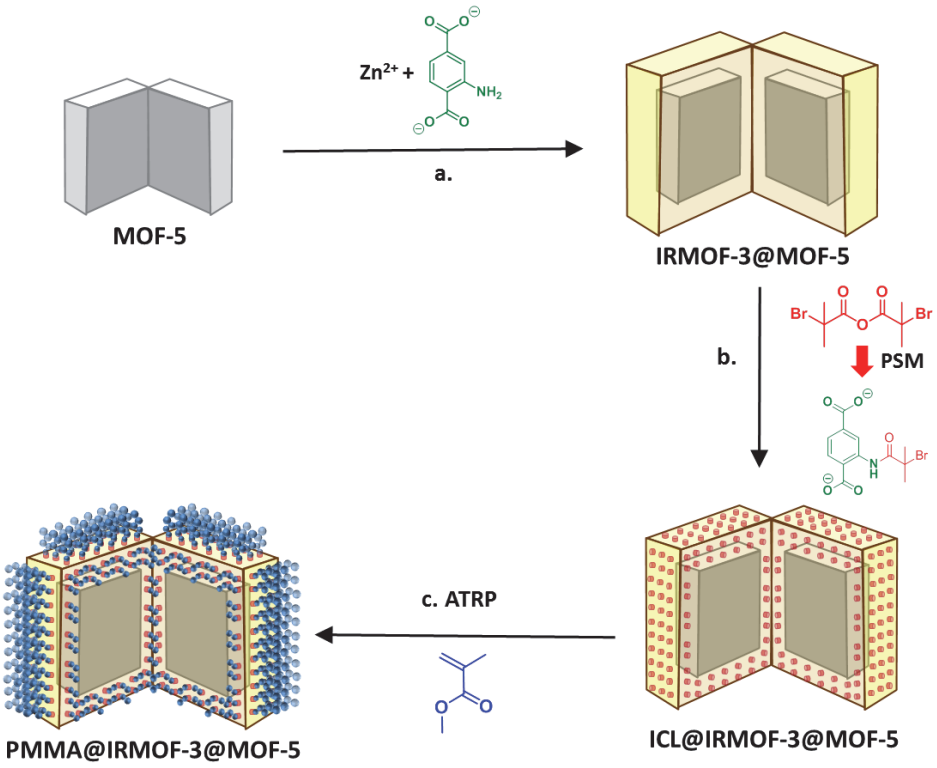

Figure 2.1. Synthetic route to PMMA@IRMOF-3@MOF-5 wherein the cubic MOF crystal is represented as an open book to show both the core and shell chemistry: (a) core-shell formation on MOF-5 by growth of IRMOF-3 from MOF-5 seed crystals (IRMOF-3@MOF-5), (b) reaction of amine groups on the IRMOF-3 shell with 2-bromoisobutyric anhydride to generate initiator carrying linker@IRMOF-3@MOF-5 (ICL@IRMOF-3@MOF-5) and (c) ATRP on ICL@IRMOF-3@MOF-5 with methyl methacrylate to generate PMMA@IRMOF-3@MOF-5. See section 2.4 for experimental details.

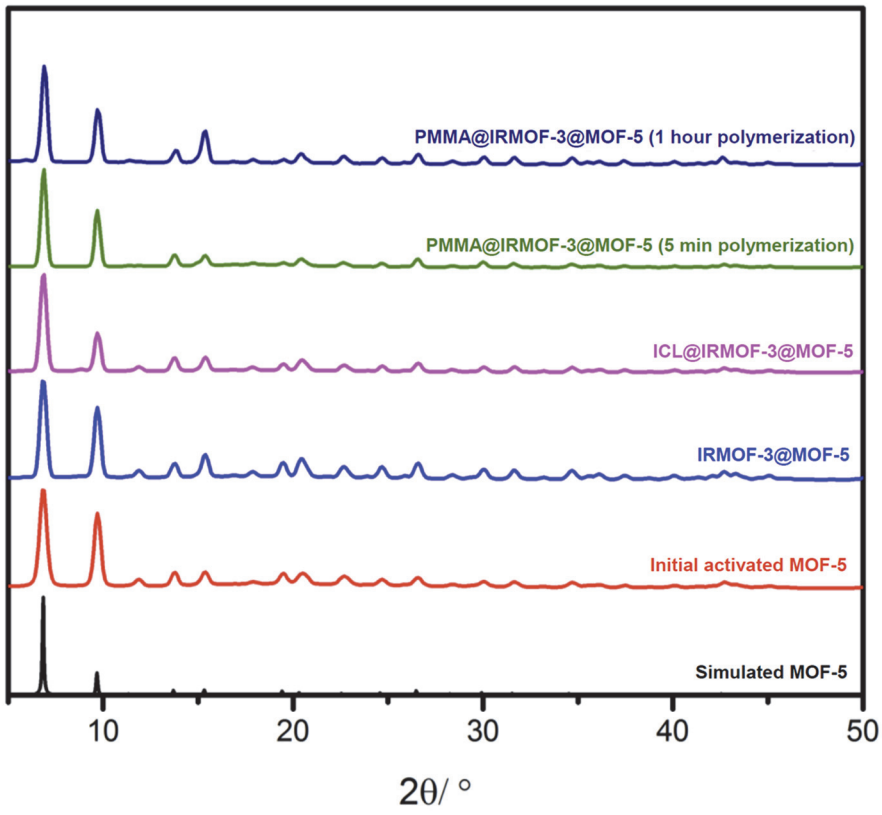

Figure 2.2. Powder X-ray diffraction (PXRD) patterns comparing the simulated MOF-5 pattern (black) to the diffractograms of as-synthesized MOF-5 (red), IRMOF-3@MOF-5 (light blue), ICL@IRMOF-3@MOF-5 (pink), PMMA@IRMOF-3@MOF-5 after 5 minutes of polymerization at 65 °C (green), and PMMA@IRMOF-3@MOF-5 after 1 hour of polymerization at 65 °C (dark blue).

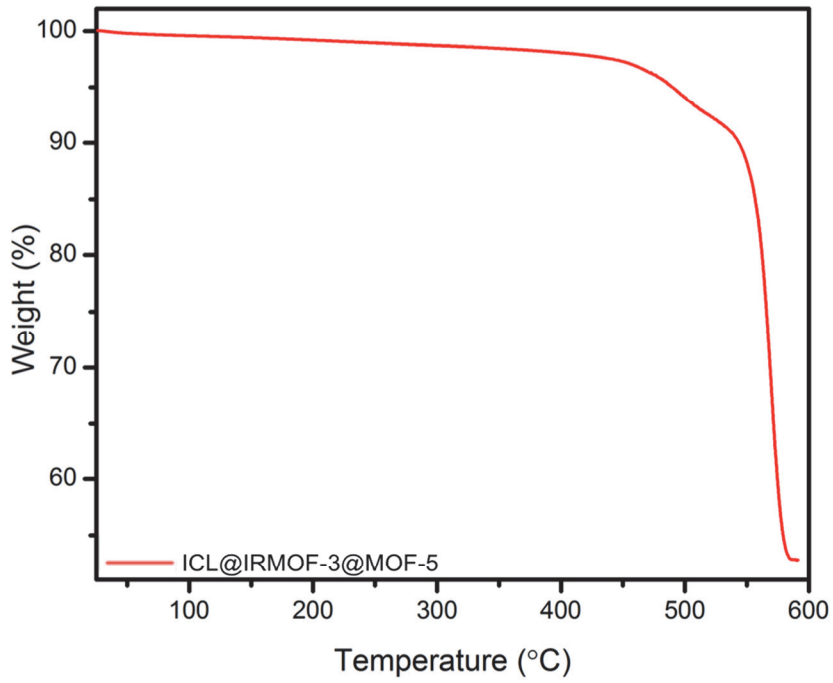

Figure 2.3. Thermogravimetric Analysis (TGA) of ICL@IRMOF-3@MOF-5 using a ramp rate of 10 °C/min.

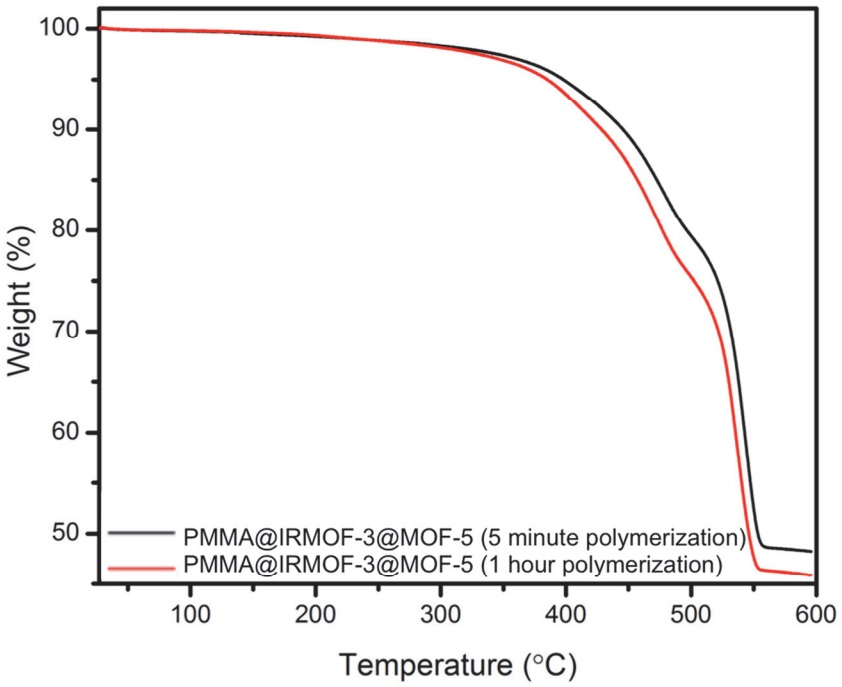

Figure 2.4. TGA of PMMA@IRMOF-3@MOF-5 after 5 minutes (black) and 1 hour (red) polymerization using a ramp rate of 10 °C/min.

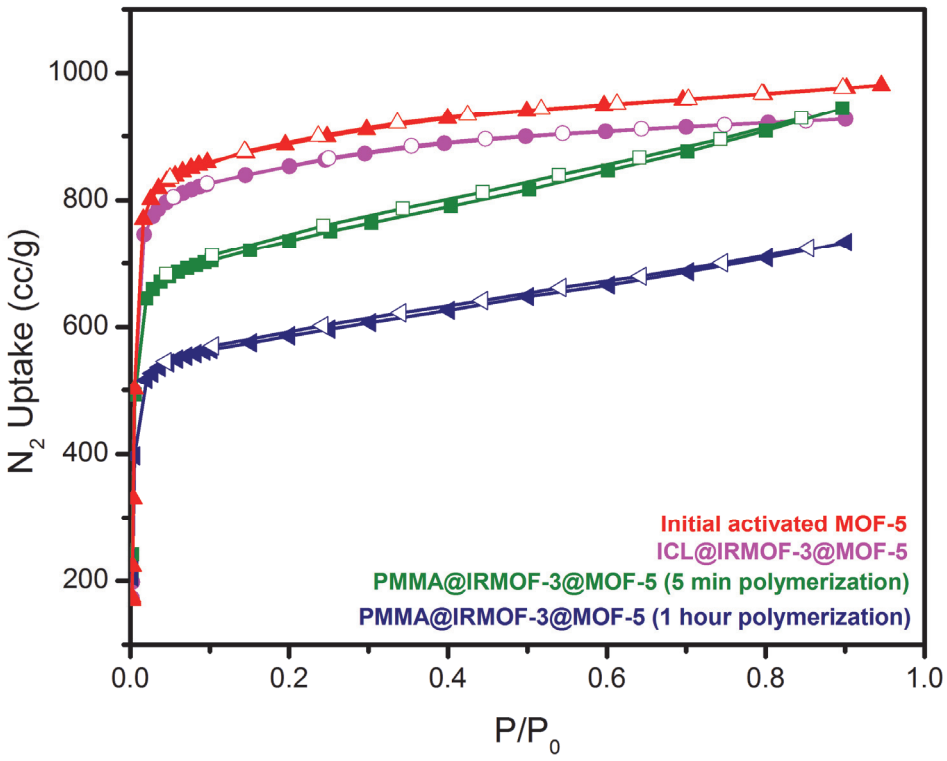

Figure 2.5. N_2 sorption isotherms of MOF-5 (red), ICL@IRMOF-3@MOF-5 (pink), PMMA@IRMOF-3@MOF-5 after 5 minutes of polymerization at 65 °C (green), and PMMA@IRMOF-3@MOF-5 after 1 hour of polymerization at 65 °C (blue).

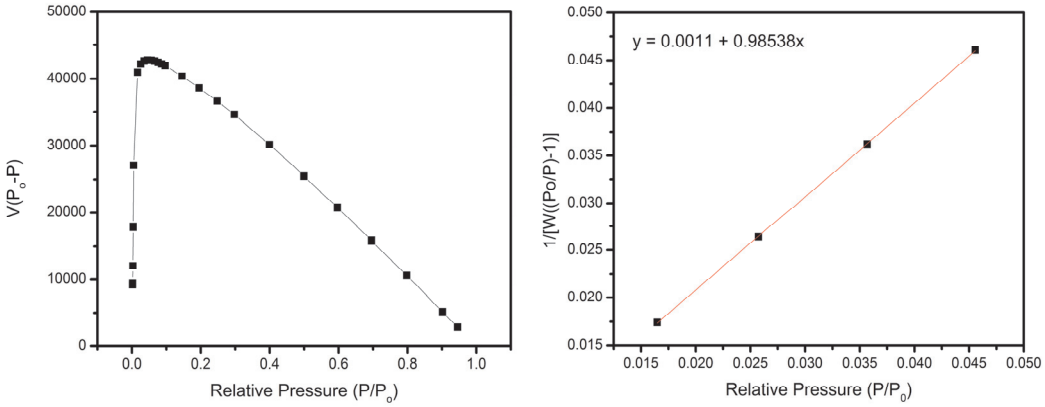

Figure 2.6. (left) Consistency criterion plot for determining the P/P_o range for BET analysis and (right) BET plot used to calculate the surface area of MOF-5 (3530 m^2g^{-1}).[35]

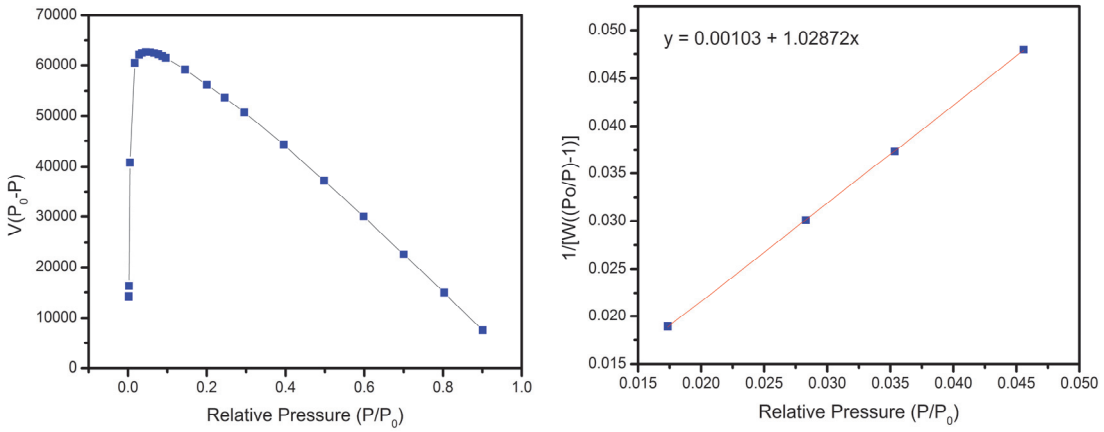

Figure 2.7. (left) Consistency criterion plot for determining the P/P_o range for BET analysis and (right) BET plot used to calculate the surface area of ICL@IRMOF-3@MOF-5 (3381 m^2g^{-1}).[35]

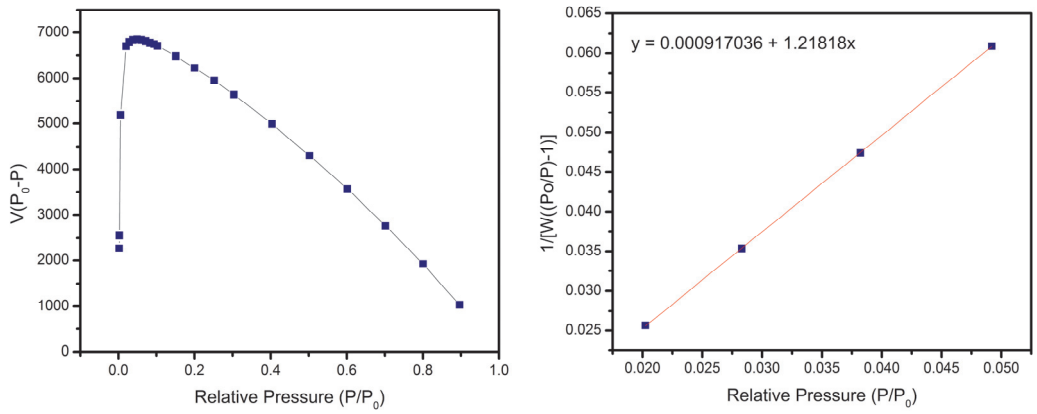

Figure 2.8 (left) Consistency criterion plot for determining the P/P_o range for BET analysis and (right) BET plot used to calculate the surface area of PMMA@IRMOF-3@MOF-5 (5 minutes polymerization) (2857 m^2g^{-1}). [35]

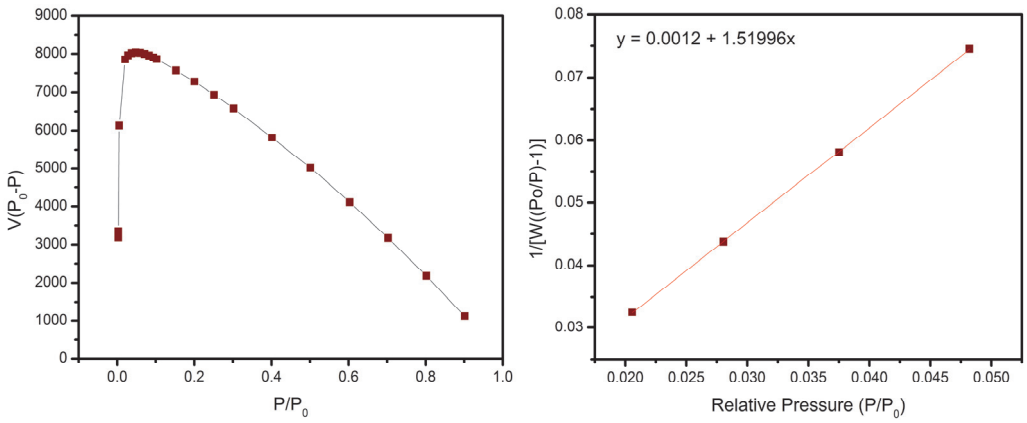

Figure 2.9. (left) Consistency criterion plot for determining the P/P_o range for BET analysis and (right) BET plot used to calculate the surface area of PMMA@IRMOF-3@MOF-5 (1 hour polymerization) (2289 m^2g^{-1}). [35]

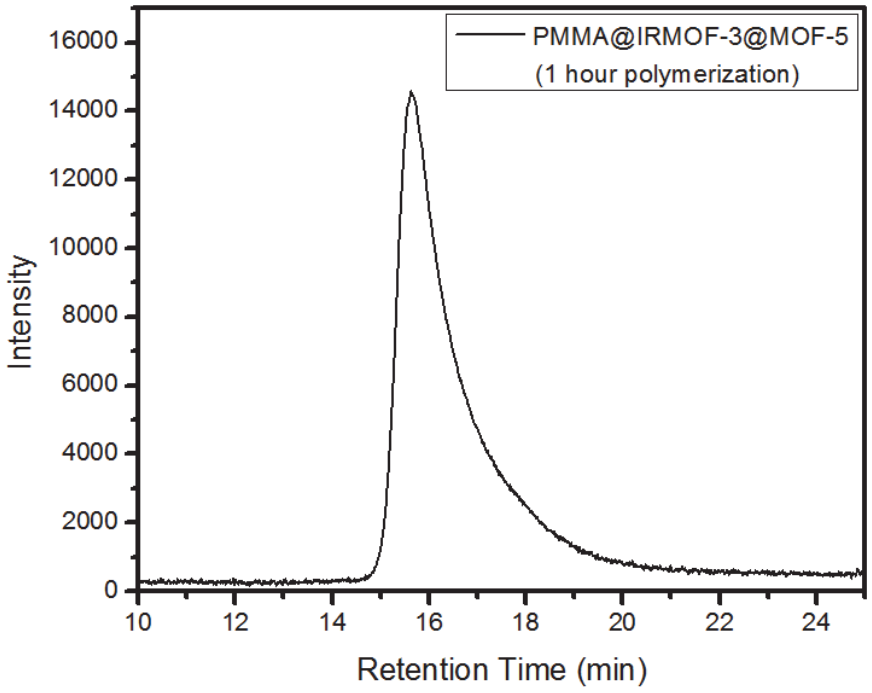

Figure 2.10. Example GPC of PMMA extracted from digested PMMA@IRMOF-3@MOF-5 after a 1 hour polymerization. The molecular weight of the resulting polymer was determined to have an Mn of 615 kDa with a polydispersity of 1.44. The molecular weight was determined at 218 nm from the UV-Vis detector with integration limits from 14.549 to 19.851 minutes.

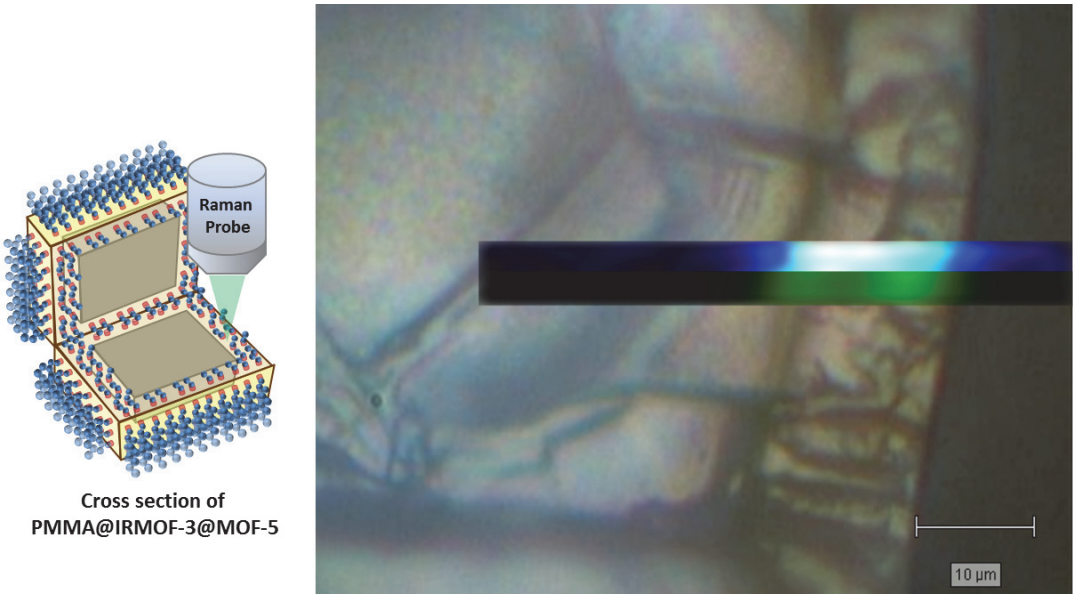

Figure 2.11. Raman mapping of PMMA@IRMOF-3@MOF-5 showing the signal to baseline ratio of the peak between 787 and 818 cm^{-1} (blue), representative of the CH_2 stretch on the backbone of poly(methyl methacrylate), and showing the intensity at 741 cm^{-1} (green), which shows the fluorescence characteristic of the IRMOF-3 shell. Polymer and shell are co-localized.

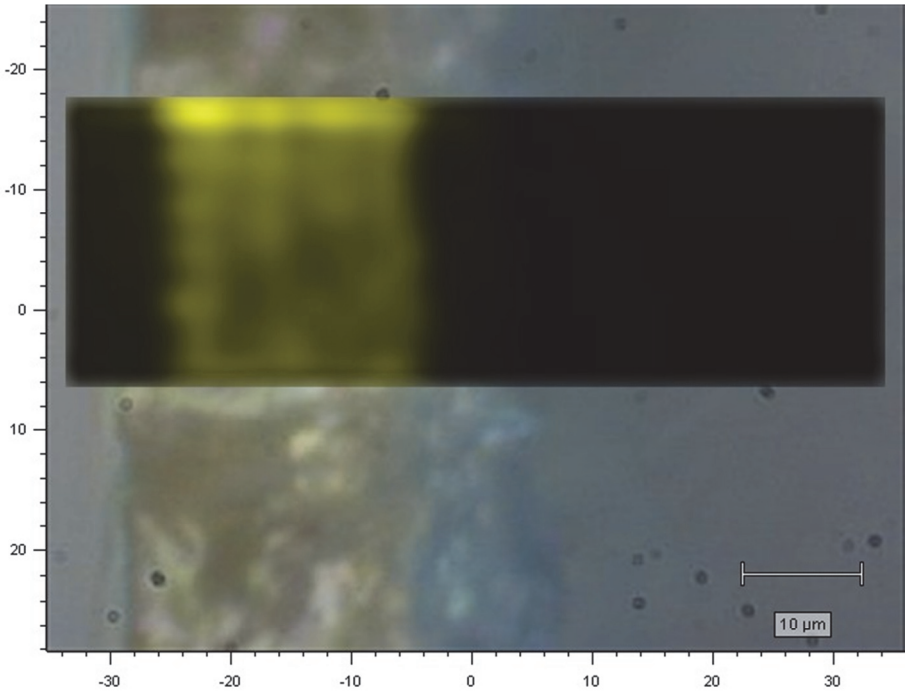

Figure 2.12. Raman mapping of IRMOF-3@MOF-5 showing the intensity at 1494 cm^{-1} representative of the fluorescence intensity of the IRMOF-3 shell.

2.6 References

(1) Yuan, W.; Lin, Y. S.; Yang, W. *J. Am. Chem. Soc.* **2004**, *126*, 4776.

(2) de Vos, R. M.; Verweij, H. *Science* **1998**, *279*, 1710.

(3) A.F. Ismail; L. I. B. David. *J. Membr. Sci.* **2001**, *193*, 1.

(4) S. Sircar; T. C. Golden; M. B. Rao. *Carbon.* **1996**, *34*, 1.

(5) Zimmerman, C. M.; Singh, A.; Koros, W. J. *J. Membr. Sci.* **1997**, *137*, 145.

(6) Balazs, A. C.; Emrick, T.; Russell, T. P. *Science.* **2006**, *314*, 1107.

(7) Celikbicak, O.; Bayramoglu, G.; Yılmaz, M.; Ersoy, G.; Bicak, N.; Salih, B.; Arica, M. Y. *Microporous Mesoporous Mater.* **2014**, *199*, 57.

(8) Sarsabili, M.; Parvini, M.; Salami-Kalajahi, M.; Ganjeh-Anzabi, P. *Adv. Polym. Tech.* **2013**, *32*, 21372.

(9) Kong, H.; Gao, C.; Yan, D. *J. Am. Chem. Soc.* **2004**, *126*, 412.

(10) Mitzi, D. B. *Chem. Mater.* **2001**, *13*, 3283.

(11) Gascon, J.; Kapteijn, F.; Zornoza, B.; Sebastián, V.; Casado, C.; Coronas, J. *Chem. Mater.* **2012**, *24*, 2829.

(12) Vinh-Thang, H.; Kaliaguine, K. *Chem. Rev.* **2013**, *113*, 4980.

(13) James, S. L. *Chem. Soc. Rev.* **2003**, *32*, 276.

(14) Eddaoudi, M.; Kim, J.; Rosi, N.; Vodak, D.; Wachter, J.; O'Keeffe, M.; Yaghi, O. M. *Science.* **2002**, *295*, 469.

(15) Park, T.-H; Koh, K.; Wong-Foy, A. G.; Matzger, A. J. *Cryst. Growth Des.* **2011**, *11*, 2059.

(16) Dutta, A.; Wong-Foy, A. G.; Matzger, A. J. *Chem. Sci.* **2014**, *5*, 3729.

(17) In the literature simple MOFs have, on occasion, been referred to as hybrid materials, inconsistent with the common use of "hybrid" to indicate two or more phases intimately mixed typically on nanometer length scales. This is, however, more of an issue of connotation than denotation, as many common definitions of hybrid materials are so absurdly broad that they encompass ferrocene and copper acetate in spite of the fact that their properties do not arise in any simple fashion from phases of the pure metal and ligand. The use of the term hybrid materials for MOFs has recently been discouraged by IUPAC: Pure Appl. Chem. **2013**; *85*, 1715.

(18) Shahid, S.; Nijmeijer, K. *J. Membr. Sci.* **2014**, *470*, 166.

(19) Zhang, Y.; Feng, X.; Li, H.; Chen, Y.; Zhao, J.; Wang, S.; Wang, L.; Wang, B. *Angew. Chem. Int. Ed.* **2015**, *54*, 4259.

(20) Huo, J.; Marcello, M.; Garai, A.; Bradshaw, D. *Adv. Mater.* **2013**, *25*, 2717.

(21) Zhang, R.; Ji, S.; Wang, N.; Wang, L.; Zhang, G.; Li, J.-R. *Angew. Chem. Int. Ed.* **2014**, *53*, 9775.

(22) O'Neill, L. D.; Zhang, H.; Bradshaw, D. *J. Mater. Chem.* **2010**, *20*, 5720.

(23) Zhao, D.; Tan, S.; Yuan, D.; Lu, W.; Rezenom, Y. H.; Jiang, H.; Wang, L.-Q.; Zhou, H.-C. *Adv. Mater.* **2011**, *23*, 90.

(24) Liu, H.; Zhu, H.; Zhu, S. *Macromol. Materi. Eng.* **2015**, *300*, 191.

(25) Lee, H. J.; Cho, W.; Oh, M. *Chem. Commun.* **2012**, *48*, 221.

(26) Li, A.-L.; Ke, F.; Qiu, L.-G.; Jiang, X.; Wang, Y.-M.; Tian, X.-Y. *CrystEngComm* **2013**, *15*, 3554.

(27) Koh, K.; Wong-Foy, A. G.; Matzger, A. J. *Chem. Commun.* **2009**, 6162.

(28) Koh, K. M.; Wong-Foy, A. G.; Matzger, A. J.; Benin, A. I.; Willis, R. R. Block Coordination Copolymers. United States Patent US 8324323 B2, 2012

(29) Zacher, D.; Nayuk, R.; Schweins, R.; Fischer, R. A.; Huber, K. *Cryst. Growth Des.* **2014**, *14*, 4859.

(30) Cubillas, P.; Anderson, M. W.; Attfield, M. P. *Cryst. Growth Des.* **2013**, *13*, 4526.

(31) Matyjaszewski, K.; Xia, J. *Chem. Rev.* **2001**, *101*, 2921.

(32) Wang, Z.; Cohen, S. M. *J. Am. Chem. Soc.* **2007**, *129*, 12368.

(33) Matyjaszewski, K. *Macromolecules* **2012**, *45*, 4015.

(34) Feldblyum, J. I.; Wong-Foy, A. G.; Matzger, A. J. *Chem. Commun.* **2012**, *48*, 9828.

(35) Walton, K. S.; Snurr, R. Q. *J. Am. Chem. Soc.* **2007**, *129*, 8552.

CHAPTER III

MOF-5-Polystyrene: direct production from monomer, improved hydrolytic stability, and unique guest adsorption‡

3.1 Introduction

Metal-organic frameworks (MOFs) hybridized with organic polymers are an emerging class of composite materials with potential to combine properties sought after in industrial separation processes.[1-13] MOFs are useful to gain defined porosities with high surface areas, crystallinity, regularity, topological diversity, and ability to tune functionality.[14-20] However, these crystalline materials have poor mechanical properties and are challenging to process.[21,22] Organic polymers have the potential to impart hydrolytic stability, processability, and compatibility with organic phases to MOFs. Thus, such MOF-polymer composites, including membranes, are of interest for a wide variety of adsorption and separation applications.[23-31]

For optimal performance of MOF-polymer composite membranes, a high compatibility between the MOF and the organic polymer phase is important. The common methods of incorporating MOFs into polymer matrices suffer from poor MOF-polymer adhesion, interfacial voids, and MOF particle aggregation.[32-34] Several synthetic attempts have been made to modify the surface of the MOFs and/or polymers to covalently link them for enhancing the compatibility between the polymer matrices and MOFs.[35-38] Previously, we successfully performed surface modification of MOFs for covalent polymer attachment and also retained a high surface area (2289–2857 m^2g^{-1}) in the polymer-MOF composite by adopting a core-shell architecture.[39] In addition to being somewhat laborious, the core shell approach dictates that only kinetic selectivities can be obtained in a separation process because the bulk of the material is unfunctionalized.

‡ Gamage, N.-D. H.; McDonald, K. A.; Matzger, A. J. *Angew. Chem. Int. Ed*. **2016**, *55*, 12099. Adapted from Wiley-VCH.

Imperfections in the polymer shell compromise even this kinetic selectivity, and in practice, only marginal gains in hydrolytic stability were observed in spite of using hydrophobic polymers and such results are inferior to simple silicone polymer coatings or polymer-grafted linkers.[14,24,36,40] Herein, we report the synthesis of a MOF-5-PS composite material with a uniform distribution of strongly bound polystyrene, formed by a simple, initiator-free synthesis. The MOF-5-PS composite is formed by heating neat styrene in the presence of MOF-5 at 65 °C. The material produced after 24 hours of heating (MOF-5-PS-24 h) gains remarkable hydrolytic stability over pristine MOF-5. Dye and CO_2 gas adsorption properties of this composite demonstrate that polystyrene grafting significantly alters the physical and chemical properties of pristine MOF-5.

3.2 Results and Discussion

An appreciable content of polystyrene was grafted onto MOF-5 crystals by heating in neat pure styrene for at least ~4 h at 65 °C. Styrene was heated for 4, 5, 8, 16, and 24 h at 65 °C in the presence of MOF-5 to obtain MOF-5-PS-4–24 h composites with increasing polymer contents (Figure 3.1). This strongly bound polystyrene is retained in the MOF-5-PS composites even after heating at 60 °C in THF. Physisorbed high molecular weight polystyrene is removed under such conditions from the MOF-5 crystals based on our control experiments.

Polymerization of styrene in the presence of MOF-5 at 65 °C up to 24 h does not alter the crystallinity of MOF-5 according to powder X-ray diffraction (PXRD, Figure 3.2). The weight percentages of polystyrene in the MOF-5-PS composites were investigated using thermogravimetric analysis (TGA) to observe mass loss corresponding to depolymerization of polystyrene. The TGA curves of MOF-5-PS-4–24 h samples and as synthesized MOF-5 are shown in Figure 3.3. The depolymerization of polymer is well separated from MOF decomposition enabling facile quantification of loading (Figures 3.4-3.6).

The weight percentage of polystyrene in the composite crystals increases with increased duration of heating in styrene (Figure 3.3). There is approximately 9.4–30.0 wt.% polystyrene grafted in the MOF-5-PS composite after 4–24 h of polymerization at

65 °C (Table 3.1). Thus, the weight percentage of polystyrene in MOF-5-PS composites can be tuned by changing the duration of heating styrene in the presence of MOF-5.

N_2 sorption isotherms of the MOF-5-PS composites after 4, 5, 8, 16, and 24 h of polymerization of styrene are shown in Figure 3.7. The corresponding surface areas obtained by applying the BET approximation[41] to the data obtained from N_2 sorption experiments are shown in Table 3.1. Increasing the duration of heating styrene in the presence of MOF-5 leads to more polystyrene grafting and thus, reduction of surface area. The surface areas of MOF-5-PS composites are in the range of 2780–1611 m^2/g after 4–24 h of polymerization of styrene at 65 °C. As the percentage of MOF-5 in the composite decreases there is a linear decrease of BET surface area (Correlation graphs of the surface areas obtained for the MOF-5-PS composites to the duration of heating and the percentage of MOF-5 are shown in Figure 3.8).

Complete digestion of the MOF-5-PS composites in 1 M NaOH was not possible due to high hydrophobicity. However, after basic treatment, it was possible to dissolve polymer in THF to allow characterization of the polymer molecular weight and molecular weight distribution by gel permeation chromatography (GPC). After 24 h of polymerization of styrene in the presence of MOF-5 at 65 °C, a high molecular weight polymer of 577 kDa (M_n) was extracted from the digested MOF-5-PS composite with a dispersity (Đ) of 1.31 (Figure 3.9). Similar high molecular weight polymers with approximately similar dispersities were observed by GPC from the MOF-5-PS samples after 4, 5, 8, and 16 h of polymerization of styrene at 65 °C (Table 3.2).

The high molecular weight of polystyrene precludes polymer isolation within a single pore of MOF-5. Indeed, approximation using the bulk density of polystyrene indicates that a chain of no more than twelve repeat units could fit in a single MOF-5 pore with a diameter of 12.5 Å. If stretched to a totally linear conformation, an oligomer of only five repeat units could sit inside a pore. At the molecular weight of 577 kDa, a polystyrene chain has a diameter of 12 nm and has a volume equivalent to ~500 MOF-5 pores (see Section 3.4). By contrast, if stretched to a totally linear conformation, this polystyrene would occupy ~1100 pores of MOF-5 (see Section 3.4). As shown below, the behavior of the polymer lies between these extremes.

The presence of polystyrene in the MOF-5-PS composites was confirmed by Raman microspectroscopy. In addition to characteristic signals of MOF-5,[42] Raman peaks at 1001 and 1030 cm^{-1} corresponding to the breathing mode of the aromatic carbon ring and bending modes of C–H bonds of polystyrene, respectively were present (Figures 3.10 and 3.11). A Raman mapping experiment was performed on a sectioned MOF-5-PS-24 h crystal embedded in epoxy to study the distribution of polystyrene by examining the distribution of the 1001 cm^{-1} peak. According to the Raman mapping image and the white light image (Figure 3.12a and 3.12b, respectively) polystyrene is uniformly distributed throughout the MOF-5 crystal.

Though the micron scale uniformity of polystyrene distribution is clearly shown by Raman mapping, what is occurring on the level of the pores is not observable directly. Therefore, the pore size distributions of MOF-5-PS composites were obtained by applying the non-local density functional theory (NLDFT)[43,44] with the cylindrical pore model and using the DFT and Monte Carlo approximation to the data obtained from Ar sorption experiments. A pore size distribution plot of the MOF-5- PS-24 h composite is shown in comparison to the pore size distribution of pristine MOF-5 in Figure 4 (Pore size distribution plots for MOF-5-PS-4–16 h composites are shown in Figures 3.13 and 3.14). Pristine MOF-5 mostly contains pore widths of approximately 12.5 Å. After grafting polystyrene using the polymerization process for 24 h there is a reduction in the content of pores of 12.5 Å and the major pore width obtained is approximately 11.5 Å. Smaller pore widths in the range of 5.2–9.6 Å that are absent in pristine MOF-5 were observed for the MOF-5-PS composites. The pore size distribution of MOF-5-PS composites shifts towards the range of 5.2–11.5 Å when the duration of heating styrene is increased (Figures 3.13 and 3.14). Taken together with the Raman mapping data, this indicates that as the polymer loading increases, polystyrene is distributed throughout the available pore space and unoccupied pores are very rare. Thus, the MOF-5-PS composite material obtained via this simple synthetic protocol alters the material sufficiently that the composites may show unique sorption properties in which the thermodynamics of adsorption are altered rather than only the kinetics.

The hydrolytic stability of the MOF-5-PS-24 h and pristine MOF-5 were studied after keeping the corresponding crystals at 53% relative humidity (RH). Based on the

PXRD patterns, pristine MOF-5 degraded within 4 h whereas the MOF-5-PS composite was stable for > 3 months (Figures 3.15 and 3.16). This is consistent with previous reports for degradation rates of MOF-5.[45] Surface area obtained by applying the BET approximation to the data obtained from N_2 sorption of the MOF-5-PS composite after 3 months under 53% RH was 1556 m^2/g, which indicates that there is no significant reduction in the porosity of the composite (Figure 3.17). Thus, a dramatic improvement in hydrolytic stability was achieved with this novel MOF-5-PS composite and this argues strongly for a drastic change in the chemical environment within the pores.

To probe changes in polarity of the pore environment of MOF-5-PS-24 h composite versus pristine MOF-5, dye adsorption studies were performed. Solvatochromic behavior between a dye adsorbed in MOF-5-PS-24 and pristine MOF-5 can be employed to determine changes in surface polarity. Chosen dyes were methyl red and nile red due to their ability to diffuse into constricted pores. The microscopic images of methyl red and nile red adsorbed to MOF-5-PS and MOF-5 crystals and the solid state UV-Visible spectra are shown in Figure 3.18. Based on the solid state UV-visible spectra, both methyl red and nile red adsorbed in MOF-5-PS-24 h show blue shifted centroids of the peak envelopes with respect to the dyes adsorbed on pristine MOF-5. In both cases this is consistent with a less polar environment in the pores upon incorporation of polymer. This conclusion is based on previous studies of solvent polarity effects on the absorption maxima for methyl red and nile red.[46,47] Hence, the chemical and physical properties of MOF-5 has significantly changed with the uniform distribution of polystyrene in the MOF-5-PS-24 h composite.

Variations in the pore environment of MOF-5-PS-24 h composite versus pristine MOF-5 were further analyzed by CO_2 adsorption studies. The CO_2 adsorption isotherms obtained at 1 atm and 298 and 273 K are shown in Figure 3.19. Impressively, the CO_2 adsorption capacity of the MOF-5-PS-24 h composite is greater than pristine MOF-5 at both temperatures in spite of the lower surface area of the MOF-5-PS-24 h composite. The higher CO_2 adsorption capacities can be attributed to the change of the pore environment with partial pore filling by polystyrene. Thus, the pore environment is significantly altered in the MOF-5-PS-24 h composite with respect to pristine MOF-5.

Although a mechanistic understanding of the origin of grafting in MOF-5-PS has yet to be achieved, some observations are worth noting. Methyl methacrylate (MMA) does not form a grafted polymer with MOF-5 at 65 °C and thus, required initiator grafting.[39] Styrene is different than MMA in several key aspects. Pure styrene is known to undergo self- initiated thermal polymerization at a rate of 0.1% per hour at 60 °C in the absence of initiators.[48-51] Styrene is one of the few monomers known to undergo self-initiated thermal polymerization in the absence of impurities. According to the proposed Mayo mechanism,[48] the self-initiated thermal polymerization of styrene is an initiator-free radical based process. There have been reports of experimental evidence[49,52-54] as well as theoretical studies[51] for the occurrence of the Mayo mechanism. High molecular weight polymers with similar dispersities were observed when neat styrene was polymerized in the presence of MOF-5 for varying durations or in the absence of MOF-5. However, styrene is also prone to cationic polymerization and the potential role of defects in such an initiation merits investigations. Mechanistic investigations of the styrene polymerization process and grafting of polystyrene are underway.

The synthetic protocol described herein can be used with other MOFs such as IRMOF-3. Also, functionalized styrene monomers such as 4-bromo styrene can be used to obtain polymer grafted MOF-5-PS composites. Thus, this method can be employed to obtain versatile MOF and polymer composites with various chemical and physical properties.

3.3 Conclusions

In conclusion, we have obtained a novel MOF-5-PS composite material through a simple synthetic protocol avoiding laborious synthetic modification and polymerization initiators. The MOF-5-PS-24 h composite is much greater in hydrolytic stability (> 3 months) with respect to pristine MOF-5 (4 h) at the relative humidity of 53%. The solvatochromic behavior of methyl red and nile red dyes adsorbed on MOF-5-PS-24 h versus pristine MOF-5 demonstrates that the pore environment of MOF-5 is significantly changed after the polymer grafting. The MOF-5-PS-24 h composite also has higher CO_2 adsorption capacities at 1 atm and 298 and 273 K with respect to pristine MOF-5 due to the significantly altered pore environment. Realizing such dramatic changes in properties

after grafting polystyrene onto MOFs with this simple protocol allows versatile metal-organic framework and polymer composite materials for a wide variety of adsorption and separation applications.

3.4 Experimental Methods

Starting Reagents: Zinc nitrate hexahydrate (Fisher Scientific, ACS reagent), 1,4-benzenedicarboxylic acid (H_2BDC, Fisher Scientific, 98%), dichloromethane (CH_2Cl_2, Fisher Scientific, > 99.9%), xylenes (Sigma-Aldrich, > 98.5%, ACS reagent), tetrahydrofuran (THF, Fisher Scientific, ACS and HPLC grades), dimethylformamide (DMF, Fisher Scientific, > 99.5%), sodium hydroxide (NaOH, Fisher Scientific, ACS reagent), sodium chloride (NaCl, Fisher Scientific, ACS reagent), sodium sulfate, anhydrous (Na_2SO_4, Acros Organics, ACS reagent), and hydrochloric acid (HCl, 36.5–38.0% w/w, Fisher Scientific, certified ACS plus) were used as received without further purification. Diethylformamide (DEF, TCI America, > 99.0%) was purified by storing over activated carbon for ~1 month and subsequently passing through a column containing silica gel. Styrene (stabilized and N_2 flushed, Acros Organics, 99.5%) was purified by passing through a column of *t*-Butyl catechol remover (chromatographic packing, Scientific Polymer Products Inc.) and consequently filtering through a CHROMAFIL® Xtra PTFE-45/13 0.45 µm disposable syringe filter. Nile red (Acros Organics, 99%, pure) and methyl red (Acros Organics, pure, ACS reagent) organic dyes were used as purchased.

Synthesis:

Zinc nitrate tetrahydrate, $Zn(NO_3)_2{\cdot}4H_2O$: Zinc nitrate tetrahydrate was prepared as previously described.[54]

MOF-5: MOF-5 was synthesized based on a slightly modified previously published procedure.[39] H_2BDC (0.100 g, 0.602 mmol), $Zn(NO_3)_2{\cdot}4H_2O$ (0.500 g, 1.91 mmol), and 15 mL of DEF were added to a 20 mL vial. The mixture was sonicated for 15 minutes until all the solid materials were dissolved and heated to 100 °C for 18–24 hours to obtain colorless cubic crystals of MOF-5. The DEF solution was decanted and MOF-5 crystals were washed with DEF ((i) 3 × 10 mL; (ii) kept on an IKA® vibrax VXR basic shaker at

100 rpm in 10 mL of fresh DEF over 24 h) and CH_2Cl_2 ((i) 3 × 10 mL; (ii) kept on an IKA® vibrax VXR basic shaker at 100 rpm in 10 mL of fresh CH_2Cl_2 over 24 h). The resultant MOF-5 crystals were activated by exposure to dynamic vacuum (10^{-2} Torr) for 24 h and were stored in a glove box under an atmosphere of nitrogen.

MOF-5-PS-4–24 h: MOF-5 crystals (0.100 g) and purified styrene (10 mL) were added to a 20 mL vial and the mixture was heated at 65 °C for 4–24 h to obtain colorless MOF-5-PS-4–24 h composite crystals. Afterwards, the styrene solution was decanted and MOF-5-PS-4–24 h crystals were washed with THF ((i) 3 × 10 mL; (ii) kept on an IKA® vibrax VXR basic shaker at 100 rpm in 10 mL of fresh THF over 24 h) and CH_2Cl_2 ((i) 3 × 10 mL; (ii) kept on an IKA® vibrax VXR basic shaker at 100 rpm in 10 mL of fresh CH_2Cl_2 over 24 h). The resultant MOF-5-PS-4–24 h crystals were activated by exposure to dynamic vacuum (10^{-2} Torr) for 24 h and were stored in a glove box under an atmosphere of nitrogen.

Extraction of polystyrene on MOF-5-PS-4–24 h composites:

Method 1: MOF-5-PS-4–24 h composite was vigorously shaken in 1 M NaOH (10 mL) for 5–10 min. and sonicated further for 5–10 min. The NaOH solution was decanted and the resultant material was washed with (i) saturated NaCl (2 × 10 mL), (ii) distilled H_2O (2 × 10 mL), and (iii) acetone (2 × 1 mL). The residual solvent was removed under reduced pressure and the resultant partially degraded MOF-5-PS-4–24 h composite was kept in THF (1.8 mg/mL) for 5–10 min. and also sonicated for 5–10 min. The dispersed mixture obtained was filtered through a CHROMAFIL® Xtra PTFE-45/13 0.45 μm disposable syringe filter. Finally, a gel permeation chromatography (GPC) trace was obtained to determine the polymer molecular weight and dispersity (Đ).

Method 2: MOF-5-PS-4–24 h composite was ground until a uniform powder was obtained and then, this powder was vigorously shaken in 1 M NaOH (10 mL) for 5–10 min. and sonicated further for 5–10 min. Afterwards, the polymer was extracted to CH_2Cl_2 (10 mL) in a separatory funnel. This CH_2Cl_2 layer was separated from the aqueous layer and was washed with saturated NaCl (3 × 10 mL). Then, the CH_2Cl_2 layer

was separated and dried with anhydrous Na_2SO_4. Finally, the dry CH_2Cl_2 layer was decanted and the solvent was removed under reduced pressure to obtain the extracted polystyrene. This polystyrene was dissolved in THF (1 mg/mL) and was filtered through a CHROMAFIL® Xtra PTFE-45/13 0.45 µm disposable syringe filter. A gel permeation chromatography (GPC) trace was obtained to determine the polymer molecular weight and Đ.

There was no significant difference in the measured polymer molecular weights and dispersities measured by the two different methods.

Determination of polystyrene retention:

(i) Polymer retention after the washing procedure:

(a) Analysis of the final (CH_2Cl_2) wash solution: The final CH_2Cl_2 solution (10 mL) that was used to wash MOF-5-PS crystals (0.100 g) over 24 h on the shaker was dried on the Schlenk line under reduced pressure. Then, the residue was dissolved in THF (1 mg/mL) and filtered through a CHROMAFIL® Xtra PTFE-45/13 0.45 µm disposable syringe filter. Finally, a GPC trace was collected and there was no polystyrene in the final (CH_2Cl_2) wash solution, which indicates there was no polymer coming off from the MOF-5-PS-24 h composite in to the CH_2Cl_2 washing solvent.

(b) Analysis of extracted polystyrene from MOF-5-PS-24 h after the washing procedure: After the washing procedure mentioned in (a) and activation, the presence of polymer on the MOF-5-PS-24 h composite was confirmed using TGA and Raman Spectroscopy. The grafted polystyrene was studied by GPC after it was extracted from the digested MOF-5-PS-24 h composite using the above mentioned extraction method 2. Based on GPC, a polymer of 594 kDa was observed with a Đ of 1.35.

The observations in (a) and (b) indicate that the high molecular weight polymer was grafted and was not washed by the washing procedure with THF and CH_2Cl_2 mentioned above in the MOF-5-PS-24 h composite synthesis.

(ii) Polymer retention after heating in THF at 60 °C:

(a) Analysis of polymer after heating in THF at 60 °C: To a 20 mL vial, a sample of washed and activated MOF-5-PS-24 h composite (0.432 g) and THF (10 mL) was added

and the mixture was kept shaking at 60 °C on a Glas-Col® pulse vortex mixer/heater (Terre Haute, USA). Afterwards, the THF was decanted, allowed to come to room temperature, and was filtered through a CHROMAFIL® Xtra PTFE-45/13 0.45 μm disposable syringe filter. A GPC trace was obtained and there was no polymer, which indicated that no polymer was coming off from the MOF-5-PS-24 h composite in to THF at 60 °C.

(b) Analysis of extracted polystyrene from MOF-5-PS-24 h after heating in THF: After heating in THF at 60 °C as mentioned in (a) and activation, the presence of polymer on the corresponding MOF-5-PS-24 h composite was confirmed using TGA and Raman Spectroscopy. The grafted polystyrene was studied by GPC after it was extracted from the digested MOF-5-PS-24 h composite using the above mentioned extraction method 2. Based on GPC, a high molecular weight polymer of 541 kDa was observed with a Đ of 1.41.

The observations in (a) and (b) indicate that the high molecular weight polymer was grafted and was not washed by heating in THF at 60 °C.

Feasibility of high molecular weight polystyrene entrapment in MOF-5:

To each of three 20 mL vials, high molecular weight polystyrene (Mw = 280 kDa, ~0.100 g) was added. Polystyrene was dissolved in (i) THF, (ii) Xylenes, or (iii) DCM (5 mL) by sonication in separate vials. Then, MOF-5 (~0.010 g) was added to each vial and the corresponding mixtures were heated at 65 °C for 24 h. Afterwards, the solutions were decanted and the resultant MOF-5 crystals were washed with THF ((i) 3 × 10 mL; (ii) kept on an IKA® vibrax VXR basic shaker at 100 rpm in 10 mL of fresh THF over 24 h) and CH_2Cl_2 ((i) 3 × 10 mL; (ii) kept on an IKA® vibrax VXR basic shaker at 100 rpm in 10 mL of fresh CH_2Cl_2 over 24 h). These washed crystals were activated by exposure to dynamic vacuum (10^{-2} Torr). No polystyrene was observed based on Raman Spectroscopy, TGA, and GPC (after digestion of MOF-5 with the extraction method 2), which indicates that high molecular weight polymer does not directly graft onto, or otherwise become strongly associated with, MOF-5 crystals under the same conditions of MOF-5-PS-4–24 h composite synthesis. If there are physisorbed high molecular weight

polymers with MOF-5 crystals, they get completely washed away during the washing procedure.

Study of hydrolytic stability:

The hydrolytic stability measurements were performed using saturated salt solutions of K_2CO_3 in distilled H_2O (in 20 mL vials) to provide an environment of 53% relative humidity (RH).[45] To two 4 mL vials, MOF-5 (~0.020 mg) and MOF-5-PS-24 h (~0.020 mg) were added and then, they were quickly incorporated in to 20 mL vials with the saturated K_2CO_3 solution and sealed. After different time points, crystals of MOF-5 and MOF-5-PS-24 h were harvested and any effects on their crystallinity was analysed by powder X-ray diffraction (PXRD, Figures 3.15 and 3.16, respectively). Based on the PXRD patterns, pristine MOF-5 degraded within 4 h whereas the MOF-5-PS-24 h composite was stable for > 3 months (12 weeks) at 53% RH, which indicates that grafting of polystyrene using this simple protocol results in a significant enhancement of the hydrolytic stability. For N_2 gas sorption results confirming maintenance of porosity see below (Figure 3.17).

Dye sorption experiments:

Saturated methyl red and nile red dye solutions were prepared in CH_2Cl_2 (1–2 mL) using two 4 mL vials. The MOF-5-PS-24 h composite (~0.010 mg, after the CH_2Cl_2 wash, without activation) was added to each vial and the mixture was kept on an IKA® vibrax VXR basic shaker at 100 rpm for 24 h. Afterwards, the dye solutions were decanted and the dye adsorbed MOF-5-PS-24 h composites were washed with fresh CH_2Cl_2 (2 × 5 mL) and activated by exposure to dynamic vacuum (10^{-2} Torr) for 24 h and were stored in a glove box under an atmosphere of nitrogen.

Instrumental analysis:

Powder X-ray diffraction: Powder X-ray diffraction (PXRD) data for MOF-5 and MOF-5-PS composites were collected on a Rigaku R-axis Spider diffractometer with an image plate detector and Cu-Kα radiation (graphite monochromated, 1.5406 Å). The data collection was carried out operating at 40 kV and 44 mA in the transmission mode.

Images were collected with χ fixed at 45° while the sample loop was rotated at 10°/min in ϕ on the goniometer and ω oscillating between 5° and 50° to minimize any effect of preferred orientation. Then, by integration of the resulting two-dimensional images using the AreaMax (2.0) software package with a step size of 0.1 in 2θ, the PXRD patterns were obtained.

Gas sorption measurements: Nitrogen gas sorption experiments of MOF-5 and MOF-5-PS composites were obtained using a NOVA *e*-series 4200 surface area analyser from Quantachrome Instruments (Boynton Beach, Florida, USA). Ultra-high purity N_2 (99.999%) was purchased from Cryogenic Gases and used as received. N_2 sorption experiments were carried out at 77 K in a glass sample cell with approximately 15–20 mg of sample. The N_2 Sorption isotherms were obtained and analysed by applying the BET approximation using the NOVAwin software.

Argon and CO_2 sorption experiments were carried out using an AUTOSORB-1C gas sorption analyser from Quantachrome Instruments (Boynton Beach, Florida, USA). Liquid Argon (99.999%) and CO_2 (Bone Dry or 99.9%) were purchased from Cryogenic Gases and used as received. The argon sorption measurements were carried out at 87 K in a glass sample cell with approximately 10 mg of sample. The CO_2 sorption measurements were carried out at 298 K and 273 K in a glass sample cell with approximately 100 mg of sample. Pore size distributions of MOF-5 and MOF-5-PS composites were obtained by applying the non-local density functional theory (NLDFT) with a zeolite/silica equilibrium kernel using the cylindrical pore model by employing the ASWin software package (version 1.2).

Thermogravimetric Analysis (TGA): Thermogravimetric analyses of MOF-5 and MOF-5-PS composites were performed on a TA Instruments Q50 thermogravimetric analyser. The analyte was heated from room temperature (~25 °C) to 600 °C at a rate of 10 °C/min using platinum pans under a flow of nitrogen gas.

Gel permeation chromatography (GPC): Analyses of the polystyrene extracted from the MOF-5-PS-24 h composites were performed on a Shimadzu GPC with a molecular

weight range coverage of 1,000,000 to 92 Da. THF was used as the solvent and the sample concentrations were adjusted to be ~1–1.8 mg/mL. GPC was performed in the batch processing mode with a solvent flow rate of 1 mL/min and the spectra were obtained using a diode array UV-vis detector at 259 nm wavelength. These GPC analyses were performed and analysed using Shimadzu LCsolution software.

Raman Spectroscopy: Single point Raman spectra of MOF-5 and MOF-5-PS-4–24 h composites were obtained using a Renishaw inVia Raman microscope equipped with a RenCan CCD detector, Leica microscope, 633 nm laser, 1800 lines/mm grating, and 65 μm slit. Calibration of the instrument was performed using a silicon standard for all experiments. For collecting data, the extended scan mode was used in the range of 100–3200 cm^{-1}. The spectra were analysed using the Wire 3.4 software package.

Raman mapping of a sectioned MOF-5-PS-24 h composite embedded in epoxy, was performed on a Renishaw inVia Raman microscope equipped with a Renishaw 1" CCD array detector, Leica microscope, 785 nm laser, and a 65 μm slit in the streamline image acquisition mode. A region of the cross-section that includes the sectioned MOF-5-PS-24 h crystal and the epoxy background were selected for analysis. The spectra were collected using a static scan mode in the range of 555–1679 cm^{-1}. The mapping image was analysed using the Wire 4.2 software package.

Solid-state UV-visible (UV-vis) spectroscopy: UV-vis spectra of methyl red and nile red dye adsorbed MOF-5 and MOF-5-PS-24 h composite were performed on a double beam Varian Cary 5000 UV-vis-NIR spectrophotometer in the reflectance mode (%R). Spectra were scanned at a rate of 600 nm/min within the wavelength range of 200–2500 nm. Instrument baseline was set to zero using powdered barium sulphate ($BaSO_4$). The dye adsorbed MOF-5 and MOF-5-PS-24 h crystals (~10 mg) were mixed with $BaSO_4$ (~20 mg) and ground together to obtain a homogeneous solid mixture for analysis. The spectral data obtained in the reflectance mode were converted to transmission mode, F(R) using the Kubelka-Munk theory of reflectance by employing the Varian Cary WinUV Scan software version 3.0.

Calculation of the distribution of polystyrene through the MOF-5 network

(i) The number of repeating units (*n*) of bulk polystyrene that fit a single pore of MOF-5

- Bulk density of polystyrene = 1.04 g/mL
- MOF-5 pore diameter based on the argon pore size distribution measurements = 1.25 nm
- Molecular weight of styrene = 104.1 g/moL

The number of repeating units that fit a single pore of MOF-5 at maximum density, ***n***, is given by;

$$\frac{\boldsymbol{n} \times 104.1\ g/mol}{1.04\ g/cm^3} \times \frac{1}{6.022 \times 10^{23}\ mol^{-1}} \times \frac{10^{21}\ nm^3}{1\ cm^3} = (1.25\ nm)^3$$

$$\boldsymbol{n} \approx 12$$

(ii) The number of pores of MOF-5 filled by bulk polystyrene of M_n = 577 kDa

The volume of bulk polystyrene of M_n = 577 kDa is given by;

$$\frac{577{,}000\ g/mol}{1.04\ g/cm^3} \times \frac{1}{6.022 \times 10^{23}\ mol^{-1}} \times \frac{10^{21}\ nm^3}{1\ cm^3} = 921\ nm^3$$

Thus, the diameter (**d**) of bulk polystyrene of M_n = 577 kDa is given by;

$$\boldsymbol{d} = 2\left(\frac{921\ nm \times 3}{4\pi}\right)^{1/3} = 12\ nm$$

The number of pores of MOF-5 filled by bulk polystyrene of M_n = 577 kDa is given by;

$$\frac{921\ nm^3}{(1.25\ nm)^3} \approx 472$$

(iii) The number of repeating units of polystyrene that is stretched to a totally linear conformation that can fit a single pore of MOF-5

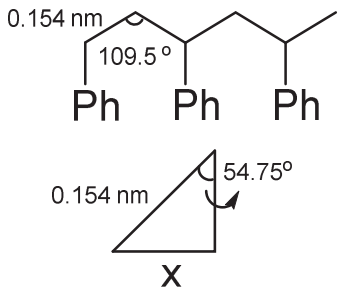

Sin 54.75^o = x/0.154 nm

X = 0.126 nm

The length of each repeating unit = 2x = 0.252 nm

The number of repeating units that can fit a single pore of MOF-5 = 1.25/0.252 ≈ 5

(iv) The number of pores of MOF-5 that can be filled by polystyrene of M_n = 577 kDa that is stretched to a totally linear conformation

The number of repeating units in polystyrene of M_n = 577 kDa is given by;

$$\frac{577{,}000}{104.1} = 5543$$

Based on (iii), the length of each repeating unit = 0.252 nm

Thus, the length of the stretched polystyrene = 5543 x 0.252 = 1397 nm

Hence, the number of pores of MOF-5 that can be filled = 1397/1.25 nm = 1117

3.5 Figures

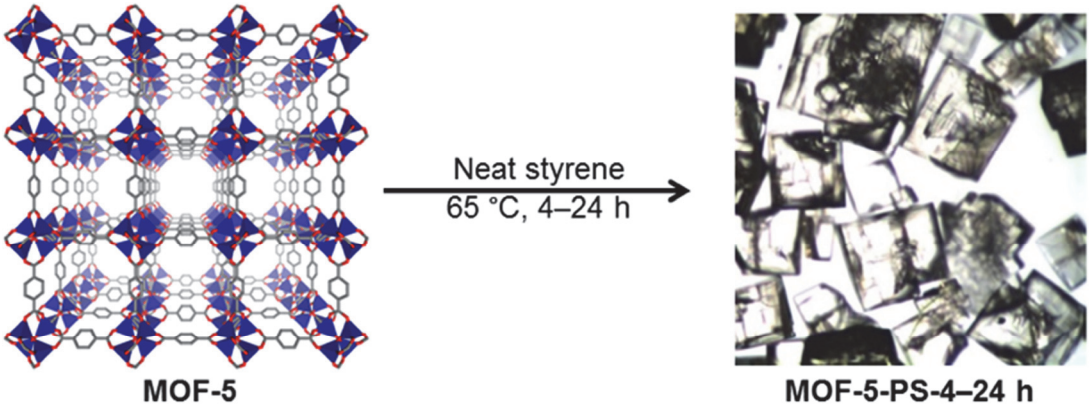

Figure 3.1. Synthetic scheme for direct production of MOF-5-PS-4–24 h composites from monomer.

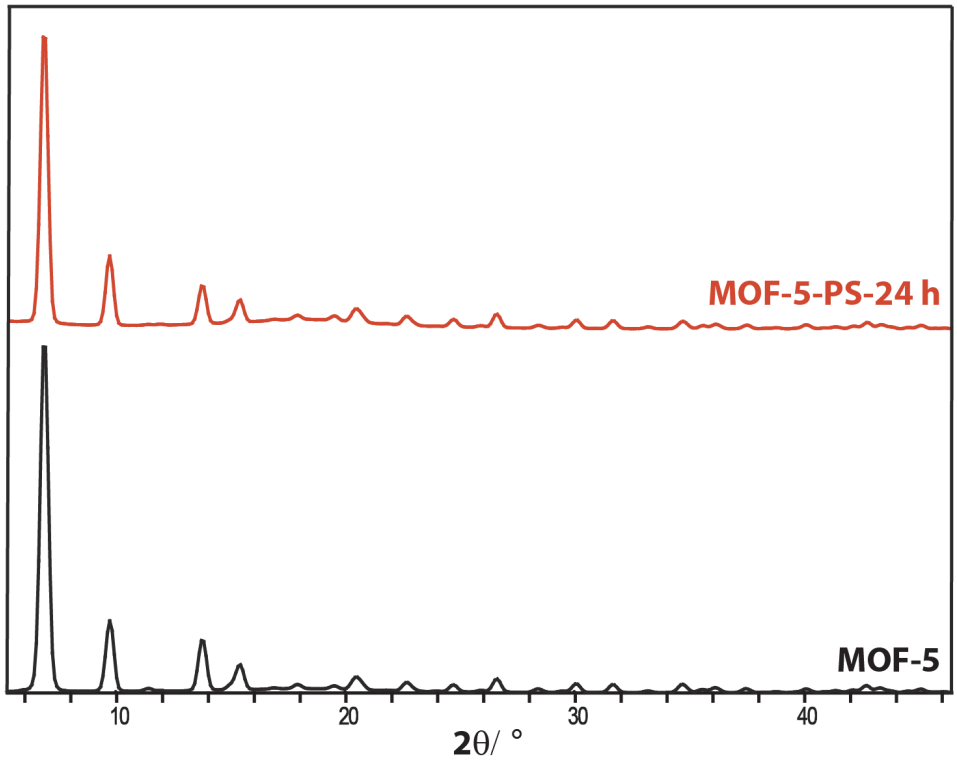

Figure 3.2. PXRD patterns of pristine MOF-5 and MOF-5-PS-24 h composite

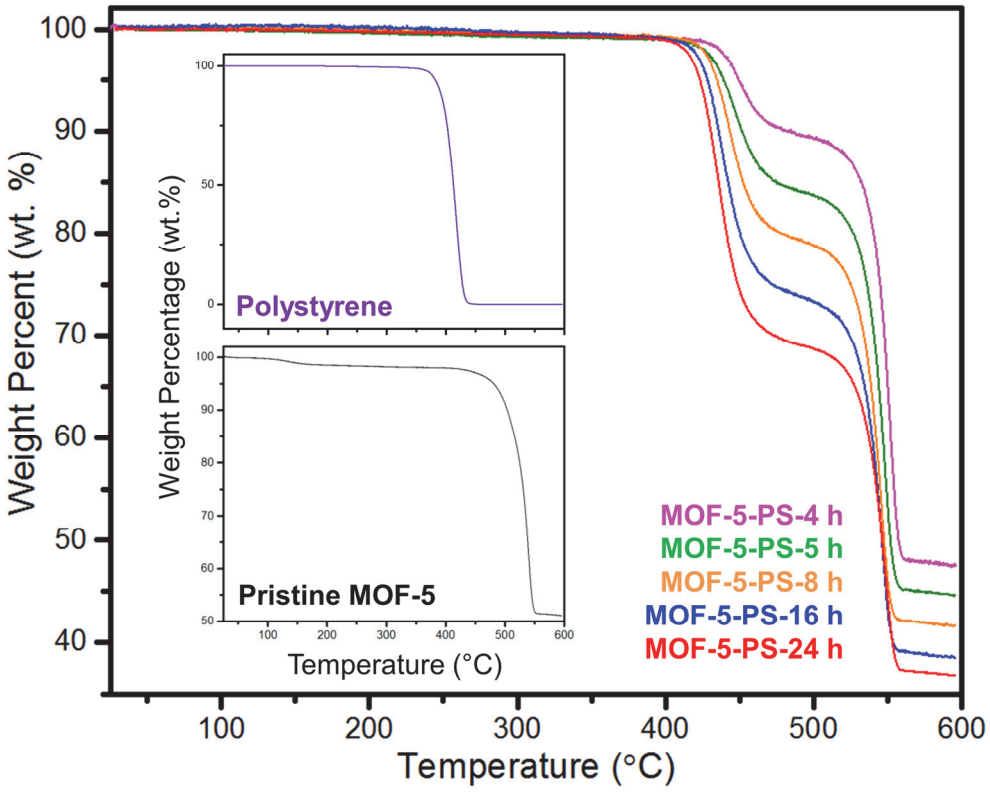

Figure 3.3. TGA curves of MOF-5-PS-4–24 h, polystyrene, and pristine MOF-5

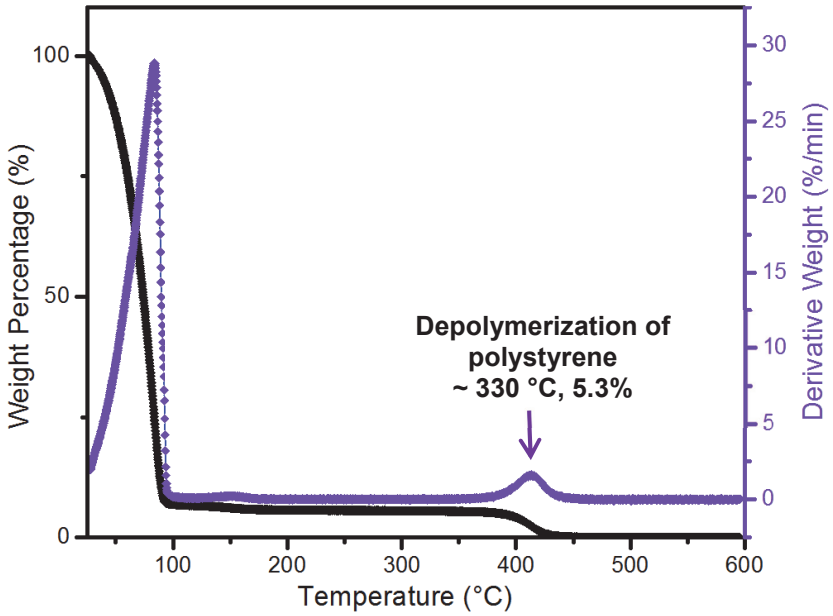

Figure 3.4. TGA weight loss (black) and differential weight loss (purple) curves of styrene after heating at 65 °C for 24 h

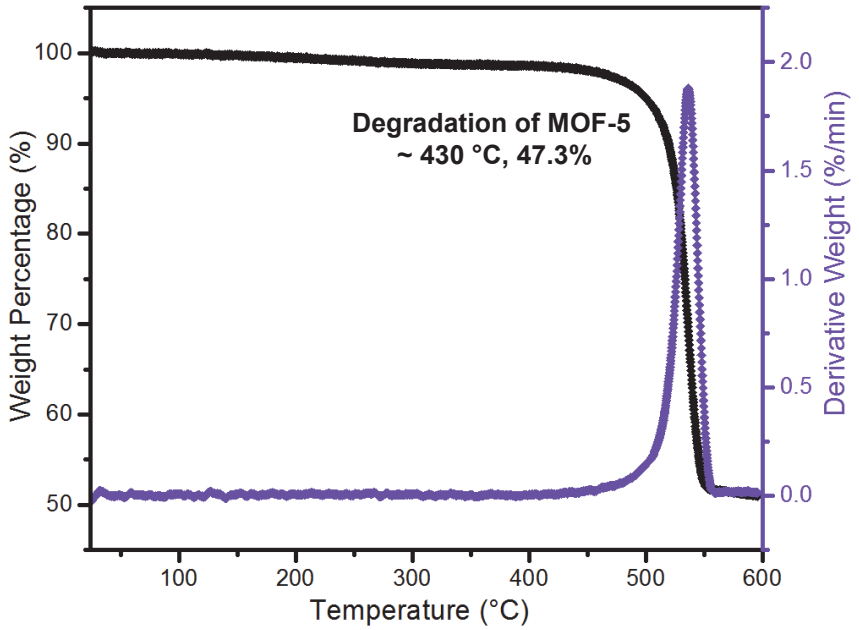

Figure 3.5. TGA weight loss (black) and differential weight loss (purple) curves of pristine MOF-5

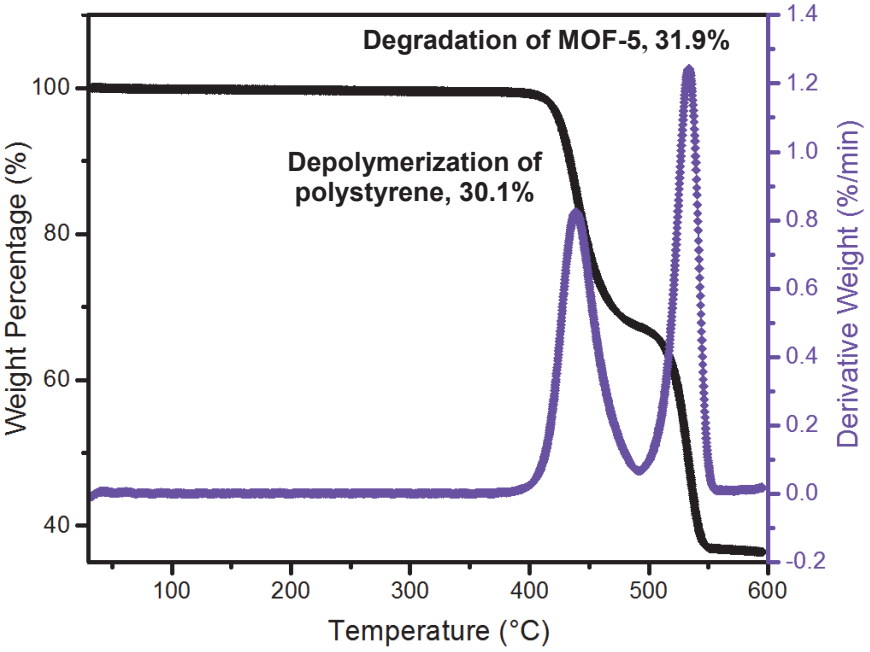

Figure 3.6. TGA weight loss (black) and differential weight loss (purple) curves of MOF-5-PS-24 h composite where depolymerization of polystyrene is well separated from decomposition of MOF-5

Table 3.1. Weight percentages of polystyrene and BET surface areas of MOF-5-PS-4–24 h

Polymerization Time (h)	TGA Weight Percentage of Polystyrene (%)	BET Surface Area (m^2/g)
0	–	3509
4	9.4	2780
5	15.1	2496
8	20.0	2163
16	25.3	1868
24	30.1	1611

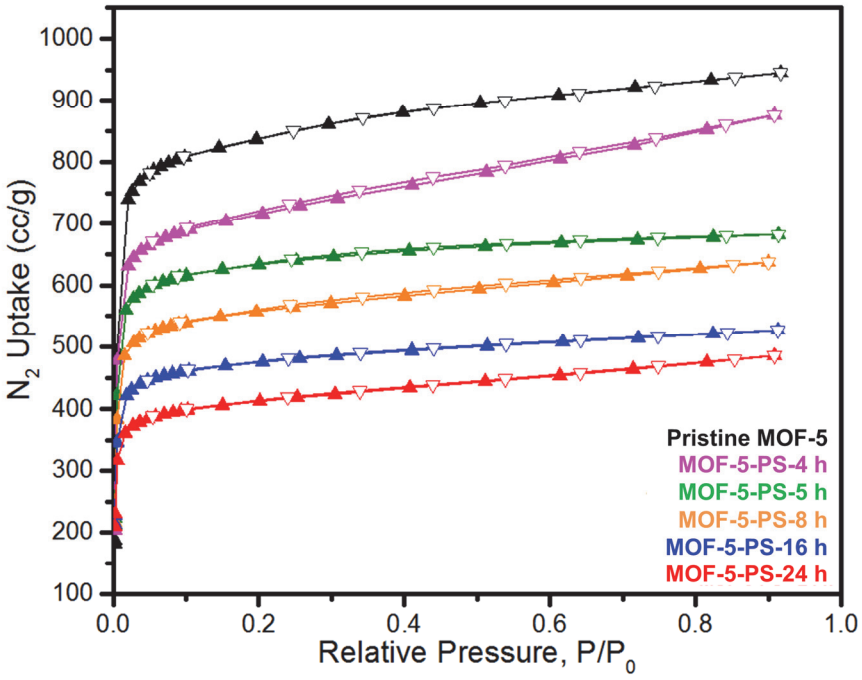

Figure 3.7. N_2 sorption isotherms of pristine MOF-5 and MOF-5-PS-4–24 h composites (Adsorption data are shown in full symbols while desorption data are shown in hollow symbols)

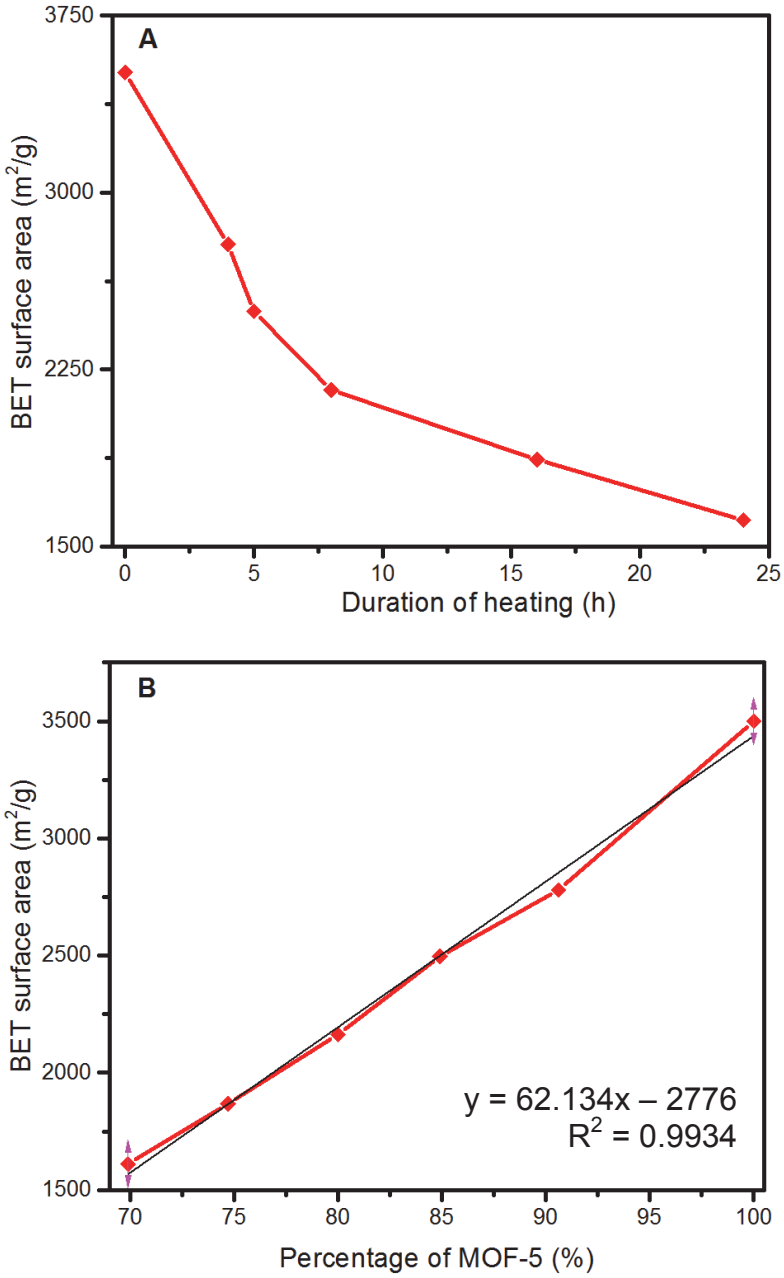

Figure 3.8. Correlation graphs: (A) BET surface area versus duration of heating and (B) BET surface area versus percentage of MOF-5 in the MOF-5-PS-4–24 h composites

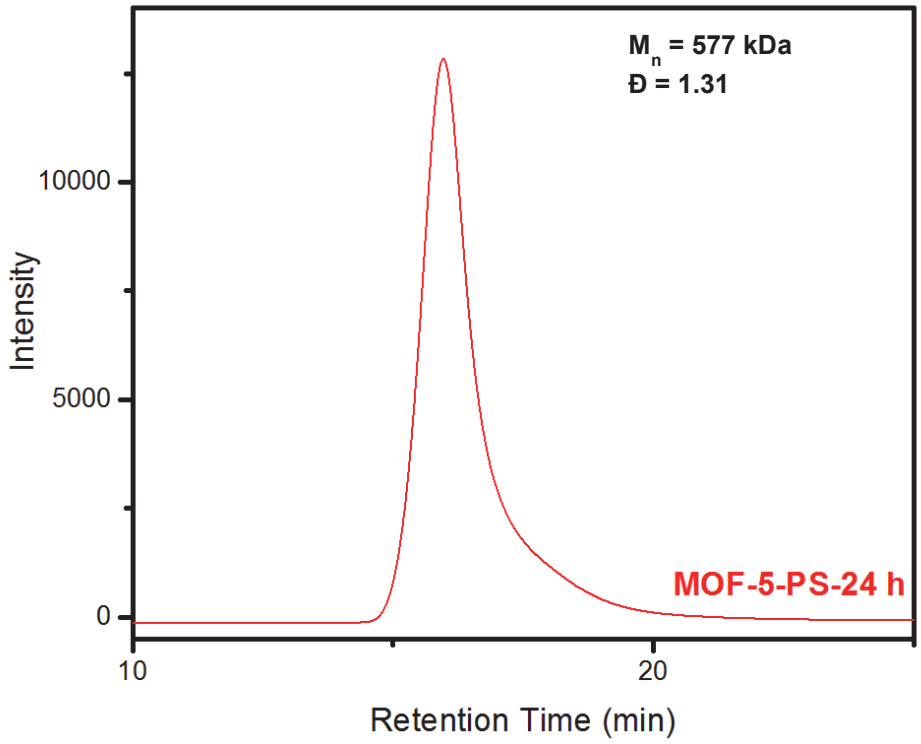

Figure 3.9. A representative GPC trace of high molecular weight polystyrene extracted from MOF-5-PS-24 h

Table 3.2. GPC data for polystyrene extracted after digestion of the MOF-5-PS-4–24 h composites

Composite	M_n	M_w	Đ
MOF-5-PS-4 h	481828	618424	1.28
MOF-5-PS-5 h	513819	689742	1.34
MOF-5-PS-8 h	541955	703823	1.30
MOF-5-PS-16 h	555162	715539	1.29
MOF-5-PS-24 h	576805	758366	1.31

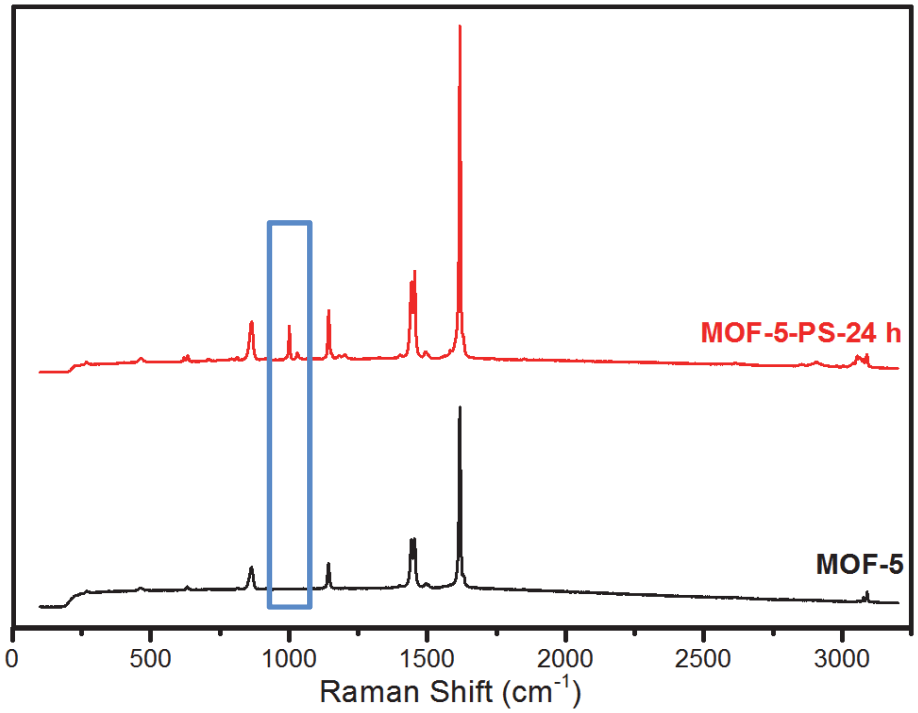

Figure 3.10. Raman spectra of pristine MOF-5 and MOF-5-PS-24 h with additional peaks of 1001 and 1030 cm^{-1} from polystyrene

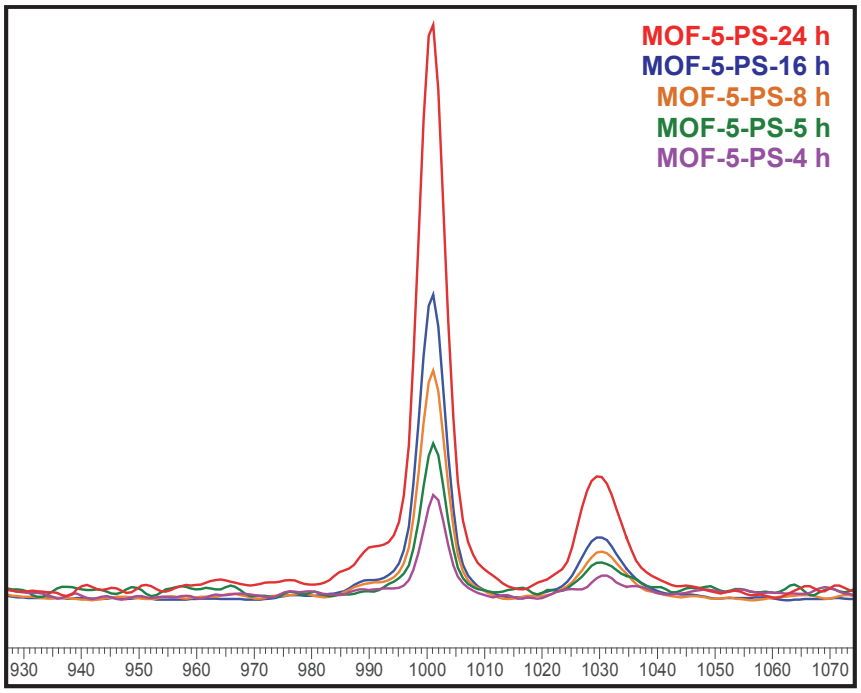

Figure 3.11. Raman peaks at 1001 and 1030 cm^{-1} from MOF-5-PS-4–24 h composites after normalization of the MOF-5 peak at 1617 cm^{-1}

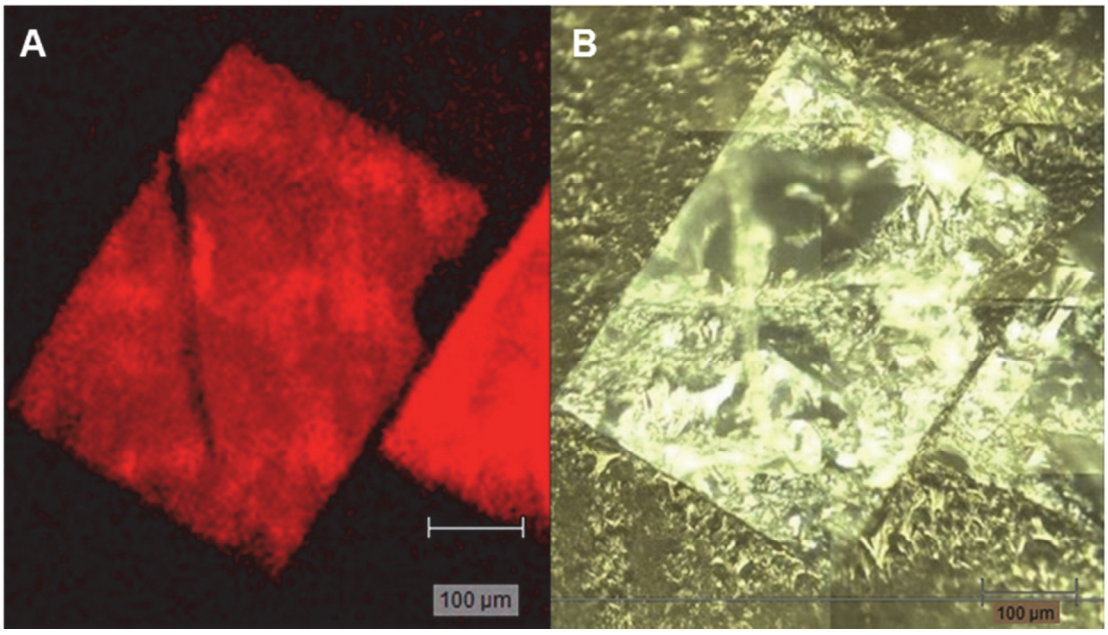

Figure 3.12. Raman mapping data of MOF-5-PS-24 h: (A) Raman map of area for the 1001 cm^{-1} peak shown in red of the cross-sectioned MOF-5-PS embedded in epoxy; (B) A white light image of the sectioned MOF-5-PS in embedded in epoxy showing two distinct crystals.

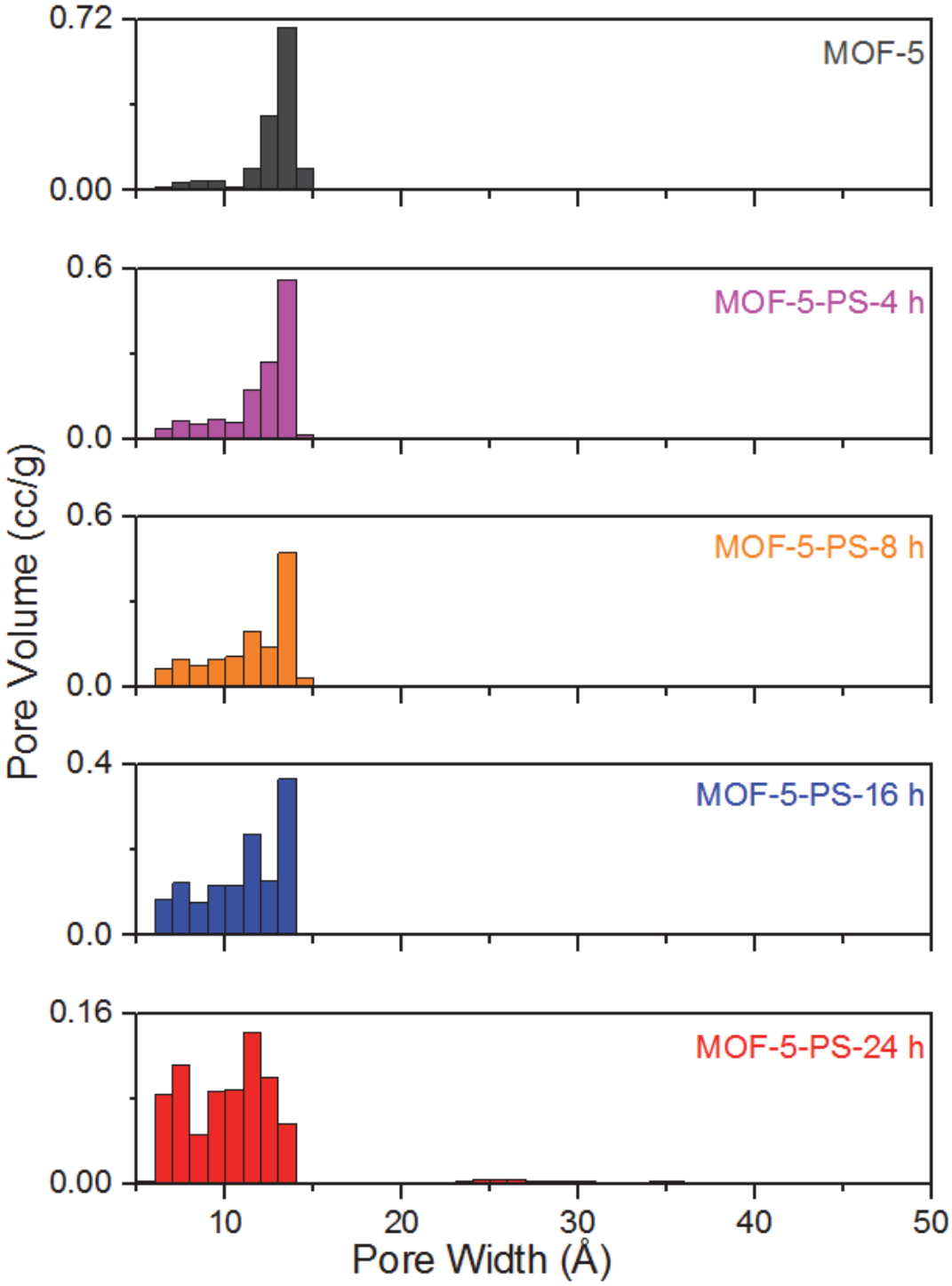

Figure 3.13. Pore volume histograms of pristine MOF-5 and MOF-5-PS-4, -8, -16, and -24 h composites

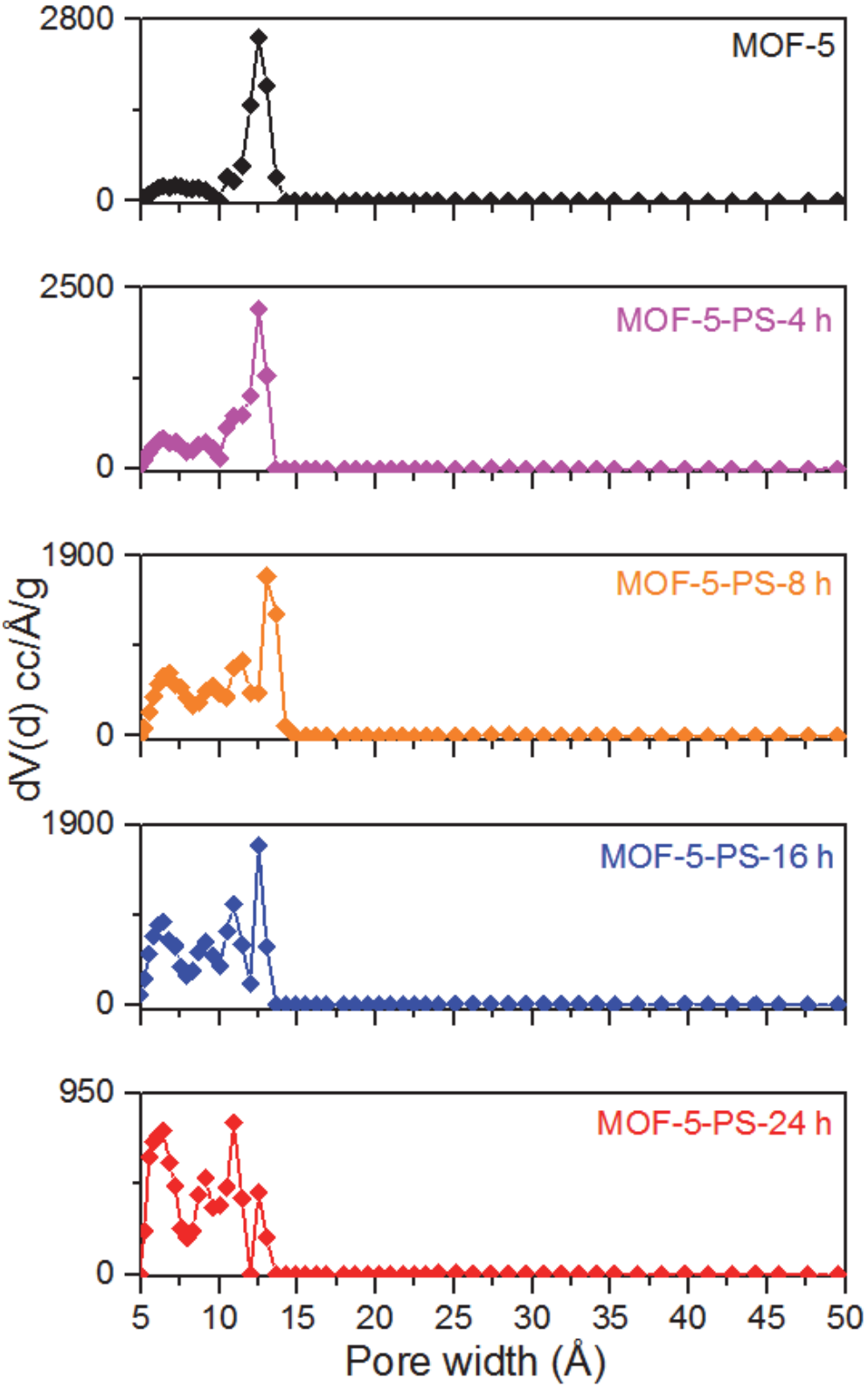

Figure 3.14. Differential pore volume distribution plots of MOF-5 and MOF-5-PS-4, -8, -16, and -24 h composites

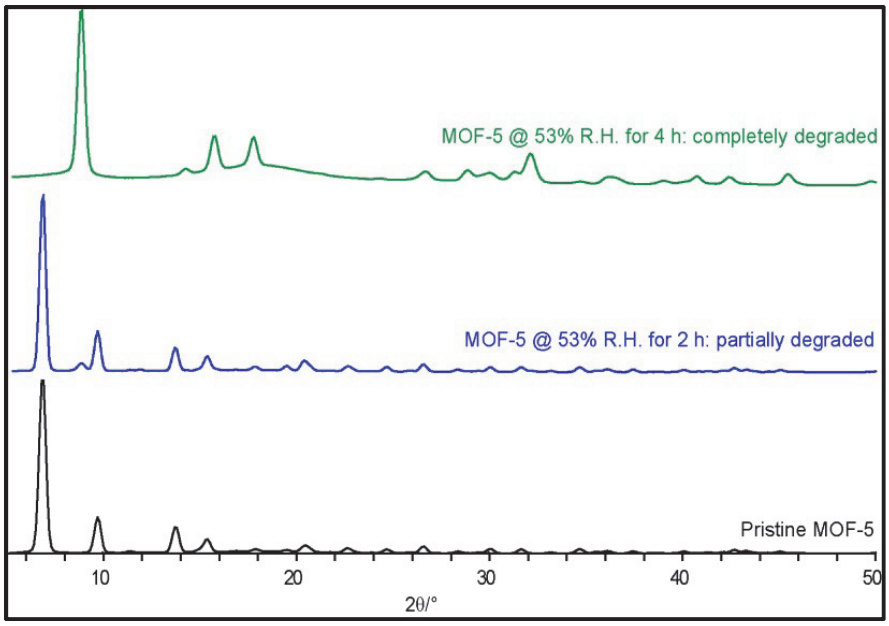

Figure 3.15. PXRD patterns of pristine MOF-5 and MOF-5 crystals after exposing to 53% RH

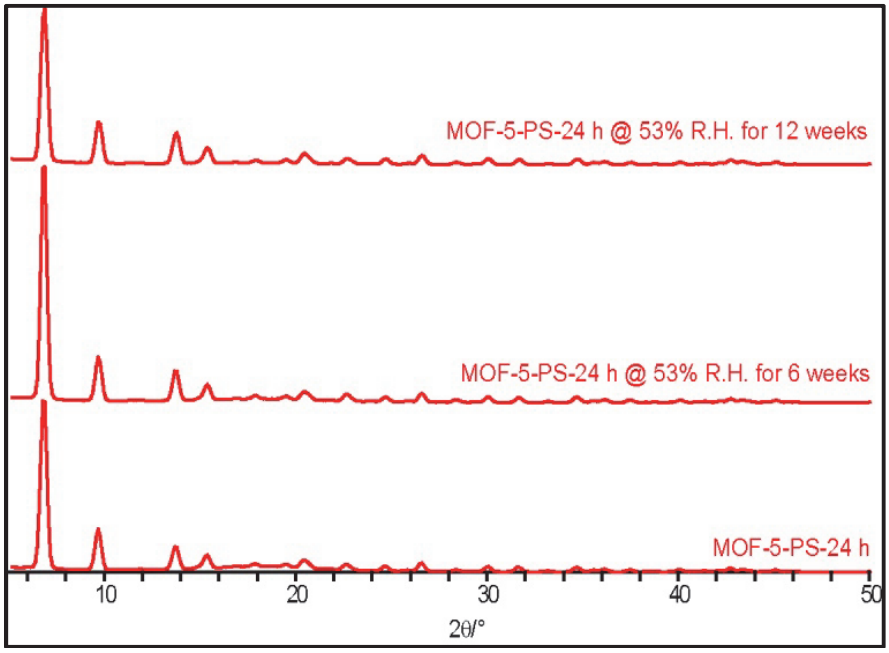

Figure 3.16. PXRD patterns of pristine MOF-5-PS-24 h and MOF-5-PS-24 h crystals after exposing to 53% RH

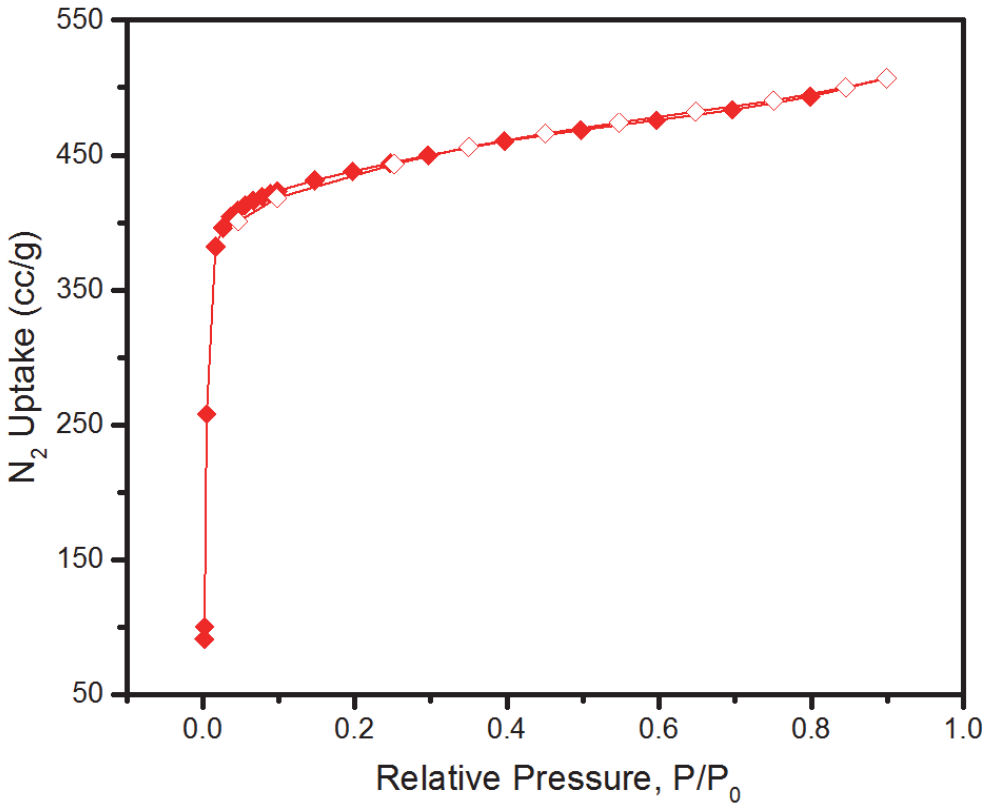

Figure 3.17. N_2 sorption isotherm of MOF-5-PS-24 h composite after exposure to 53% RH for 3 months. (BET surface area obtained: 1556 m^2/g)

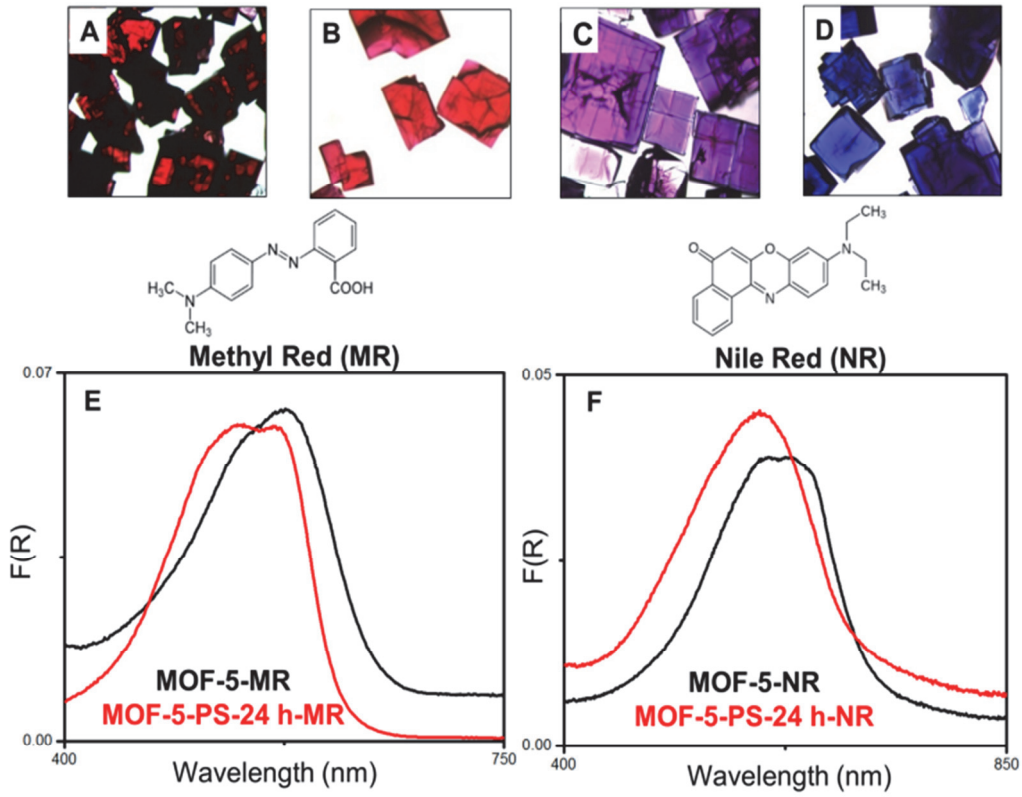

Figure 3.18. Microscopic images of methyl red and nile red adsorbed MOF-5-PS-24 h and MOF-5 crystals: (A) methyl red dye adsorbed MOF-5-PS-24 h; (B) methyl red dye adsorbed MOF-5; (C) nile red dye adsorbed MOF-5-PS-24 h; (D) nile red dye adsorbed MOF-5 and solid state UV-Visible spectra: (E) methyl red adsorbed MOF-5-PS-24 h and MOF-5; (F) nile red adsorbed MOF-5-PS-24 h and MOF-5.

Table 3.3. Peak maxima of the solid-state UV-visible spectra of methyl red and nile red dye adsorbed on pristine MOF-5 and MOF-5-PS-24 h composite

Dye	**Peak Maxima in MOF-5-PS-24 h (nm)**	**Peak Maxima in MOF-5 (nm)**
Methyl red	566.8	575.6
	538.2	
Nile red	600.0	607.5
		631.7

Table 3.4. CO_2 adsorption capacities of pristine MOF-5 and MOF-5-PS-24 h composite at 1 atm and 298 and 273 K

Sample	Temperature (K)	Uptake (cc/g)
MOF-5	298	16.6
	273	28.3
MOF-5-PS-24 h	298	18.8
	273	36.6

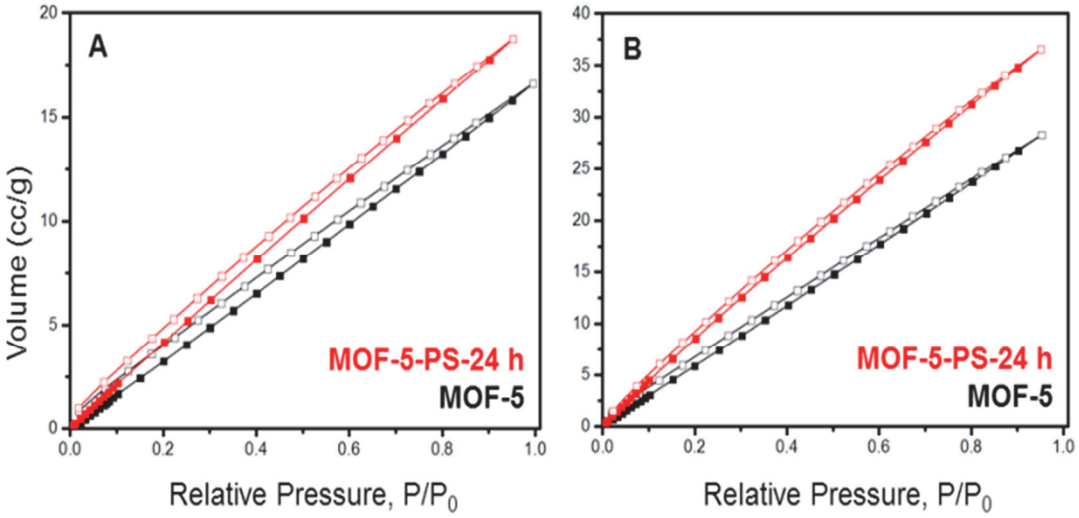

Figure 3.19. CO_2 adsorption isotherms of MOF-5-PS-24 h and pristine MOF-5 obtained at 1 atm: (A) 298 K and (B) 273 K (Adsorption data are shown in full symbols while desorption data are shown in hollow symbols.)

3.6 References

(1) Zhu, H.; Zhang, Q.; Zhu, S. *ACS Appl. Mater. Interfaces.* **2016**, *8*, 17395.

(2) Calvez, C. L.; Zouboulaki, M.; Petit, C.; Peeva, L.; Shirshova, N.; *RSC Adv.* **2016**, *6*, 17314.

(3) Su, P.; Li, W.; Zhang, C.; Meng, Q.; Shen, C.; Zhang, G. *J. Mater. Chem. A.* **2015**, *3*, 20345.

(4) Zhang, Y.; Feng, X.; Li, H.; Chen, Y.; Zhao, J.; Wang, S.; Wang, L.; Wang, B. *Angew Chem. Int. Ed.* **2015**, *54*, 4259; *Angew Chem.* **2015**, *127*, 4333.

(5) Liu, H.; Zhu, H.; Zhu, S. *Macromol. Mater. Eng.* **2015**, *300*, 191.

(6) Erucara, I.; Keskin, S. *J. Memb. Sci.* **2012**, *407-408*, 221.

(7) Bromberg, L.; Su, X.; Hatton, T. A. *Chem. Mater.* **2014**, *26*, 6257.

(8) Zhang, R.; Ji, S.; Wang, N.; Wang, L.; Zhang, G.; Li, J.-R. *Angew. Chem. Int. Ed.* **2014**, *53*, 9775; *Angew. Chem.* **2014**, *126*, 9933.

(9) Liang, X.; Zhang, F.; Feng, W.; Zou, X.; Zhao, C.; Na, H.; Liu, C.; Sun, F.; Zhu, G. *Chem. Sci.* **2013**, *4*, 983.

(10) Huo, J.; Marcello, M.; Garai, A.; Bradshaw, D. *Adv. Mater.* **2013**, *25*, 2717.

(11) Lee, H. J.; Cho, W.; Oh, M. *Chem. Commun.* **2012**, *48*, 221.

(12) Zhao, D.; Tan, S.; Yuan, D.; Lu, W.; Rezenom, Y. H.; Jiang, H.; Wang, L.-Q.; Zhou, H.-C. *Adv. Mater.* **2011**, *23*, 90.

(13) O'Neill, L. D.; Zhang, H.; Bradshaw, D. *J. Mater. Chem.* **2010**, *20*, 5720.

(14) Zhang, Z.; Nguyen, H. T. H.; Miller, S. A.; Cohen, S. M. *Angew. Chem. Int. Ed.* **2015**, *54*, 6152; *Angew. Chem.* **2015**, *127*, 6250.

(15) James, S. L. *Chem. Soc. Rev.* **2003**, *32*, 276.

(16) Eddaoudi, M.; Kim, J.; Rosi, N.; Vodak, D.; Wachter, J.; O'Keeffe, M.; Yaghi, O. M. *Science*, **2002**, *295*, 469.

(17) Park, T.-H.; Koh, K.; Wong-Foy, A. G.; Matzger, A. J. *Cryst. Growth Des.* **2011**, *11*, 2059.

(18) Dutta, A.; Wong-Foy, A. G.; Matzger, A. J. *Chem. Sci.* **2014**, *5*, 3729.

(19) Wade, W. R.; Corrales-Sanchez, T.; Narayan, T. C.; Dincă, M. *Energy Environ. Sci.* **2013**, *6*, 2172.

(20) Biradha, K.; Fujita, M. *Chem. Commun.* **2001**, 15.

(21) Dong, G.; Li, H.; Chen, V. *J. Mater. Chem. A*. **2013**, 4610.

(22) Goh, P.S.; Ismail, A. F.; Sanip, S. M.; Ng, B. C.; Aziz, M. *Sep. Purif. Technol.* **2011**, *81,* 243.

(23) Culp, J. T.; Sui, L.; Goodman, A.; Luebke, D. *J. Colloid Interface Sci.* **2013**, *393*, 278.

(24) Zhang, Z.; Nguyen, H. T. H.; Miller, S. A.; Ploskonka, A. M.; DeCoste, J. B.; Cohen, S. M. *J. Am. Chem. Soc.* **2016**, *138*, 920.

(25) Rodenas, T.; Luz, I.; Prieto, G.; Seoane, B.; Miro, H.; Corma, A.; Kapteijn, F.; Llabrés Xamena, F. X.; Gascon, J. *Nat. Mater.* **2015**, *14*, 48.

(26) Li, W.; Zhang, Y.; Li, Q.; Zhang, G. *Chem. Eng. Sci.* **2015***, 135*, 232.

(27) Seoane, B.; Coronas, J.; Gascon, I.; Benavides, M. E.; Karvan, O.; Caro, J.; Kapteijna, F.; Gascon, J. *Chem. Soc. Rev.* **2015**, *44*, 2421.

(28) Adams, R.; Carson, C.; Ward, J.; Tannenbaum, R.; Koros, K. *Microporous and Mesoporous Mater.* **2010**, *131*, 13.

(29) Erucar, I.; Yilmaz, G.; Keskin, S. *Chem. Asian J.* **2013**, *8*, 1692.

(30) Zhang, L.; Hu, Z.; Jiang, J. *J. Phys. Chem. C.* **2012**, *116*, 19268.

(31) Zornoza, B.; Tellez, C.; Coronas, J.; Gascon, J.; Kapteijn, F. *Microporous and Mesoporous Mater.* **2013**, *166*, 67.

(32) Shahida, S.; Nijmeijera, K.; Nehacheb, S.; Vankelecomc, I.; Deratanib, A.; Quemener, D. *J. Memb. Sci.* **2015**, *492*, 21.

(33) Gascon, J.; Kapteijn, F.; Zornoza, B.; Sebastia´n, V.; Casado, C.; Coronas, J. *Chem. Mater.* **2012**, *24*, 2829-2844.

(34) Vinh-Thang, H.; Kaliaguine, S. *Chem. Rev.* **2013**, *113*, 4980.

(35) Lin, R.; Ge, L.; Hou, L.; Strounina, E.; Rudolph, V.; Zhu, Z. *ACS Appl. Mater. Interfaces.* **2014**, *6*, 5609.

(36) Denny Jr., M. S.; Cohen, S. M. *Angew. Chem. Int. Ed.* **2015**, *54*, 9029; *Angew. Chem.* **2015**, *127*, 9157.

(37) Tien-Binh, N.; Vinh-Thang, H.; Chen, X. Y.; Rodriguea, D.; Kaliaguine, S. *J. Mater. Chem. A.* **2015**, *3*, 15202.

(38) Feijani, E. A.; Tavasoli, T.; Mahdavi, H.; *Ind. Eng. Chem. Res.* **2015**, *54*, 12124.

(39) McDonald, K. A.; Feldblyum, J. I.; Koh, K.; Wong-Foy, A. G.; Matzger, A. J. *Chem. Commun.* **2015**, *51*, 11994.

(40) Zhang, W.; Hu, Y.; Ge, J.; Jiang, H. L.; Yu, S. H. *J. Am. Chem. Soc.* **2014**, *136*, 16978.

(41) Brunauer, S.; Emmett, P. H.; Teller, E. *J. Am. Chem. Soc.* **1938**, *60*, 309.

(42) Siberio-Pérez, D. Y.; Wong-Foy, A. G.; Yaghi, O. M.; Matzger, A. J. *Chem. Mater.* **2007**, *19*, 3681.

(43) Ravikovitch, P. I; Haller, G. L; Neimark, A. V. *Adv. Colloid Interface Sci.* **1998**, *76-77*, 203.

(44) Ravikovitch, P. I.; Neimark, A. V. *J. Phys. Chem. B.* **2001**, *105*, 6817.

(45) Guo, P.; Dutta, D.; Wong-Foy, A. G.; Gidley, D. W.; Matzger, A. J. *J. Am. Chem. Soc.* **2015**, *137,* 2651.

(46) Seu, G. *Dyes and Pigments.* **1995***, 29,* 227.

(47) Deye, J. F.; Berger, T. A.; Anderson, A. G. *Anal. Chem.* **1990**, *62*, 615.

(48) Mayo, F. R. *J. Am. Chem. Soc.* **1953**, *75*, 6133.

(49) Mayo, F. R. *J. Am. Chem. Soc.* **1968**, *90*, 1289.

(50) Khuong, K. S.; Jones, W. H.; Pryor, W. A.; Houk, K. N. *J. Am. Chem. Soc.* **2005**, *127*, 1265.

(51) Sun, Y.; Wu, Y.; Chen, L.; Fu, Z.; Sh, Y. *Polym. J.* **2009**, *41*, 954.

(52) Hiatt, R. R.; Bartlett, P. D. *J. Am. Chem. Soc.* **1959**, *81*, 1149.

(53) Buzanowski, W. C.; Graham, J. D.; Priddy, D. B.; Shero, E. *Polymer*. **1992**, *33*, 3055.

(54) Pryor, W. A.; Lasswell, L. D. *AdV. Free-Radical Chem.* **1975**, *5*, 27.

CHAPTER IV

Thermal decomposition pathways of nitro-functionalized metal-organic frameworks[§]

4.1 Introduction

Recent advances in the synthesis of explosive coordination polymers (CPs), and in particular the subset known as metal-organic frameworks (MOFs), have highlighted the utility of coordination chemistry to produce energetic materials with a wide range of structure types and reactive characteristics.[1-3] This class of materials shows promise to address some of the drawbacks of traditional energetics by offering more control over molecular arrangement leading to changes in sensitivity to stimuli and, in some cases, improved thermal stability. The synthesis of energetic CPs almost exclusively involves nitrogen-rich heterocyclic linkers because these high-nitrogen molecules can be explosives themselves and have numerous coordination modes for CP formation. This can lead to a variety of different CPs derived from the same linker.[4] However, the effects of coordination polymerization on nitrated aromatics, the most common motif in energetic materials, are underexplored in the literature.[1-3] Here, we present that cubic crystals of energetic compounds assembled with copper ions and nitrated biphenyl linkers decompose in an anisotropic manner to give fibrous carbon structures with highly dispersed metals by an unprecedented reaction manifold.

4.2 Results and Discussion

Biphenyl-4,4′-dicarboxylic acid (H_2BPDC), one of the basic building blocks in the CP literature, was modified with pendant nitro groups resulting in a nitrated aromatic

---

[§] McDonald, K. A.; Ko, N.; Noh, K.; Bennion, J. C.; Kim, J.; Matzger, A. J. *Chem. Commun*. **2017**, *53*, 7808. Adapted by permission of The Royal Society of Chemistry.

suitable for coordination polymerization. A solvothermal reaction between 2,2′,6,6′-tetranitrobiphenyl-4,4′-dicarboxylic acid (H_2BPDC-$(NO_2)_4$) and $Cu(NO_3)_2 \cdot 2.5H_2O$ in *N*,*N*-dimethylacetamide (DMA) resulted in a nitrated energetic MOF, $[Cu(BPDC\text{-}(NO_2)_4)(H_2O)]_n$ (hereafter referred to as CuNbO-1) (Figure 4.1a). CuNbO-1, like the vast majority of currently used explosives, is underoxidized, as it does not contain enough oxygen within the material for conversion to completely oxidized decomposition products (for example, carbon to carbon dioxide).[5,6] When heated to 250 °C, CuNbO-1 deflagrates leading to long anisotropic carbon structures that are morphologically distinct from the highly symmetric starting MOF crystals.[7-10]

In the crystal structure of CuNbO-1, the two phenyl units in BPDC-$(NO_2)_4$ are oriented perpendicularly to each other. These biphenyl units are linked to Cu_2 paddlewheel clusters giving rise to a non-interpenetrated 3D network with NbO topology (Figure 4.1a and Table 4.1).[11,12] The thermal decomposition of CuNbO-1 was first examined using thermogravimetric analysis (TGA). The 68 wt % loss upon heating to 200 °C corresponds to the loss of *ca*. 14 DMA molecules per formula unit $[Cu(BPDC\text{-}(NO_2)_4)(H_2O)]$ (calculated 71.6 wt %). The ^{1}H-NMR spectrum for the as-synthesized crystals dissolved in DCl/DMSO-d_6 confirms the number of DMA molecules corresponding to the TGA measurement (Figure 4.2). Following desolvation, it was observed that essentially the total weight of the sample was lost after heating to 250 °C (Figure 4.1b). This phenomenon is not typical for most known MOFs which deposit non-volatile inorganic residues such as carbons and metal/metal oxides.[7-9] Analysis of the TGA chamber after heating revealed long fibrous decomposition products. The deflagration of CuNbO-1 caused the residues to lift out of the TGA pan (Figure 4.3). Both solvated and desolvated CuNbO-1 samples showed seemingly the same thermal decomposition pathways. The details of this decomposition form the content of this contribution, presenting a further understanding of the decomposition process of energetic CPs comprised of nitrated aromatics.

To further examine the decomposition of CuNbO-1, high-speed imaging of the thermal decomposition was carried out at 9,000 frames per second (Figure 4.4). An initiation point on one face of the MOF crystal leads to long anisotropic carbonaceous structures. This initiation point results in a break with the cubic symmetry of the material

and is consistent with an initiation event that propagates within the CuNbO-1 crystals leading to unfolding and large anisotropic expansion similar to Black Snake Fireworks (for the complete high-speed video go to: http://pubs.rsc.org/en/content/articlelanding/2017/cc/c7cc03354k#!divAbstract). This high-speed video clearly shows that each crystal is converted to long anisotropic decomposition products; a decomposition pathway, which has not been observed thus far in MOF literature. More specifically, a ~0.2 mm CuNbO-1 crystal yields interwoven carbonaceous fibers on a length scale of about ~1 cm.

The decomposition product of CuNbO-1 has an unusual morphology; therefore, an analysis of the decomposition product was conducted in order to understand more about its decomposition pathway. The Raman spectrum of the CuNbO-1 decomposition product showed peaks at 1579 cm^{-1} and 1352 cm^{-1}, representative of the G (E_{2g}) and D (A_{1g}) breathing modes in carbon materials, respectively (Figures 4.5a and 4.6).[13] In perfect graphite, the D breathing mode is forbidden and is only active in the presence of disorder.[14-16] Therefore, the Raman spectrum indicates that the CuNbO-1 decomposition product contains amorphous carbon. The amorphous structure of the carbon was further confirmed by transmission electron microscopy (TEM), which finds that no long-range order is present (Figure 4.7). Powder X-ray diffraction (PXRD) showed a broad peak centered at $2\theta = 18.0°$; this diffraction angle is between 26.5° for the (002) peak of pure graphite and ~10-12° for graphene oxides (Figures 4.5b and 4.9).[17-19] Therefore, the *d*-spacing of 4.9 Å for the amorphous carbon from CuNbO-1 is longer than that of graphite (3.4 Å) but significantly shorter than those of graphene oxides (*ca*. 7~8 Å). Using the Sherrer equation with 0.9 as a shape factor, the thickness of the carbon is approximated as 12 Å, corresponding to stacking of three carbon layers.[17-19] Notably absent are peaks in the PXRD pattern corresponding to diffraction from copper metal or copper oxides accompanying the amorphous carbon. Therefore, scanning electron microscopy with energy dispersive X-ray spectroscopy (SEM-EDX) was used to confirm the presence of copper in the decomposition product (Figures 4.5c and Figures 4.10-4.13). These data, in combination with the lack of diffraction peaks from the copper species present on the carbon, supports the conclusion that they are highly dispersed throughout the amorphous carbon matrix.

In this context it should be noted that graphite intercalation compounds (GICs) with metal donors, such as superconducting C_6Ca and C_6Yb, have ca. 4.5 Å as interplanar distances.[20] The decomposition product of CuNbO-1 is consistent with the formation of Cu-intercalated carbon sheets although the layers are not purely graphitic. Known metal-intercalated graphites limit alkali, alkaline earth, and some lanthanoid metal atoms (Yb, Eu) as donors with interplanar spacing ranging from 3.90 Å (Li) to 5.62 Å (Rb).[21-23]

The decomposition of CuNbO-1 initiated under a nitrogen atmosphere occurs in the same general manner as the decomposition in air (Figures 4.14 and 4.15) indicating no role for moisture/oxygen in the mechanism. However, when sealed under vacuum (~0.033 Torr) the decomposition differed in that the CuNbO-1 crystals fragmented into smaller carbon residues, which were subsequently shown to be amorphous with substantially similar Raman bands and an increased I_D/I_G ratio (Figure 4.5a and Figures 4.16-4.22). It is believed that the decomposition pathway under vacuum is different from under nitrogen and air because trapped gasses, generated during decomposition, act as a blowing agent and when they are subjected to vacuum their rapid release causes structural instability leading to collapse; however, the layer stacking mode is maintained like the decomposition products obtained in air or N_2 atmosphere (Figure 4.5b).

To further probe the mechanism of thermal decomposition, an analysis of the decomposition pressure and gaseous decomposition products was conducted. The pressure change as a result of the thermal decomposition of either CuNbO-1 crystals or the $H_2BPDC\text{-}(NO_2)_4$ ligand itself in a sealed apparatus filled with helium, was monitored with a pressure transducer and normalized to psi/mmol. The pressure released by the ligand is approximately 7 % greater than from CuNbO-1 on a molar basis, indicating that the decomposition pathways differ between the two materials. Analysis of the decomposition gasses generated from each sample was achieved by coupling the apparatus with high-resolution EI mass spectrometry (Figures 4.23-4.26). Decomposition product gasses including N_2, CO, CO_2, NO, and NO_2 were detected in each case; however, the distribution of some of these gasses differed significantly and analysis of these differences provided insight into the relative decomposition pathways between CuNbO-1 and the $H_2BPDC\text{-}(NO_2)_4$ ligand. Notable differences were present in the relative abundance of NO and CO_2 (Figure 4.27). High amounts of NO suggest

incomplete decomposition of the ligand and thus a reduction in the amount of CO_2. In contrast, CuNbO-1 contains 6.9 % more CO_2 compared to the linker, while also producing a significant amount of amorphous carbon. It is proposed that the copper in CuNbO-1 catalyzes the oxidation of CO to CO_2, which not only reduces the overall amount of gas produced (as evidenced by gas analysis), but therefore also increases the amount of carbon left in the decomposition product. More specifically, these catalytic effects lead to more of the limited oxygen atoms in CuNbO-1 being used to convert CO to CO_2 and, therefore, less oxygen available to oxidize the remaining carbon to CO. This results in more carbon being left in the CuNbO-1 decomposition product, relative to the pure linker. Furthermore, the metal-mediated catalysis also leads to the anisotropic growth of the decomposition products.[23,24]

In order to understand the importance of intimate mixing in the formation of the anisotropic decomposition products, physical mixtures of copper acetate ($Cu_2(CH_3COO)_4 \cdot (H_2O)_2$) and the $H_2BPDC\text{-}(NO_2)_4$ ligand were prepared and thermal decomposition was monitored (Figures 4.28-4.30). Copper acetate was chosen to mimic the Cu_2 paddlewheels in CuNbO-1. Copper (II) nitrate ($Cu(NO_3)_2$) was not employed to avoid a possible interference from the nitrate anion. The metal complex melts and eventually evolves gas at 240 °C, and the free ligand decomposes between 250~370 °C based on TGA measurements. When the two components are physically mixed and thermally initiated, the decomposition occurs heterogeneously and a mixture of decomposition modes results. The heterogeneity of the decomposition products stems from the metal source reacting with the ligand as well as the melting/decomposition of the metal and ligand alone. These complex decomposition processes are in stark contrast to the simple decomposition event of Cu-NbO-1, which results in one anisotropic fibrous decomposition product per crystal with a defined decomposition temperature. Since Cu^{2+} and $BPDC\text{-}(NO_2)_4$ are intimately mixed in CuNbO-1 and do not melt before framework destruction, they can react more efficiently during the thermal decomposition to form the characteristic carbon composites. Furthermore, the intimate mixing of these components in CuNbO-1 leads to a morphologically distinct carbon support that originates from a thermal initiation point, which propagates through the crystal leading to the formation of fibrous metal-carbon composites.

To demonstrate the extension of this type of decomposition to other MOFs containing similar nitrated aromatic linkers, a recently reported MOF, $[Cu(dnpdc)(H_2O)]_n(DMA)_4(H_2O)_2$ was selected and synthesized by a modified procedure: dnpdc = 2,2′-dinitrobiphenyl-4,4′-dicarboxylate or BPDC-$(NO_2)_2$.[25] Similar to CuNbO-1, this MOF (hereafter, CuNbO-2) is composed of Cu_2 paddlewheels as vertices and exhibits NbO-topology but doubly-interpenetrated;[1,17-19] CuNbO-2 has been formulated as $[Cu(BPDC\text{-}(NO_2)_4)(DMA)]_n$ with DMA as an axial ligand based on a single-crystal X-ray diffraction analysis (Table 4.2). We were able to show that the thermal decomposition pathway of CuNbO-2 is similar to that of CuNbO-1 in spite of differences in the sort of the axial ligand, degree of interpenetration, and extent of linker nitration. Moreover, an analysis of the decomposition product revealed that the morphology and structure of the resulting carbon are the same (Figure 4.32-4.37) suggesting possible generality for the decomposition paths observed here. However, other MOFs composed of hydroxo-bridged multi-nuclear copper clusters and BPDC-$(NO_2)_2$ do not seem to show the sort of decomposition described herein based on their reported TGA curves.[25,26] Moreover, a Gd-MOF formulated as $\{[Gd(BPDC\text{-}(NO_2)_4)_{1.5}(DMF)_2(H_2O)_2](S)(H_2O)\}_n$ (S = ethyl 3-oxobutanoate) does not show abrupt thermal decompostion.[27] Therefore, these observations imply that the unique decomposition pathways as found in CuNbO-1 and $[Cu(dnpdc)(H_2O)]_n(DMA)_4(H_2O)_2$ can be achieved only when particular metal clusters and nitrated aromatic linkers are properly combined.

4.3 Conclusions

In conclusion, the decomposition pathway of CPs containing nitrated aromatic energetic linkers differs from those containing nitrogen-rich heterocycles in that deflagration leads to anisotropic decomposition forming metal-carbon composites. The decomposition under air, vacuum, or nitrogen highlights the effect of trapped gasses inside the pores of the MOFs (CuNbO-1 and -2), which act as blowing agents during decomposition. This behavior differs dramatically from the energetic linker alone. Thus, it is necessary to achieve mixing at the molecular level between the linkers and copper ions through MOF formation, which induces metal-catalyzed decomposition in the

carbonization process. The extremely high level of metal dispersion in a similar way as in GICs suggests future applications of this synthetic approach in producing catalysts and conducting or energy storage materials where metal-carbon composites are vital to function.

4.4 Experimental Methods

2,2′-Dinitrobiphenyl-4,4′-dicarboxylic acid ($H_2(NO_2)_2$BPDC). 4-Iodobenzoic acid (25 g, 0.10 mol) was put into a mixture of fuming H_2SO_4 (100 mL) and fuming HNO_3 (75 mL), and this reaction mixture was stirred at 90 °C for 24 h. The resulting solution was cooled to room temperature and poured over ice (~ 1500 mL). A produced precipitate was filtered, washed with water, and dried under vacuum to give a yellow solid of *4-iodo-3-nitrobenzoic acid* (**1**; 27 g, 91.4%): ^{1}H-NMR (DMSO-d_6, 400 MHz) δ 13.73 (s, 1H), 8.33 (s, 1H), 8.25 (d, 1H, J = 8.0 Hz), 7.54 (d, 1H, J = 8.0 Hz); ^{13}C NMR (DMSO-d_6, 100 MHz) δ 165.7, 153.8, 142.5, 133.9, 132.6, 125.6, 94.6; FT-IR (KBr, 4000-400 cm^{-1}) 3422 (br), 3091 (m), 2851 (br), 2656 (w), 2579 (w), 1701 (vs), 1598 (s), 1557 (m), 1535 (vs), 1473 (w), 1422 (m), 1350 (m), 1313 (m), 1253 (m), 1162 (w), 1125 (w), 1023 (m), 907 (w), 845 (w), 807 (w), 769 (w), 742 (w), 713 (w), 656 (w), 601 (w), 538 (w). A mixture of **1** (27 g, 92 mmol) and H_2SO_4 (30 mL) in methanol (400 mL) was refluxed for 12 h. Aqueous NaOH solution (3 M, 200 mL) was gradually poured into the solution to give a light yellow precipitate of *methyl-4-iodo-3-nitrobenzoate* (**2**; 26 g, 91.6 %). The solid was filtered, washed with water and dried under vacuum: ^{1}H-NMR (DMSO-d_6, 400 MHz) δ 8.36 (s, 1H), 8.28 (d, 1H, J = 8.0 Hz), 7.87 (d, 1H, J = 8.0 Hz), 3.90 (s, 3H); ^{13}C NMR (DMSO-d_6, 100 MHz) δ 164.8, 153.9, 142.6, 133.7, 131.2, 125.5, 95.3, 53.3; FT-IR (KBr, 4000-400 cm^{-1}) 3420 (br), 3088 (w), 2955 (w), 1717 (vs), 1596 (m), 1561 (w), 1533 (s), 1439 (m), 1355 (m), 1286 (s), 1247 (s), 1198 (w), 1152 (w), 1124 (m), 1106 (w), 1022 (m), 975 (w), 911 (w), 884 (w), 842 (w), 821 (m), 766 (m), 741 (m), 724 (m), 687 (w), 655 (w), 593 (w), 549 (w), 497 (w), 464 (w). A mixture of methyl-4-iodo-3-nitrobenzoate (26 g, 85 mmol) and copper powder (21.5 g, 4 eq) in DMF (250 mL) was refluxed for 20 h under argon atmosphere. The mixture was filtered through Celite, and washed with fresh DMF (30 mL × 2). The filtered DMF solution was quenched with 5% $Na_2S_2O_3 \cdot 5H_2O$ aqueous solution (1000 mL) and extracted with ethyl acetate (100 mL ×

9). After treatment with brine (200 mL × 3), the organic phase was dried over $MgSO_4$, and filtered. After removing ethyl acetate under reduced pressure, dimethyl-2,2′-dinitrobiphenyl-4,4′-dicarboxylate (**3**) was obtained (14.3 g, 93.5%): ^{1}H-NMR (DMSO-d_6, 400 MHz) δ 8.70 (s, 2H), 8.38 (d, 2H, J = 8.0 Hz), 7.71 (d, 2H, J = 8.0 Hz), 3.96 (s, 6H); ^{13}C NMR (DMSO-d_6, 100 MHz) δ 164.7, 147.1, 137.4, 134.6, 132.5, 131.6, 125.5, 53.5; FT-IR (KBr, 4000-400 cm^{-1}) 3432(w), 3092(w), 2956(w), 2852(w), 1726(vs), 1618(m), 1561(w), 1528(vs), 1483(m), 1438(m), 1345(s), 1310(s), 1287(s), 1256(s), 1197(w), 1158(w), 1118, 1007(w), 967(w), 935(w), 917(w), 906(w), 862(w), 823(w), 769(m), 756(m), 725(w), 696(w), 676(w), 604(w), 560(w), 484(w), 415(w). Into a mixture of aqueous $LiOH{\cdot}H_2O$ (0.6 M, 100 mL), THF (100 mL), and MeOH (50 mL), **3** (5.0 g, 14 mmol) was added, and stirred at room temperature for 20 h. The solution was concentrated and acidified with 3M HCl to form a precipitate. The precipitate was filtered, washed with water, and dried under vacuum to afford *2,2′-dinitrobiphenyl-4,4′-dicarboxylic acid* (**4**; 4.5 g, 98 %): ^{1}H-NMR (DMSO-d_6, 400 MHz) δ 13.85 (br, 2H), 8.67 (s, 2H), 8.35 (d, 2H, J = 7.6 Hz), 7.68 (d, 2H, J = 7.6 Hz); ^{13}C NMR (DMSO-d_6, 100 MHz) δ 165.7, 147.1, 137.2, 134.7, 132.9, 132.3, 125.6; FT-IR (KBr, 4000-400 cm^{-1}) 3091(w), 2853(w), 2664(w), 2557(w), 1699(vs), 1618(m), 1561(w), 1532(s), 1483(m), 1422(m), 1345(s), 1314(m), 1289(m), 1254(m), 1160(w), 1130(w), 1093(w), 1007(w), 930(w), 863(w), 815(w), 764(w), 711(w), 695(w), 678(w), 653(w), 542(w).

2,2′,6,6′-Tetranitrobiphenyl-4,4′-dicarboxylic acid ($H_2(NO_2)_4$BPDC). A mixture of biphenyl-4,4′-dicarboxylic acid (8.0 g, 33 mmol), fuming H_2SO_4(500 mL), and fuming HNO_3 (400 mL) was stirred at 90 °C for 48 h. The solution was cooled to room temperature and poured over ice (~ 4000 mL) to give a precipitate which in turn was collected, washed with water, and dried under vacuum to give an ivory solid. ^{1}H-NMR spectra indicated that the solid was a mixture of various nitrated H_2BPDCs (**5**). This solid mixture was added to methanol (400 mL) containing H_2SO_4 (30 mL), which was refluxed for 12 h. In to the solution, which was cooled to room temperature, aqueous NaOH solution (3M, 200 mL) was gradually added to form light yellow crystalline precipitates of *dimethyl-2,2′,6,6′-tetranitrobiphenyl-4,4′-dicarboxylate* (**6**). The product was collected, washed with water, and dried under vacuum (6.2 g, 41.7 %): ^{1}H-NMR (DMSO-d_6, 400

MHz) δ 8.99 (s, 4H), 4.02 (s, 6H); ^{13}C NMR (DMSO-d_6, 100 MHz) δ 163.0, 148.7, 133.7, 130.2, 125.7, 54.1; FT-IR (KBr, 4000-400 cm^{-1}) 3442(w), 3117(w), 3097(w), 2956(w), 1729(vs), 1627(m), 1538(vs), 1458(m), 1436(w), 1344(s), 1301(s), 1282(s), 1203(w), 1163(m), 988(w), 922(m), 896(w), 769(w), 751(m), 726(m), 517(w), 500(w), 410(w). A solution of **6** (4.2 g, 9.3 mmol) in a mixture of aqueous LiOH·H_2O (0.6 M, 100 mL), THF (100 mL), and MeOH (50 mL) was stirred at room temperature for 20 h. The resulting solution was concentrated and acidified with conc. HCl. The precipitate was filtered, washed with H_2O, and dried under vacuum to give 2,2′,6,6′-tetranitrobiphenyl-4,4′-dicarboxylic acid (**7**) as yellow solids (3.1 g, 78.7 %): ^{1}H-NMR (DMSO-d_6, 400 MHz) δ 14.61(br, 2H), 8.96 (s, 4H); ^{13}C NMR (DMSO-d_6, 100 MHz) δ 163.9, 148.8, 135.1, 130.3, 125.4; FT-IR (KBr, 4000-400 cm^{-1}) 3085(w), 2920(w), 2862(w), 2664(w), 2538(w), 1713(vs), 1627(m), 1548(vs), 1467(m), 1409(m), 1342(vs), 1299(m), 1280(m), 1173(m), 1115(w), 1064(w), 921(m), 754(w), 730(m), 698(w), 555(w), 427(w).

Cu-NbO-1. $H_2(NO_2)_4$BPDC (103.2 mg, 0.24 mmol) and $Cu(NO_3)_2·2.5H_2O$ (114 mg, 0.49 mmol) were dissolved in DMA (18 mL) in a 20 mL vial. The vial was capped and heated in an isothermal oven at 85 °C for 24 h to give green crystals. The collected crystals were washed with DMA and dried in air. FT-IR (KBr, 4,000-400 cm^{-1}): 3405 (br, s), 1626 (vs), 1571 (s), 1418 (s), 1366 (vs), 1108 (w), 819 (w), 780 (m), 720 (m), 693 (m). Due to the easy vaporization of the occluded solvent molecules, instead of CHN analysis, the empirical formula was determined based on the ^{1}H-NMR spectrum of the as-synthesized sample: $[Cu(H_2O)BPDC\text{-}(NO_2)_4](DMA)_{14.5}$.

$[Cu(dnpdc)(H_2O)]_n(DMA)_4(H_2O)_2$. $[Cu(dnpdc)(H_2O)]_n(DMA)_4(H_2O)_2$ was prepared by a method slightly modified from the literature procedure.[28] A mixture of $H_2BPDC\text{-}(NO_2)_2$ (81 mg, 0.24 mmol) and $Cu(NO_3)_2·2.5H_2O$ (114 mg, 0.49 mmol) was dissolved in DMA (18 mL) in 20 mL vial. The vial was capped and heated in an isothermal oven at 95 °C for 24 h to give green crystals. The collected crystals were washed with DMA and dried in air. FT-IR (KBr, 4,000-400 cm^{-1}): 3405 (br, s), 1626 (vs), 1571 (s), 1418 (s), 1366 (vs), 1108 (w), 819 (w), 780 (m), 720 (m), 693 (m). Due to the easy vaporization of the occluded solvent molecules, instead of CHN analysis, the empirical formula was

determined based on the ^{1}H-NMR spectrum of the as-synthesized sample: [Cu(DMA)BPDC-$(NO_2)_2$]$(DMA)_{4.9}$.

Single Crystal X-Ray Diffraction

The X-ray data set for a selected CuNbO-1 crystal, which was sealed in a glass capillary, was collected on an ADSC Quantum-210 detector at 2D SMC with a silicon (111) double-crystal monochromator (DCM) at the Pohang Accelerator Laboratory in the Republic of Korea. The wavelength of X-ray was fixed at λ = 0.900 Å. The structure model obtained by direct methods using SHELXS-97 was refined by subsequent refinement processes using SHELXL-2014/7.[29] The crystal belongs to a cubic space group, *Im*(-3)*m* (No. 229) having 96 general positions (*Z* = 96). Since the asymmetric unit was composed of [Cu(H_2O) $(NO_2)_4$BPDC]/8, the Z value was changed to 12 (*Z*′ = 12) to make [Cu(H_2O)BPDC$(NO_2)_4$] for a formula during refinement processes. The H atom of a coordinated water molecule (O1) was included at ideal geometry using DFIX commands in SHELXL: a bond length of 0.85 Å with a site-occupancy factor fixed at 0.25. Due to the high symmetry of the structure and diffuse electron densities in the large pore of CuNbO-1, the occluded solvent molecules could not be identified; at this stage, R1 converged to 0.1266 for 1666 Fo > 4sig(Fo). With a new data set produced by SQUEEZE in PLATON,[30] R1 was reduced to 0.0777. All non-H atoms were refined anisotropically. The CIF file was deposited to the CCDC: **CCDC- 1541609**.

In order to confirm the reproduced synthesis of Cu(dnpdc)$(H_2O)]_n(DMA)_4(H_2O)_2$,[S1] a single-crystal X-ray diffraction analysis of the crystal was conducted as follows.

The X-ray data set for CuNbO-2 was collected on an ADSC Quantum-210 detector at 2D SMC with a silicon (111) double-crystal monochromator (DCM) at the Pohang Accelerator Laboratory in the Republic of Korea. The wavelength of X-ray was fixed at λ = 0.800 Å. The structure model obtained by direct methods using SHELXS-97 was refined by subsequent refinement processes using SHELXL-2014/7. The crystal belongs to a trigonal space group, *R*(-3) (No. 148, *Z* = 18). The asymmetric unit was defined as a formula of [Cu(DMA)BPDC-$(NO_2)_2$]·DMA. The NO_2 groups were disordered over two sites with site-occupancy factors of 0.5, respectively. Accrodingly, the site-occupancy factors of the H atoms bound to the C atoms to which the NO_2 groups are also bonded in the structural model were respectively fixed to 0.5. Two independent free DMA

molecules were also disordered with a half s.o.f., respectively. In contrast, the DMA coordinated to Cu1 was disordered over four sites with equal occupancies; however, the O10 atom was ordered with a full occupancy. At this stage, the diffuse electron densities in the pores of CuNbO-2 could not be allocated to guest molecules; R1 converged to 0.1147 for 6714 Fo > 4sig(Fo). With a new data set produced by SQUEEZE in PLATON, R1 was finally reduced to 0.0998. All non-H atoms were refined anisotropically. The structure can be solved with a trigonal space group, *R*(-3)*m* (No. 166) having 36 general positions (*Z* = 36); however, due to its higher symmetry, it was difficult to model the disordered DMA molecules. The CIF file was deposited to the CCDC: **CCDC-1541610**. CuNbO-2 has a same framework structure as that of $Cu(dnpdc)(H_2O)]_n(DMA)_4(H_2O)_2$. However, in CuNbO-2, two free DMAs and one coordinated DMA to a Cu ion have been identified whereas this structural feature is not shown in the crystal structure (CCDC-1404465) of $Cu(dnpdc)(H_2O)]_n(DMA)_4(H_2O)_2$.

Decomposition Gas Analysis (DGA)

To analyze the gases generated during the decomposition of CuNbO-1 and the free ligand, a sealed pressure apparatus was built with a PSIA pressure transducer and capable of connecting to a high-vacuum line. Samples of approximately 4 mg were placed in a glass tube and attached to the pressure apparatus. The vessel containing the sample was attached and pumped/purged two times with nitrogen and one additional pump/purge with helium. The pressure was monitored and the sample was decomposed using a propane torch. Once the system stabilized back to room temperature, the apparatus was connected to a high-resolution EI-MS to determine the composition of the gases. The oxygen present in the mass spectrum was used to correct for the amount of air leaking into the apparatus/mass spectrometer inlet and used to normalize the nitrogen generated from the decomposition versus the amount of nitrogen leaked in. On average it was found that approximately 50 % of the total amount of nitrogen detected by the mass spectrometer came from the leak. The NIST efficiency factors values for each gaseous species was used to account for ionization efficiency of each species. Two trials were averaged and a standard deviation of the percent of each gas was calculated. An example calculation is shown below for CuNbO-1 Trial 1:

From the raw mass spec data:

Values taken from the mass spectra of CuNbO-1 Trial 1.

Name	CO	CO_2	N_2	O2	NO
CuNbO-1 Trial 1	687.8	1319	380.9	52.42	278.1

1. Correcting the amount of air leaking into the apparatus/mass spectrometer inlet:

N_2 (leak) = $O_2 \times (0.7809/0.2095) = 52.42 \times (0.7809/0.2095) = 195.4$

N_2 ($decomp_{corrected}$) = 185.5

Values for gasses of interest taken from the mass spectra of CuNbO-1 Trial 1 with N_2 corrected for air leak.

Name	CO	CO_2	N_2 (corrected)	NO
CuNbO-1	687.8	1319	185.5	278.1

2. Total gas composition for the gasses in the table above = 3033

3. Correcting for ionization efficiency of each species (from NIST):

NIST efficiency factor values for each gas.

Gas	NIST efficiency factor
CO	1.003
CO_2	1.4
N_2	1
NO	1.12

Multiply the NIST efficiency factor values by the values for gasses of interest taken from the mass spectra of CuNbO-1 Trial 1 with N_2 corrected for air leak to get the final values listed in the table below.

Finalized values with corrected ionization efficiencies.

Name	CO	CO_2	N_2	NO
CuNbO-1	689.9	1846	185.5	311.5

Divide each value in the table above by the total gas composition listed above and multiply by 100 to get the percentage of each gas listed below:

Percentage of each gas in the total gas composition.

Name	CO	CO_2	N_2	NO
CuNbO-1 Trial 1	22.74 %	60.87 %	6.12 %	10.27 %

The calculation described above was repeated for each of the two trials for CuNbO-1 and the linker, an average, and standard deviation of the percent was calculated to yield the values in Figure 4.27.

4.5 Figures

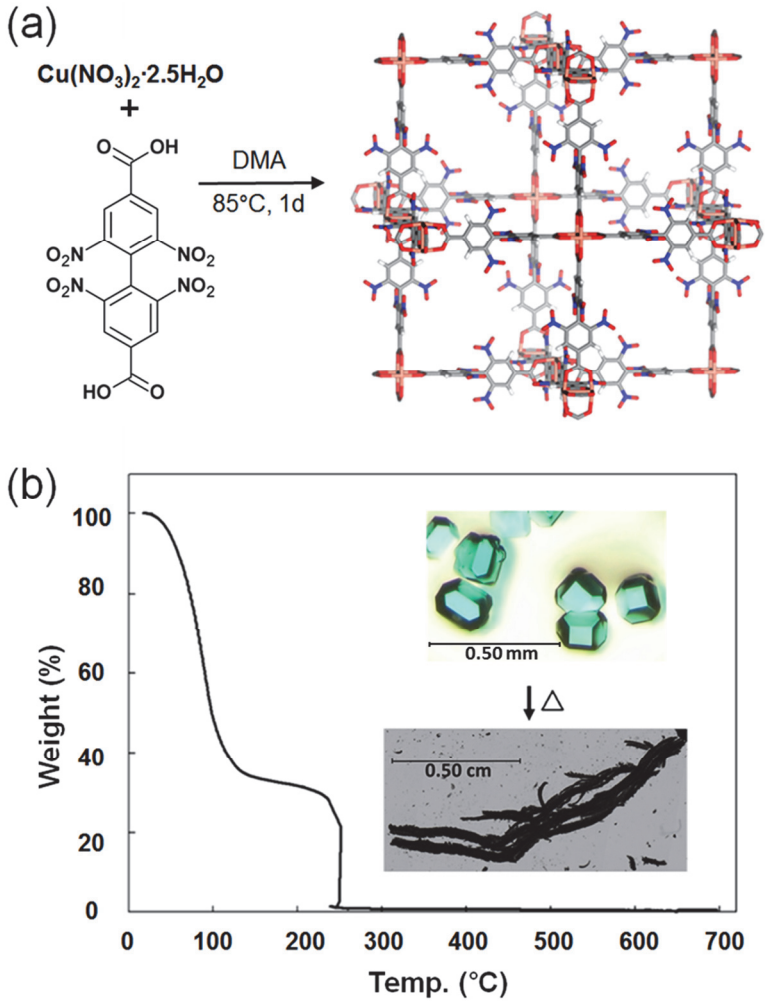

Figure 4.1. (a) Synthesis scheme and a stick model of the crystal structure of CuNbO-1. Colour codes: C, grey; H, white; N, blue; O, red; Cu, salmon. Coordinated water molecules to Cu centers are omitted for clarity. (b) TGA curve of CuNbO-1 and representative optical images of the as-synthesized CuNbO-1 crystals and their decomposition product.

Table 4.1. Crystallographic data for CuNbO-1

ORTEP drawing of the asymmetric unit at 50% probability level.	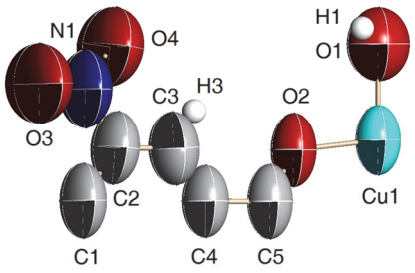

Empirical formula	$C_{14}\ H_6\ N_4\ O_{13}\ Cu$
Formula weight	501.77 g mol^{-1}
Temperature	220(2) K
Wavelength	0.900 Å
Crystal system	Cubic
Space group	*Im*(-3)*m*
Unit cell dimensions	$a = b = c = 30.261(4)$ Å
	$\alpha = \beta = \gamma = 90°$
Volume	27711(10) $Å^3$
Z	12
Density (calculated)	0.361 Mg/m^3
Absorption coefficient	0.472 mm^{-1}
F(000)	3012
Crystal size	0.30 x 0.30 x 0.20 mm^3
Theta range for data collection	2.087 to 32.058°
Index ranges	-35<=h<=35, -34<=k<=34, -33<=l<=33
Reflections collected	20215
Independent reflections	2192 [R(int) = 0.0174]
Completeness to theta = 32.058°	95.0 %
Absorption correction	None
Refinement method	Full-matrix least-squares on F2
Data / restraints / parameters	2192 / 2 / 58
Goodness-of-fit on F2	1.101
Final R indices [I>2sigma(I)]	R1 = 0.0777, wR2 = 0.2517
R indices (all data)	R1 = 0.0849, wR2 = 0.2620
Extinction coefficient	0.0046(19)
Largest diff. peak and hole	0.439 and -0.176 $e.Å^{-3}$

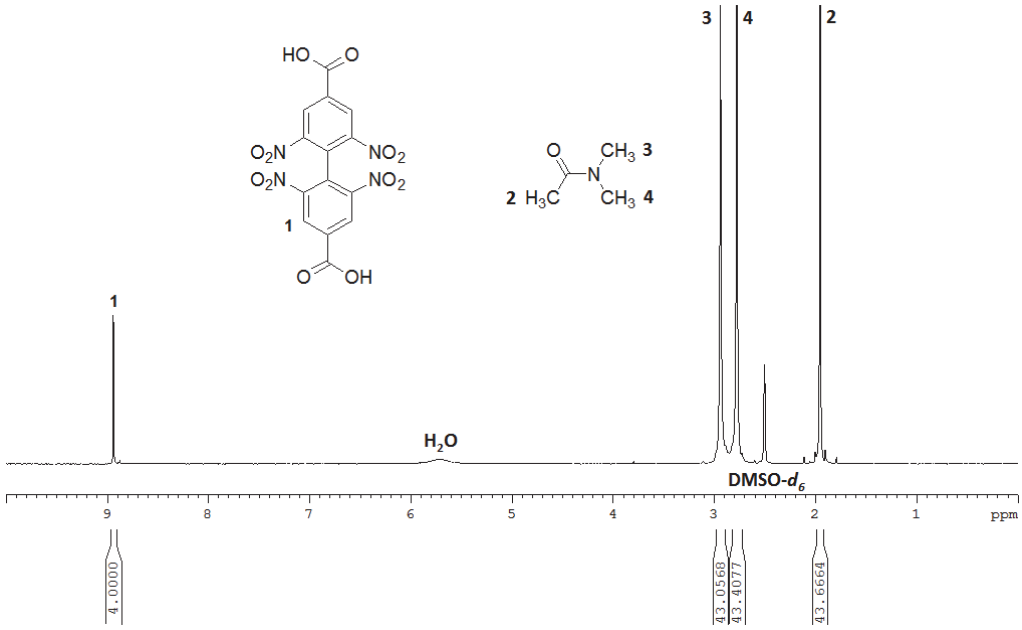

Figure 4.2. [1]H-NMR spectrum of the digested CuNbO-1 crystals in DCl/DMSO-d_6.

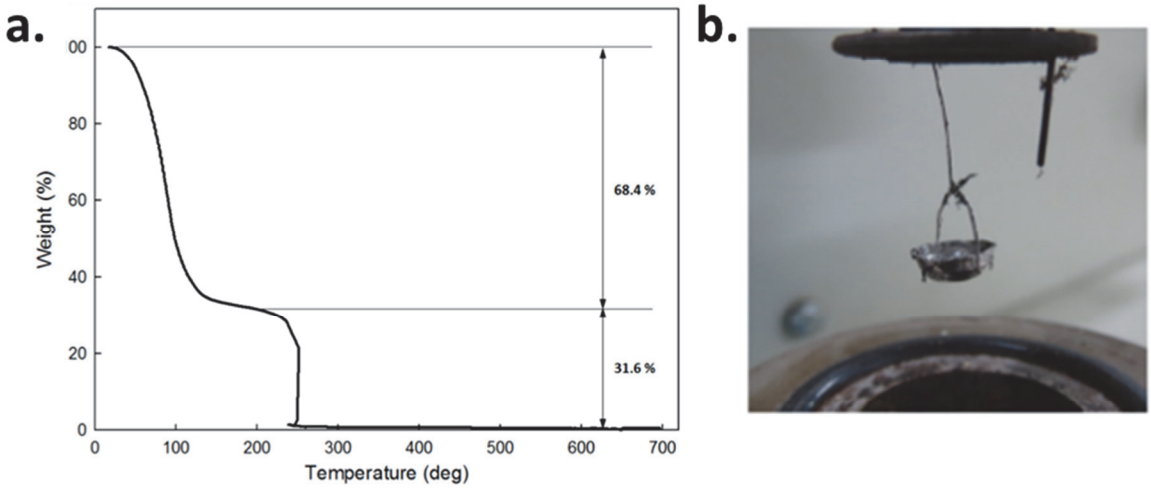

Figure 4.3. TGA thermogram of as prepared CuNbO-1 which was measured in air at a heating rate of 5 °C/min.

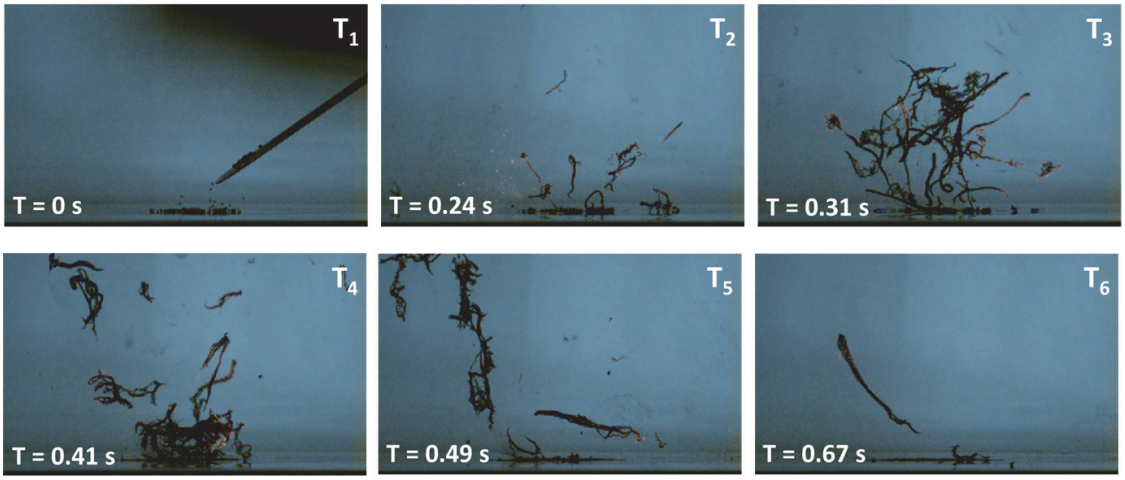

Figure 4.4. Stills taken from the high-speed imaging of the CuNbO-1 decomposition. The crystals are dropped from a spatula onto a hot plate preheated to ~330 °C. It is notable that in the T6 frame, the flying carbon composite is produced from a CuNbO-1 crystal in about 0.01 s.

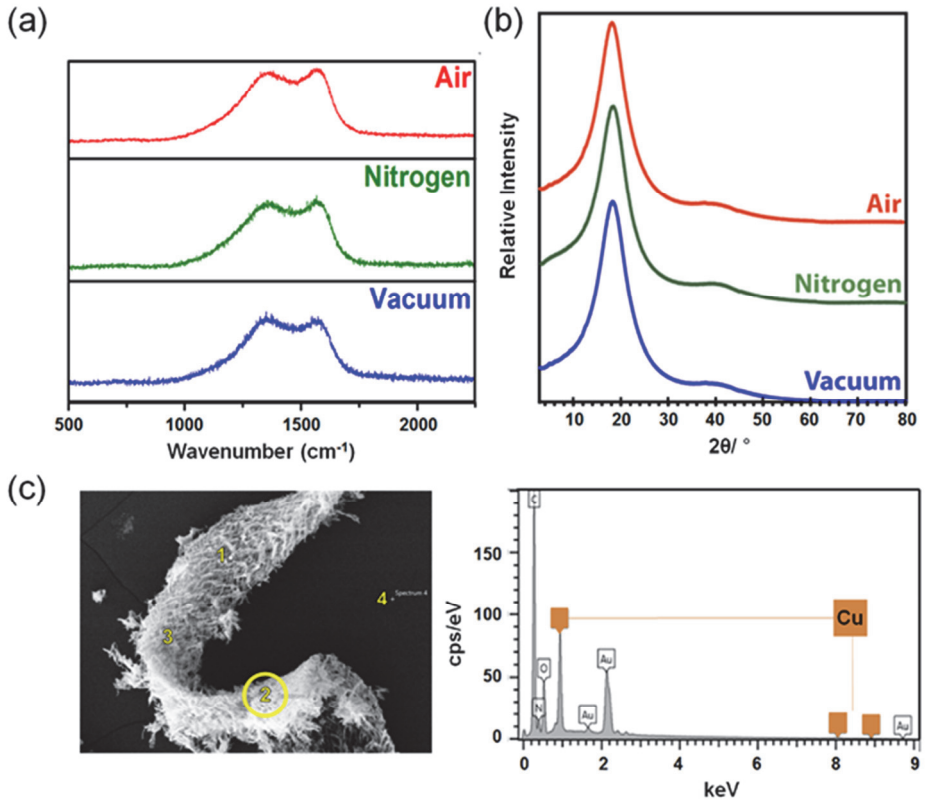

Figure 4.5. Analyses of the decomposition products of CuNbO-1 produced under air, N_2, and vacuum: (a) Raman spectra, (b) PXRD patterns (λ = 1.5418 Å), and (c) SEM-EDX mapping for the sample obtained in air, where the EDX spectrum at the position 2 (yellow circle) is shown only.

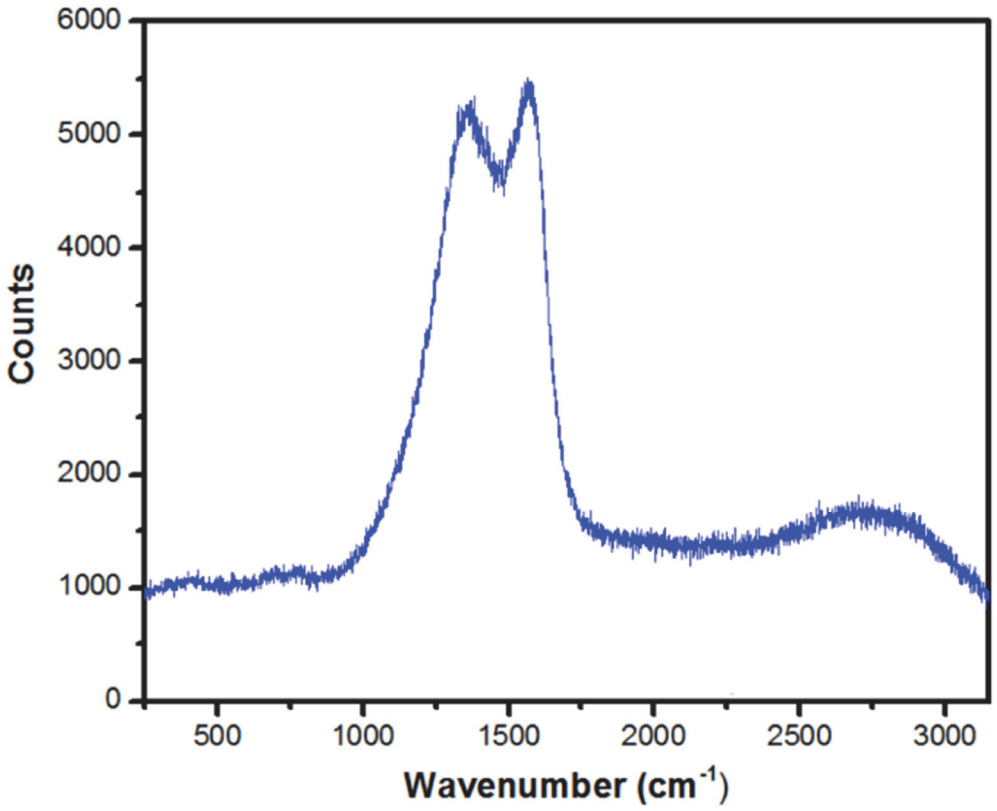

Figure 4.6. Raman spectrum of CuNbO-1 thermally decomposed in air (taken using a 633 nm laser).

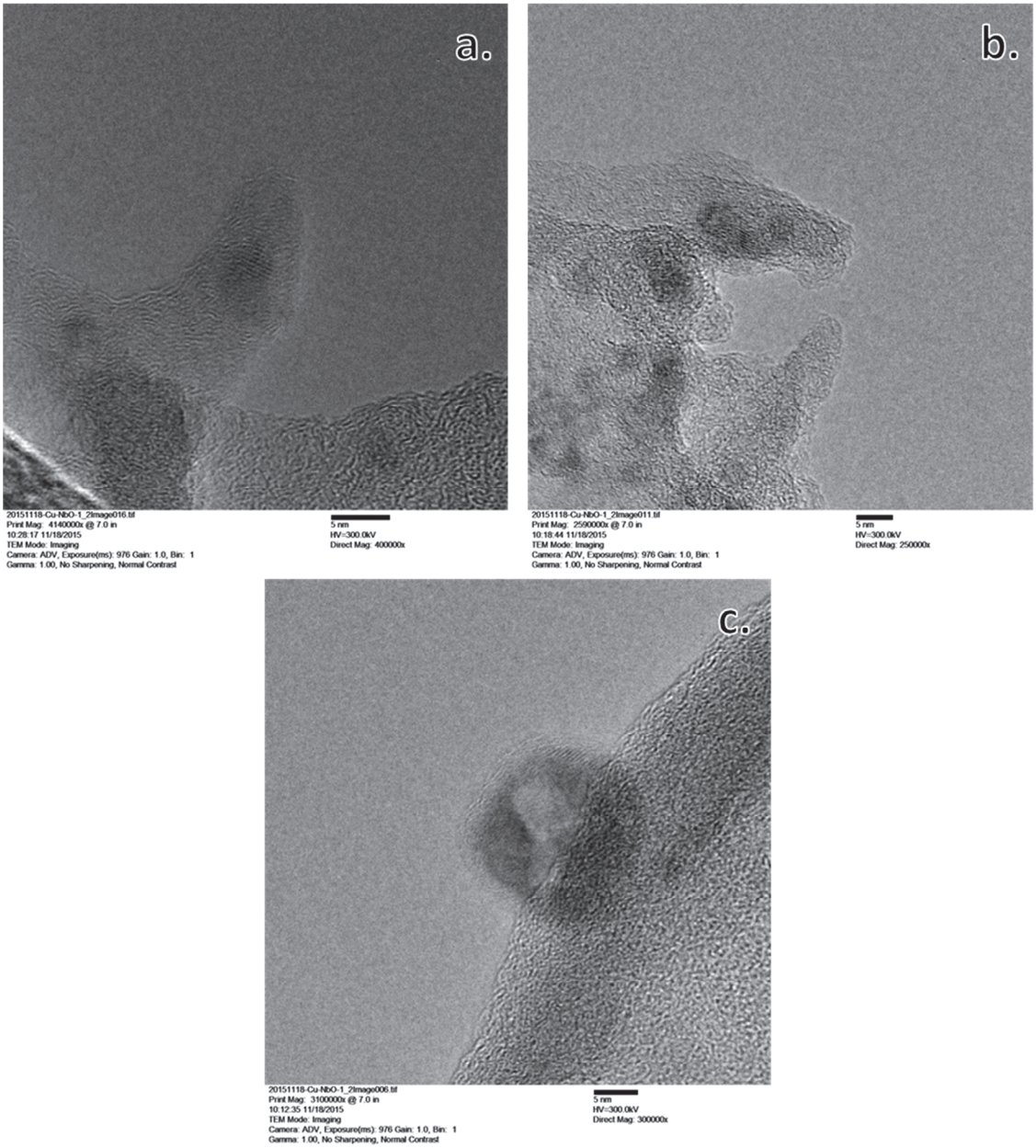

Figure 4.7. TEM images (a, b, c) of the CuNbO-1 decomposition product thermally decomposed in air showing absence of order associated with graphitic carbon. Samples were analyzed on a copper mesh support.

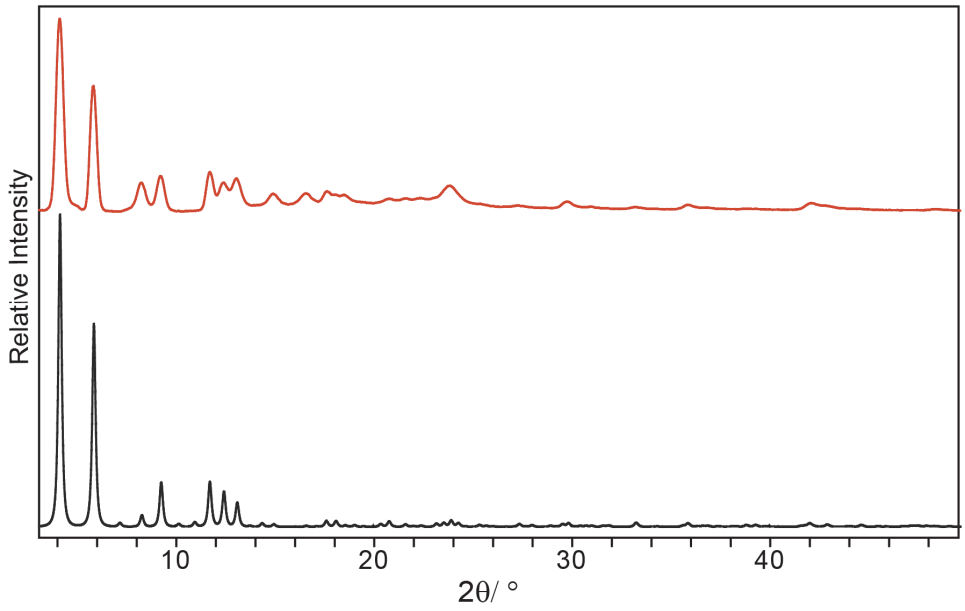

Figure 4.8. The measured (top/red) and simulated (bottom/black) PXRD patterns for CuNbO-1.

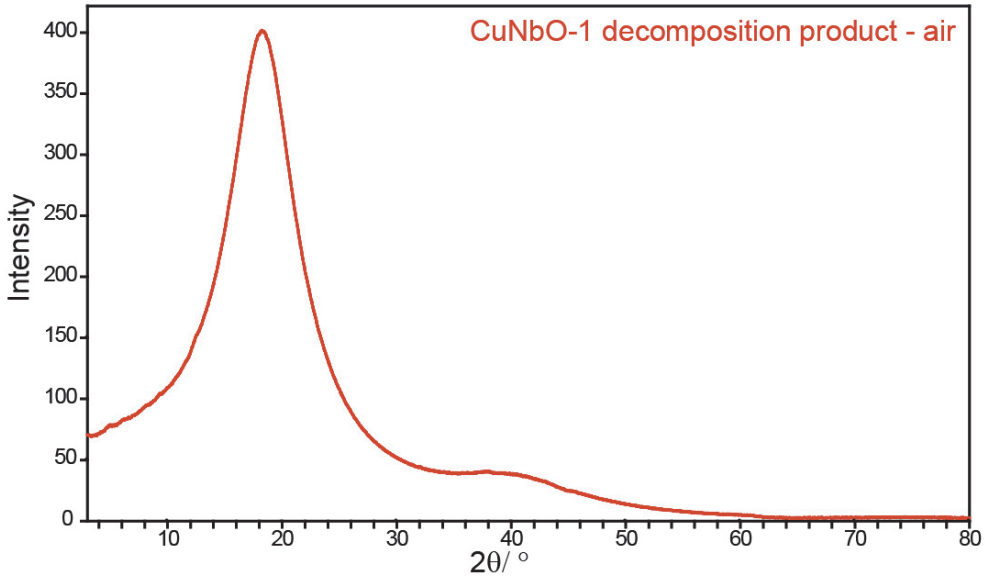

Figure 4.9. PXRD pattern of the decomposition product of CuNbO-1 thermally decomposed in air.

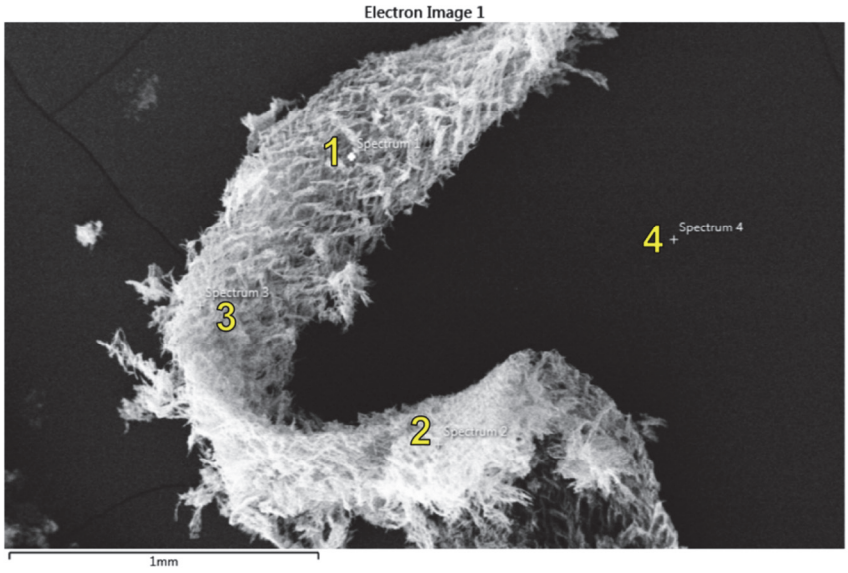

Figure 4.10. SEM image of gold-coated CuNbO-1 decomposition product initiated in air and labelled at points where EDS spectra were taken.

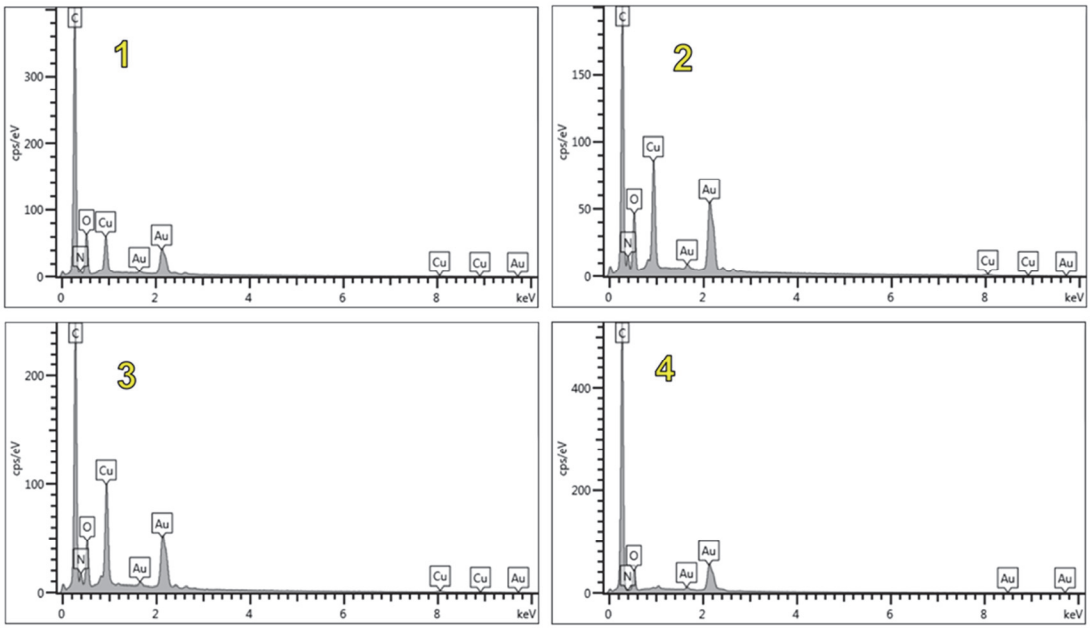

Figure 4.11. EDS spectrum showing the elemental composition at position 1, 2, 3, and 4 marked on the SEM image in Figure 4.10.

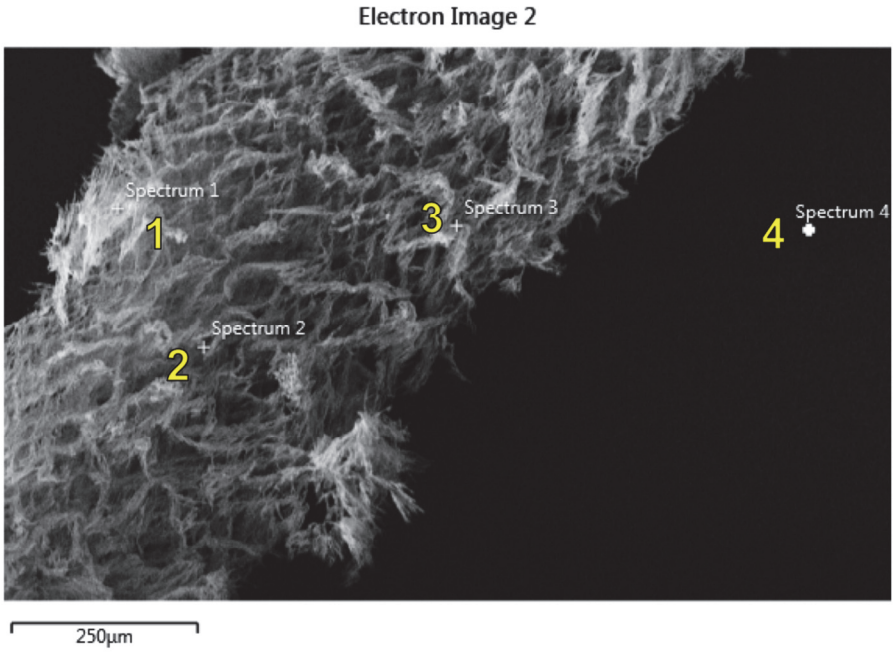

Figure 4.12. SEM image of gold-coated CuNbO-1 decomposition product initiated in air and labelled at points where EDS spectra were taken.

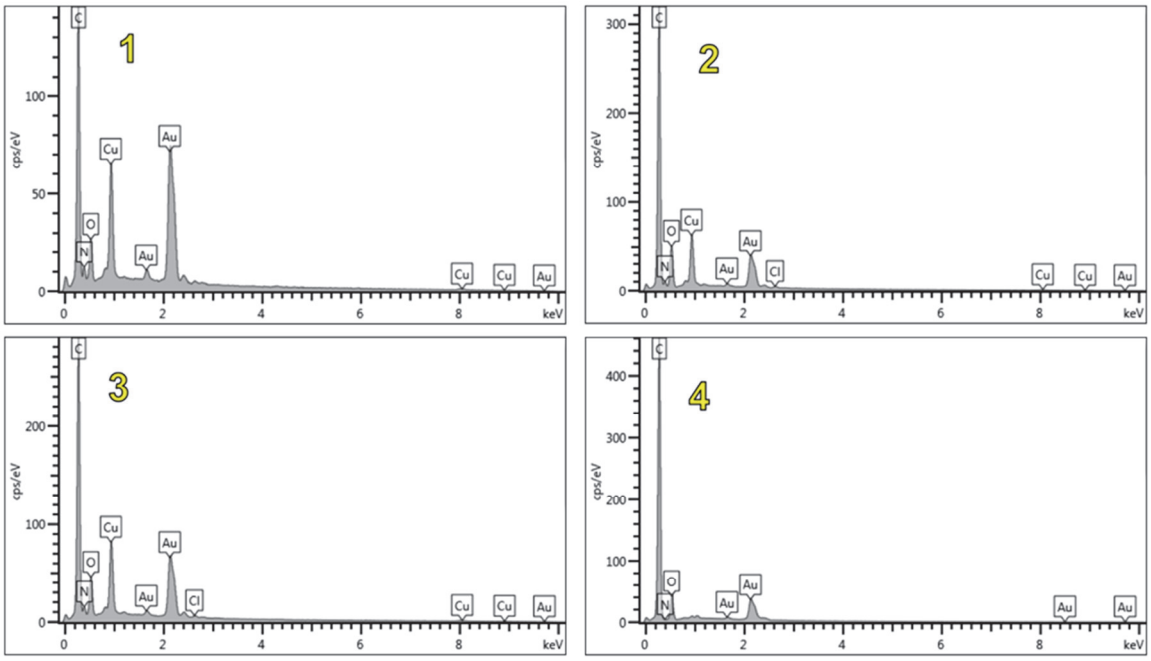

Figure 4.13. EDS spectrum showing the elemental composition at position 1, 2, 3, and 4 marked on the SEM image in Figure 4.12.

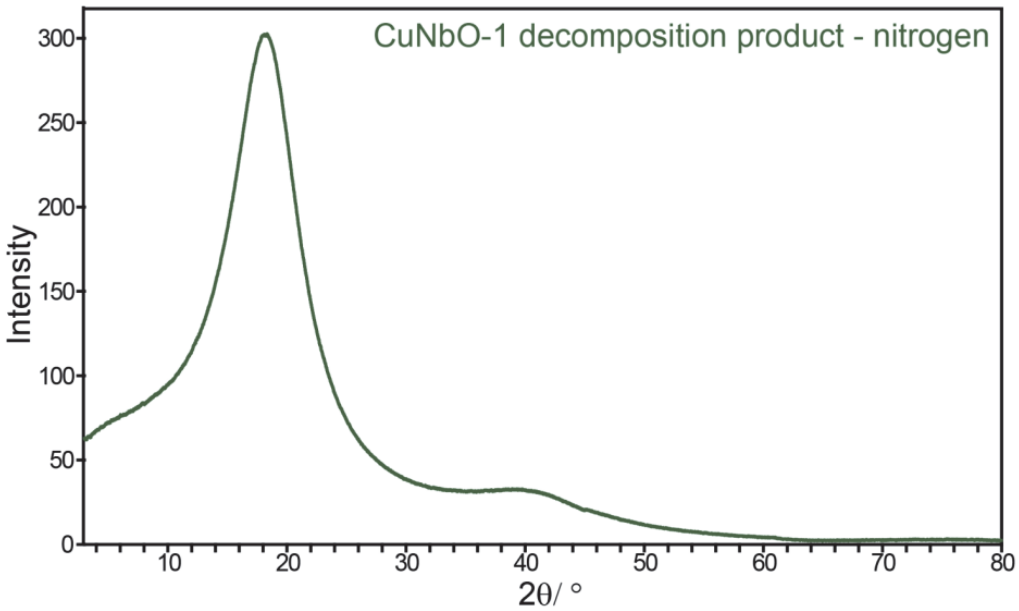

Figure 4.14. PXRD pattern of the decomposition product of CuNbO-1 thermally decomposed under nitrogen.

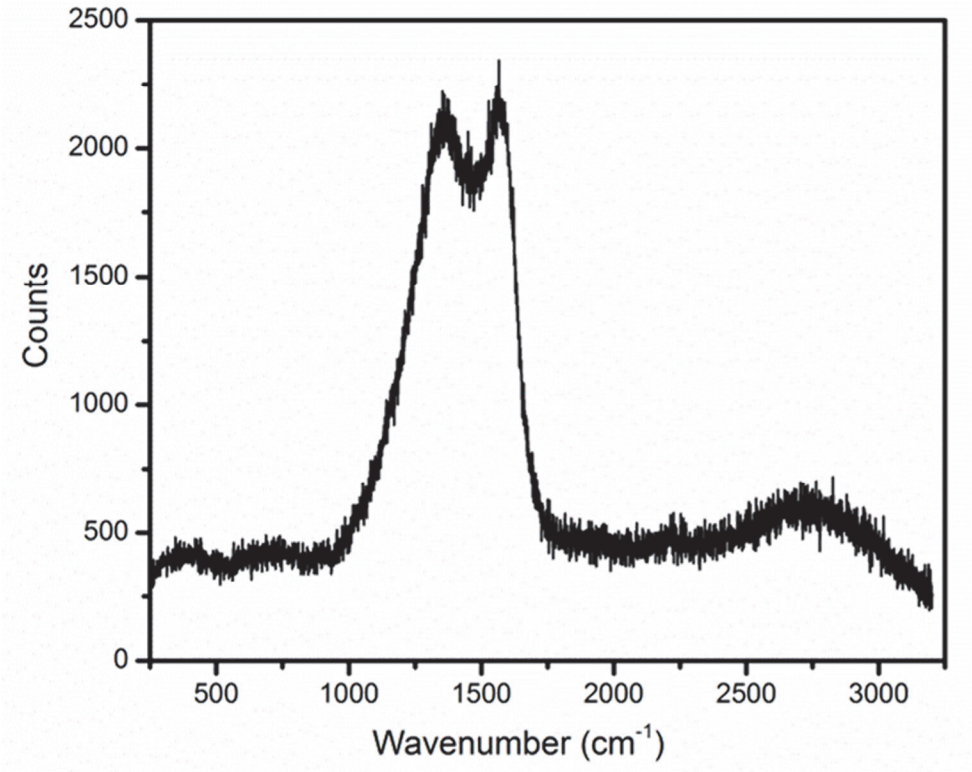

Figure 4.15. Raman Spectrum of CuNbO-1 thermally decomposed under nitrogen (taken using a 633 nm laser).

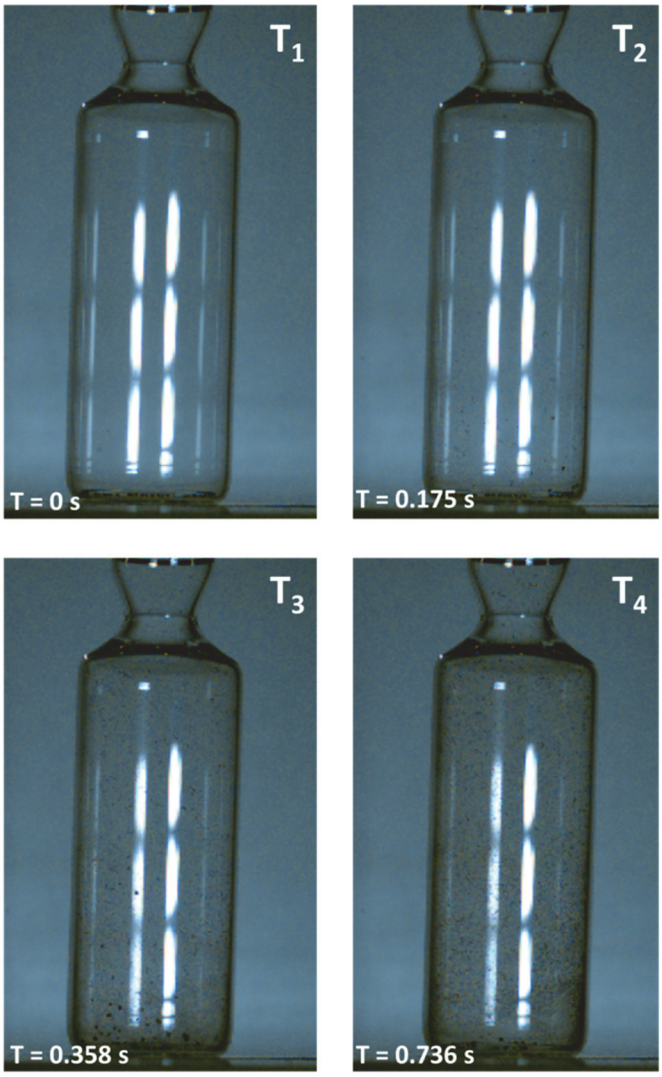

Figure 4.16. Stills taken from the high speed imaging of the CuNbO-1 decomposition sealed under vacuum (~0.03 torr). The sealed ampoule was placed onto a hot plate preheated to ~330 °C.

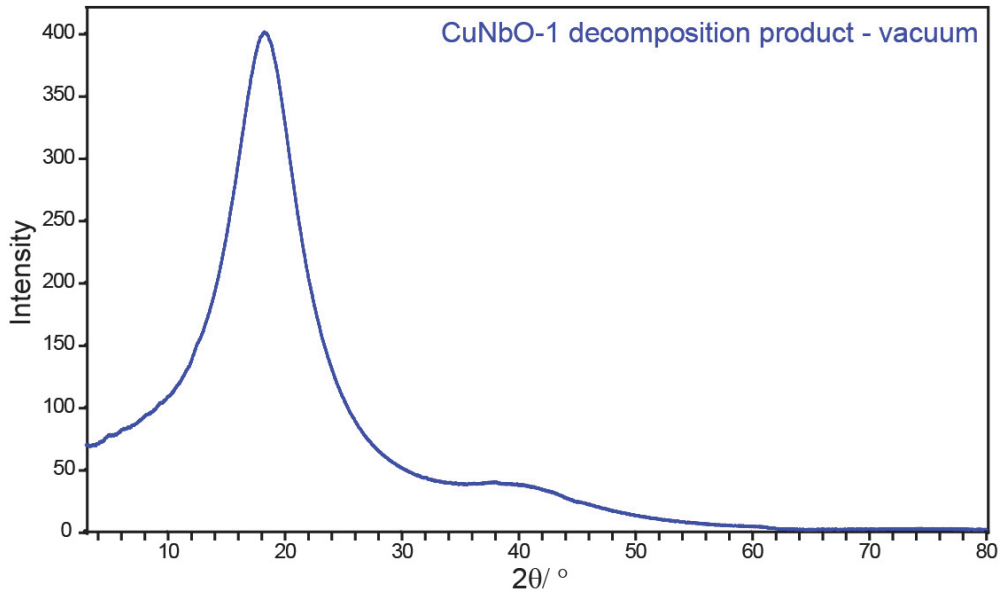

Figure 4.17. PXRD pattern of the decomposition product of CuNbO-1 thermally decomposed under vacuum (~0.03 Torr).

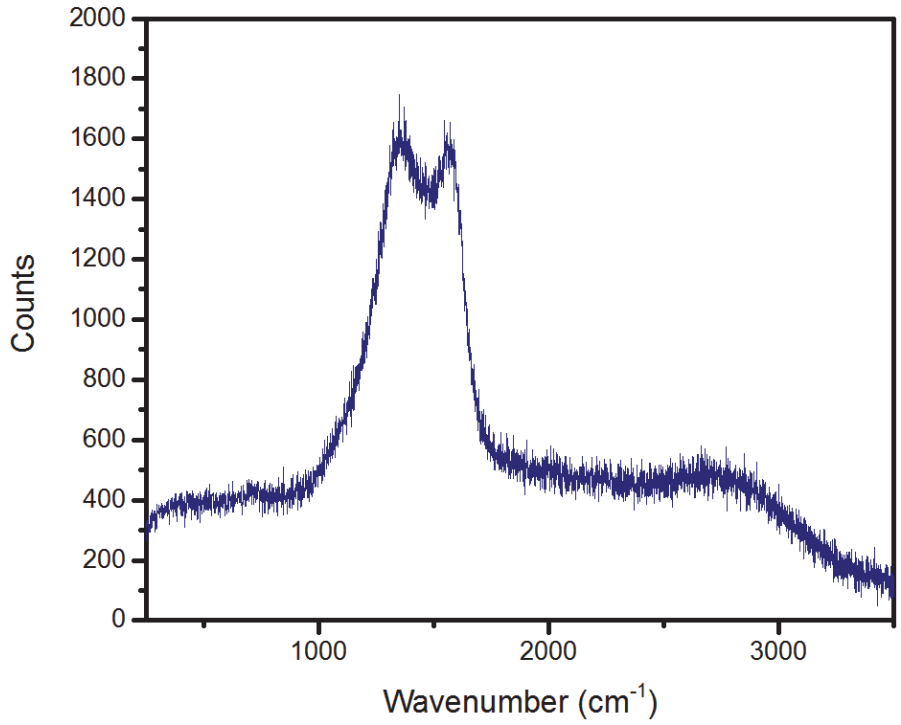

Figure 4.18. Raman Spectrum of CuNbO-1 thermally decomposed under vacuum (~0.03 Torr; taken using a 633 nm laser).

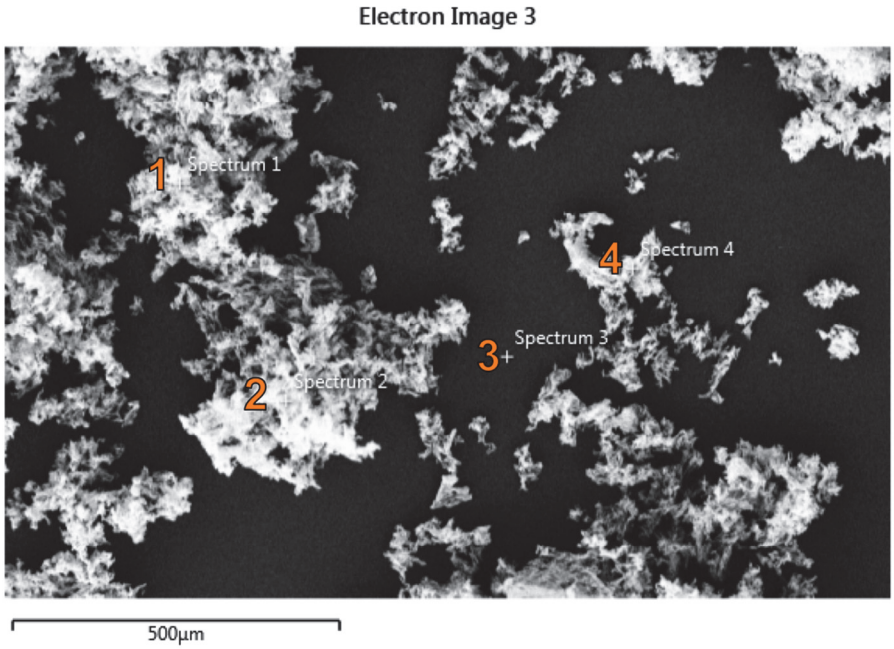

Figure 4.19. SEM image of gold-coated CuNbO-1 decomposition product initiated under vacuum (~0.03 torr) and labelled at points where EDS spectra were taken.

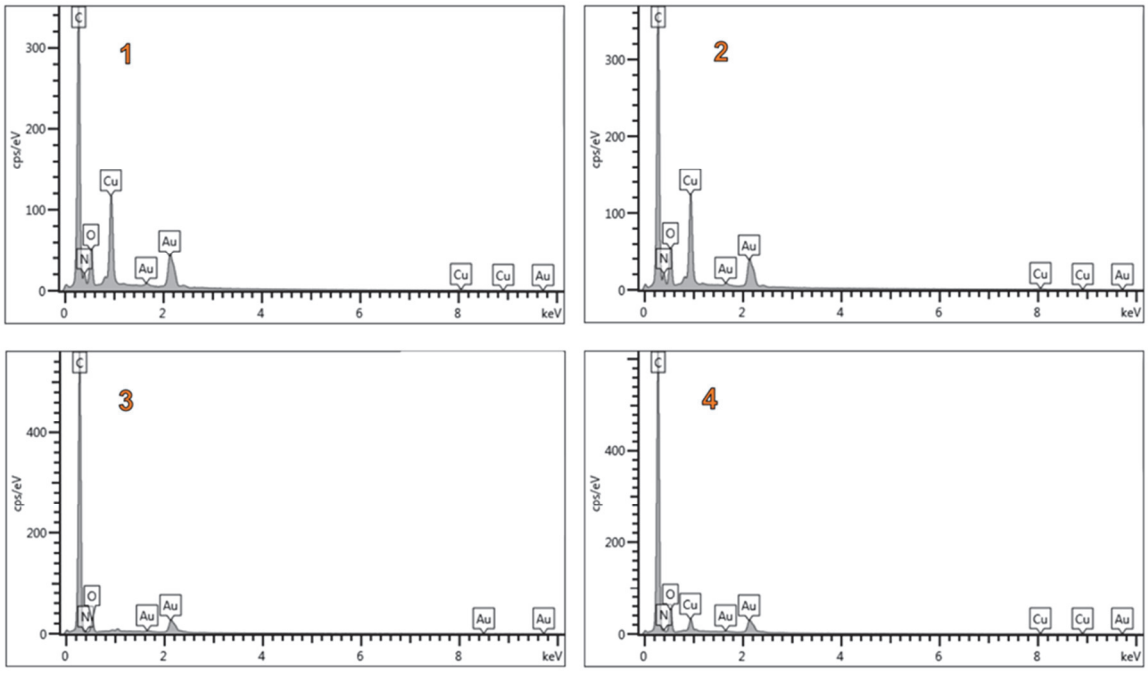

Figure 4.20. EDS spectrum showing the elemental composition at position 1, 2, 3, and 4 marked on the SEM image in Figure 4.19.

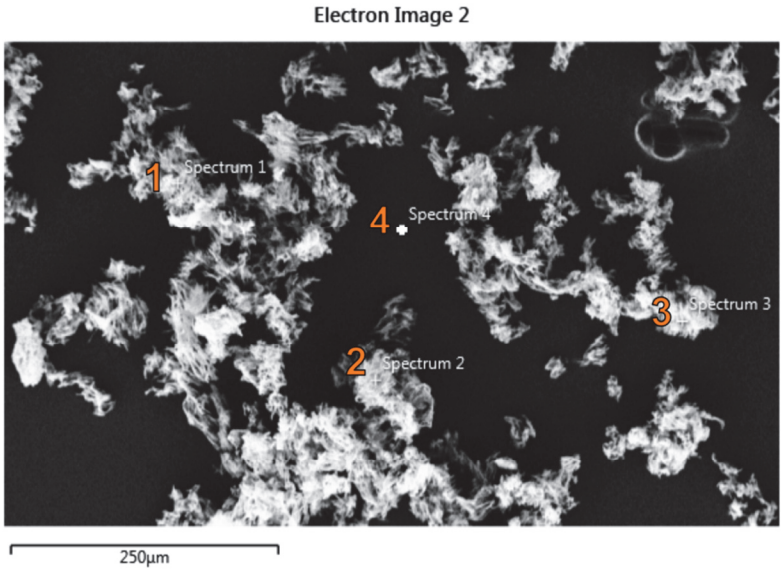

Figure 4.21. SEM image of gold-coated CuNbO-1 decomposition product initiated under vacuum (~0.03 torr) and labelled at points where EDS spectra were taken.

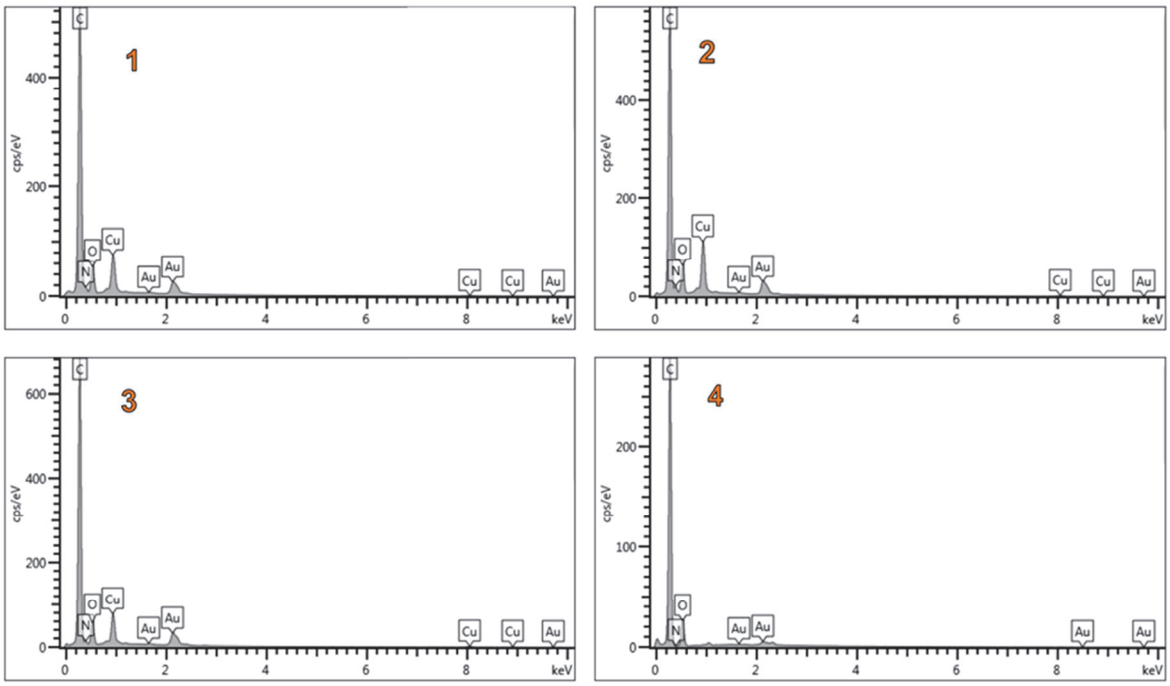

Figure 4.22. EDS spectrum showing the elemental composition at position 1, 2, 3, and 4 marked on the SEM image in Figure 4.21.

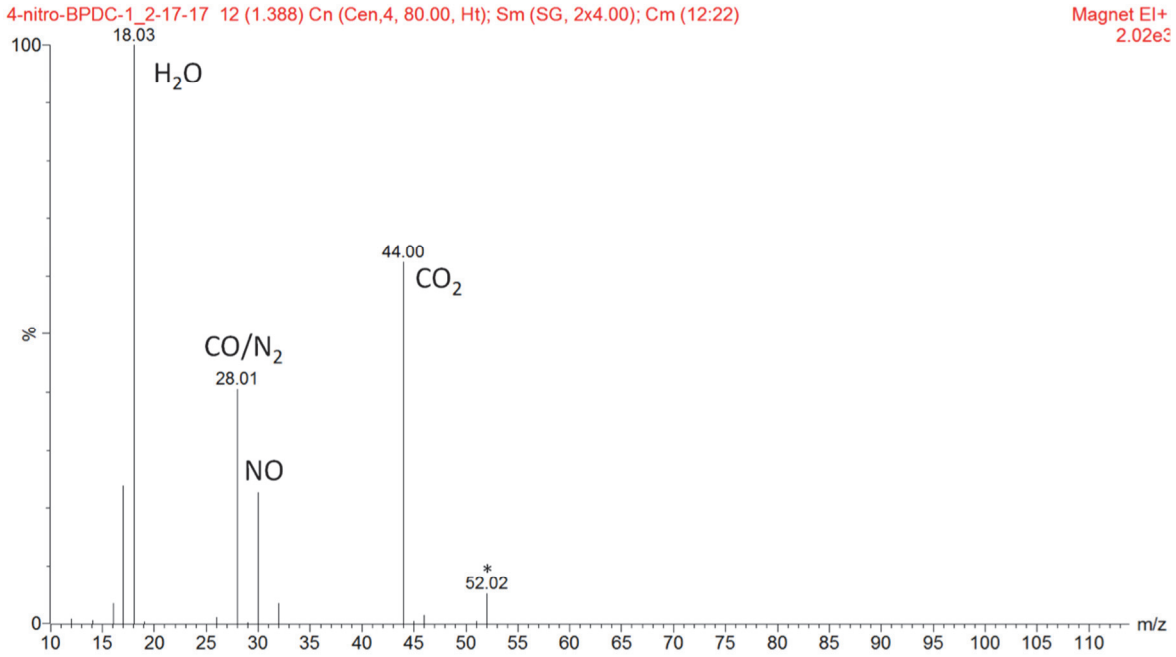

Figure 4.23. Representative mass spectra of the gaseous decomposition products of the $H_2(NO_2)_4$BPDC linker. Signals above 5 % relative abundance have been labelled on the spectra. Signal at 52 corresponds to a background peak from the mass spectrometer. Water concentration is not analyzed because it condenses and therefore its concentration cannot be determined from observing the gas phase composition.

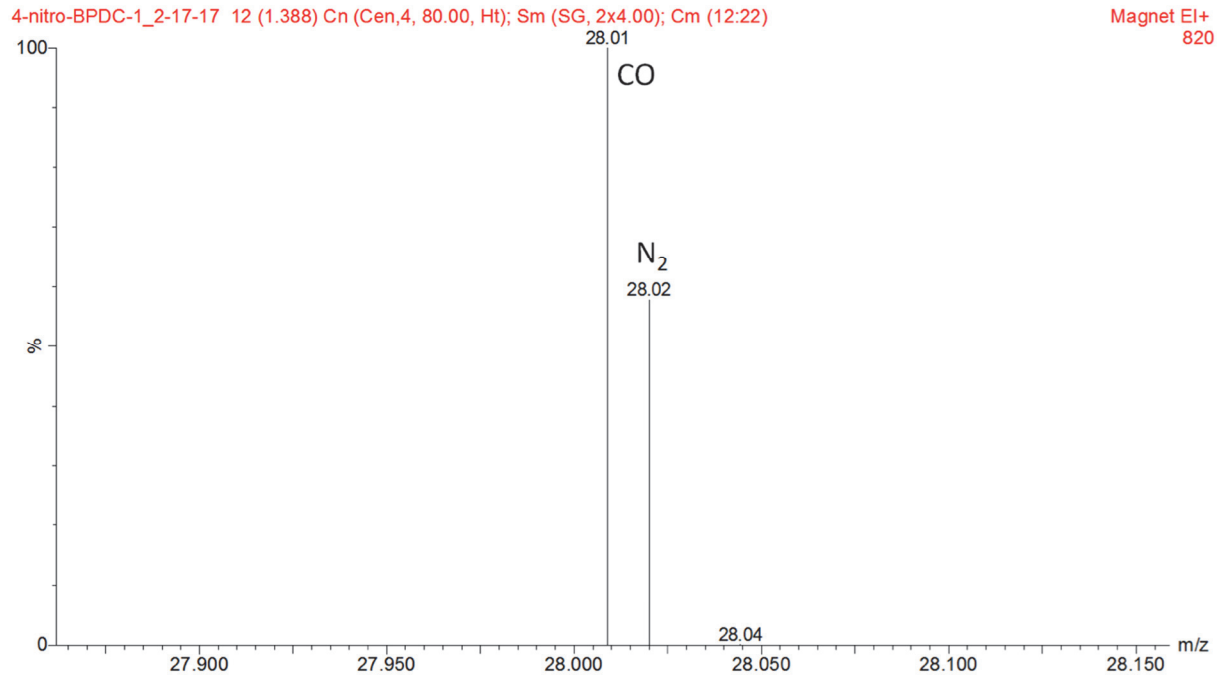

Figure 4.24. Representative mass spectra of the gaseous decomposition products of the $H_2(NO_2)_4$BPDC linker showing the resolution of the CO/N_2 peaks.

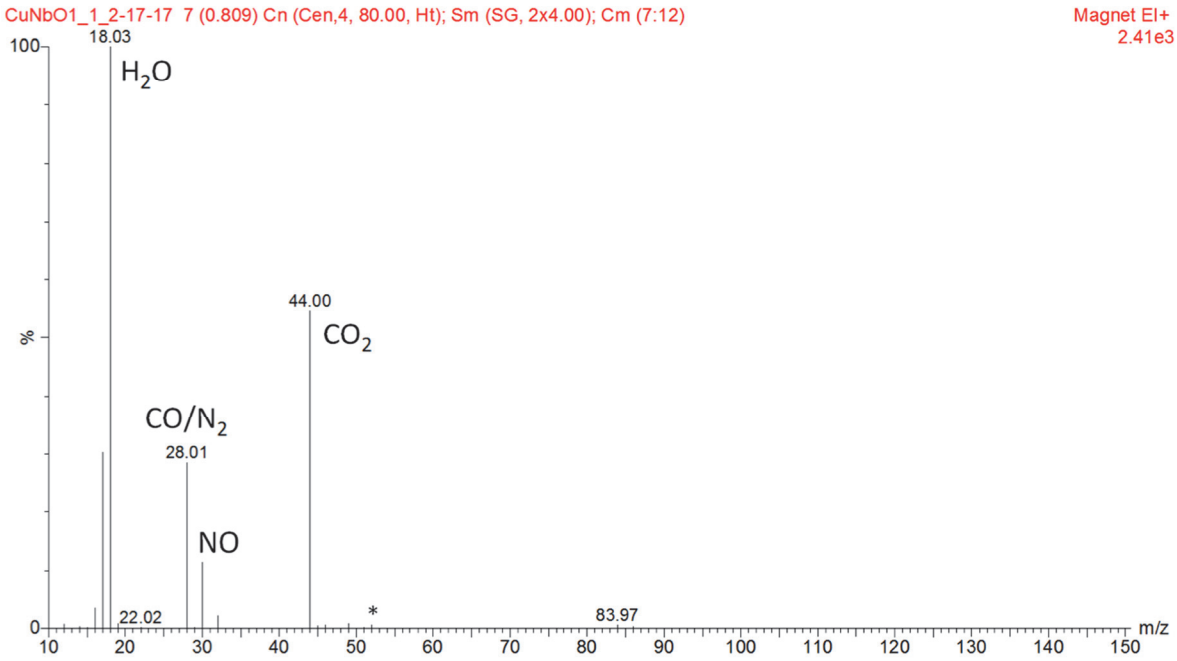

Figure 4.25. Representative mass spectra of the gaseous decomposition products of CuNbO-1.

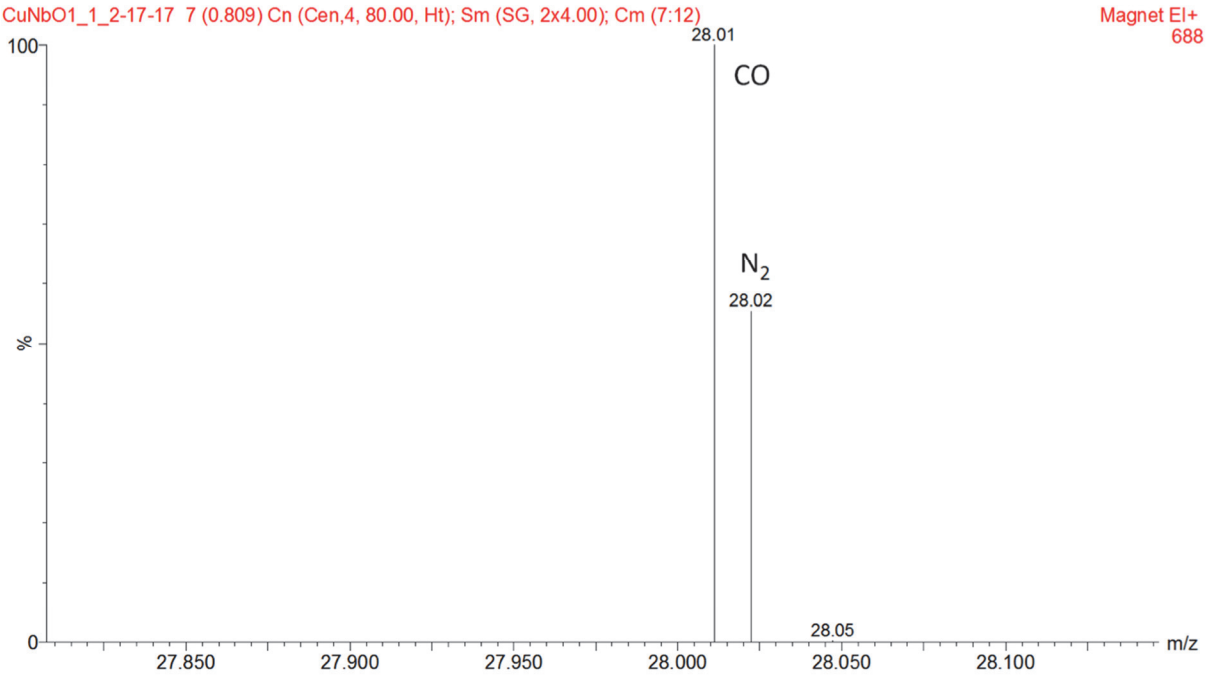

Figure 4.26. Representative mass spectra of the gaseous decomposition products of CuNbO-1 showing the resolution of the CO/ N_2 peaks.

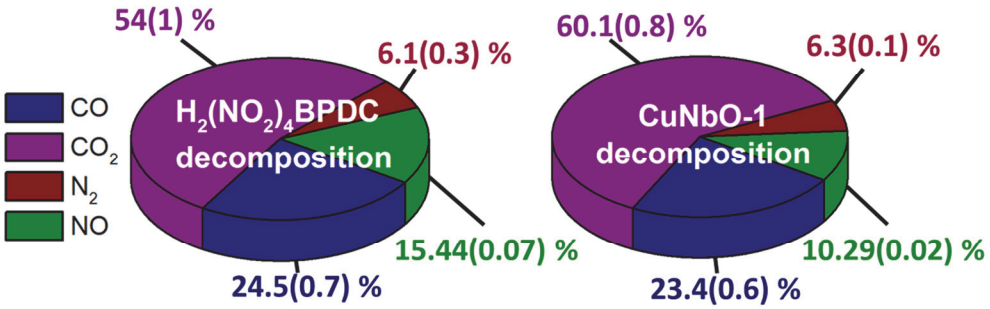

Figure 4.27. The relative percentages of CO, CO_2, N_2, and NO in the gaseous decomposition products of the $H_2(NO_2)_4$BPDC linker and CuNbO-1 taken from the high-resolution mass spectra obtained by decomposition gas analysis.

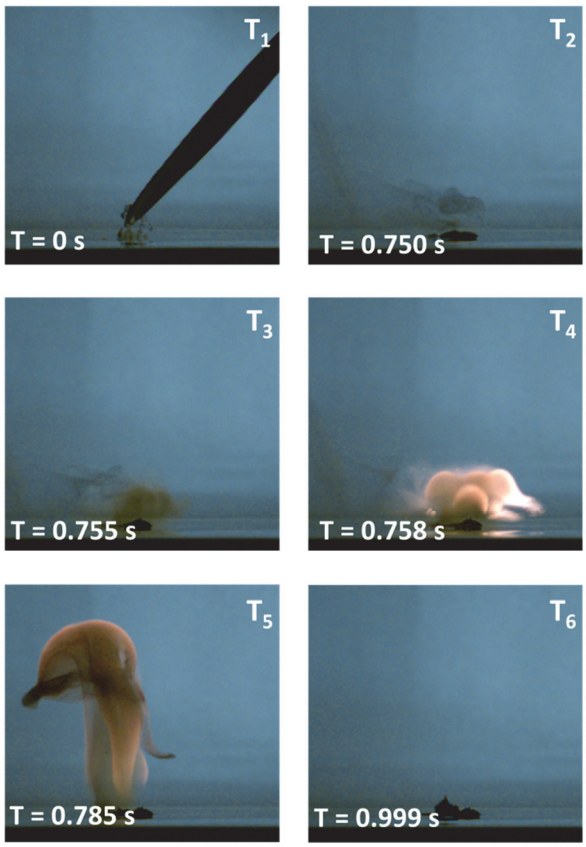

Figure 4.28. Stills taken from the high speed imaging of the $H_2(NO_2)_4$BPDC linker decomposition. The sample was dropped onto a hot plate preheated to ~330 °C.

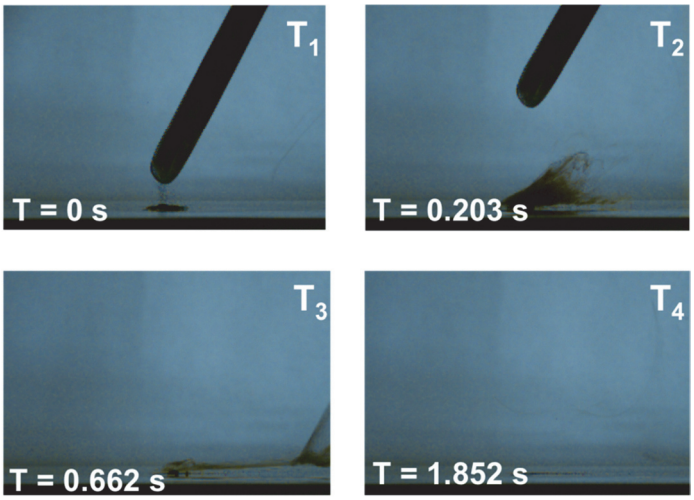

Figure 4.29. Stills taken from the high speed imaging of copper (II) acetate decomposition. The sample was dropped onto a hot plate preheated to ~330 °C.

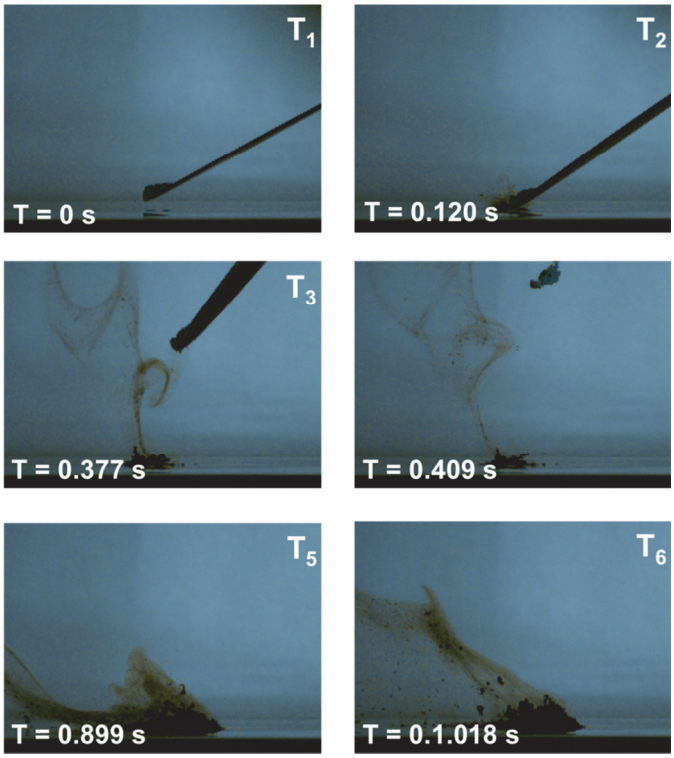

Figure 4.30. Stills taken from the high speed imaging of the physical mixture of copper (II) acetate with the $H_2(NO_2)_4BPDC$ linker decomposition. The mixture was prepared using a 1:1 molar ratio of metal to linker to most closely mimic the CuNbO-1 system and dropped onto a hot plate preheated to ~330 °C.

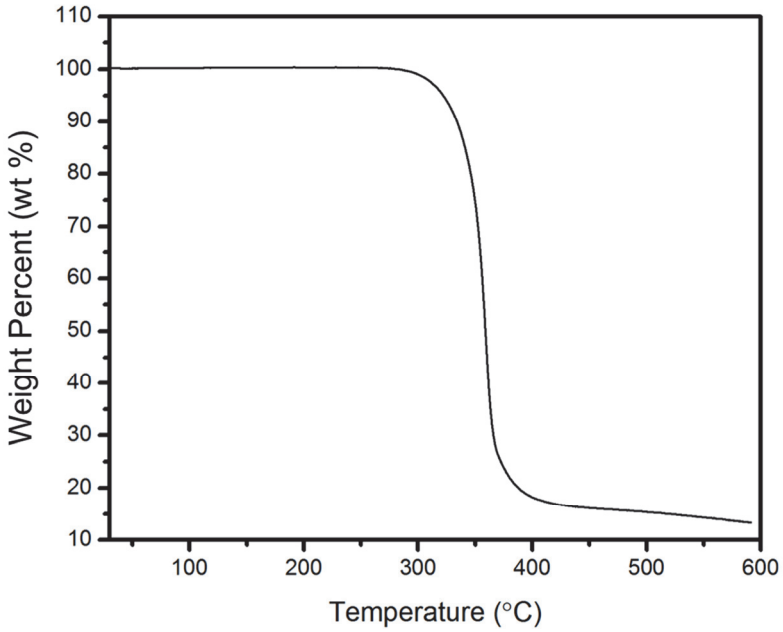

Figure 4.31. TGA thermogram of the dried $H_2(NO_2)_4$BPDC ligand measured under a nitrogen atmosphere at a heating rate of 10 °C/min

Table 4.2. Crystallographic data for CuNbO-2

ORTEP drawing of the asymmetric unit at 50% probability level. The $–NO_2$ groups and free DMAs have partial site-occupancy factors of 0.5, respectively. The coordinated DMA to Cu1 is disordered over four sites with equal probabilities; only one of them is shown for simplicity. The H atoms in the CH_3 groups of DMA molecules are not shown for clarity.	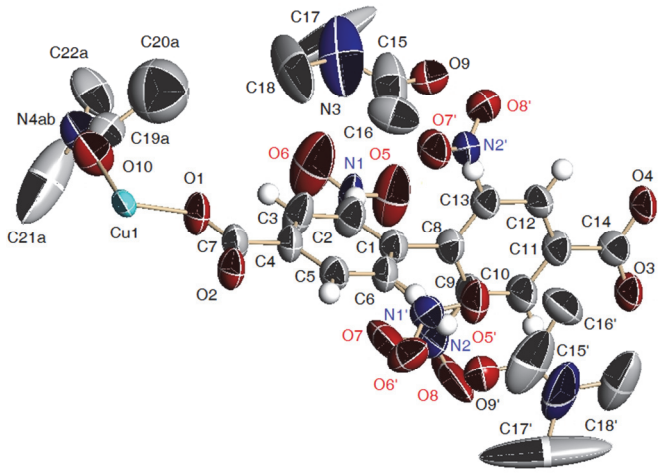
Empirical formula	$C_{22}\ H_{24}\ N_4\ O_{10}\ Cu$

Formula weight	567.99 g mol^{-1}
Temperature	95(2) K
Wavelength	0.800 Å
Crystal system	Trigonal
Space group	*R*(-3)
Unit cell dimensions	*a* = 45.724(7) Å □= 90°.
	b = 45.724(7) Å □= 90°.
	c = 10.778(2) Å □ = 120°
Volume	19514(7) Å3
Z	18
Density (calculated)	0.870 Mg/m^3
Absorption coefficient	0.742 mm^{-1}
F(000)	5274
Crystal size	0.10 x 0.10 x 0.005 mm^3
Theta range for data collection	1.737 to 28.688°
Index ranges	-46<=h<=47, -54<=k<=54, -12<=l<=12
Reflections collected	22484
Independent reflections	7726 [R(int) = 0.0301]
Completeness to theta = 28.685°	98.5 %
Absorption correction	None
Refinement method	Full-matrix least-squares on F2
Data / restraints / parameters	7726 / 135 / 536
Goodness-of-fit on F2	1.510
Final R indices [I>2sigma(I)]	R1 = 0.0998, wR2 = 0.3196
R indices (all data)	R1 = 0.1055, wR2 = 0.3247
Extinction coefficient	n/a
Largest diff. peak and hole	0.983 and -0.724 e.$Å^{-3}$

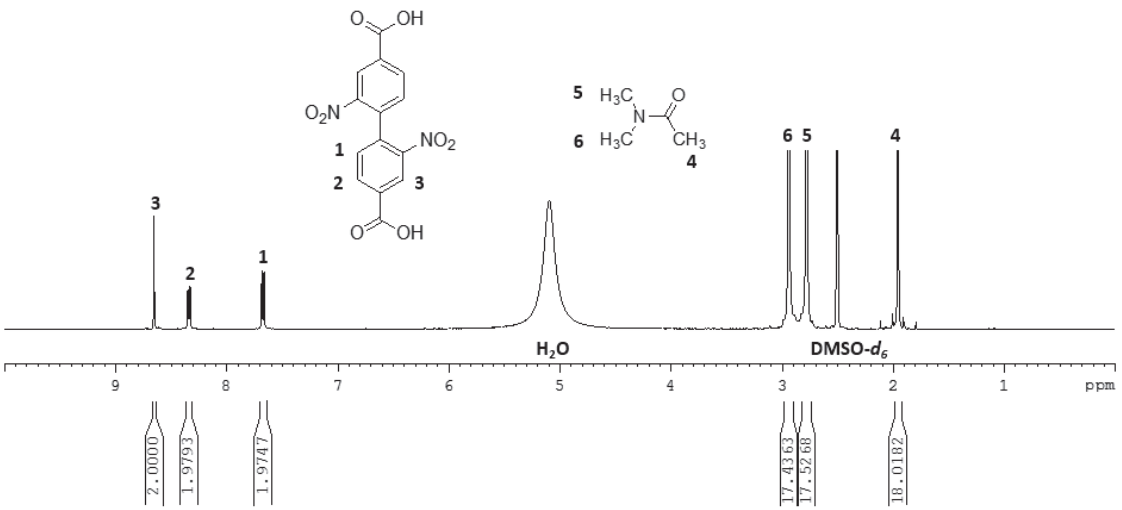

Figure 4.32. ^{1}H-NMR spectrum of the digested $[Cu(dnpdc)(H_2O)]_n(DMA)_4(H_2O)_2$ crystals in DCl/DMSO-d_6.

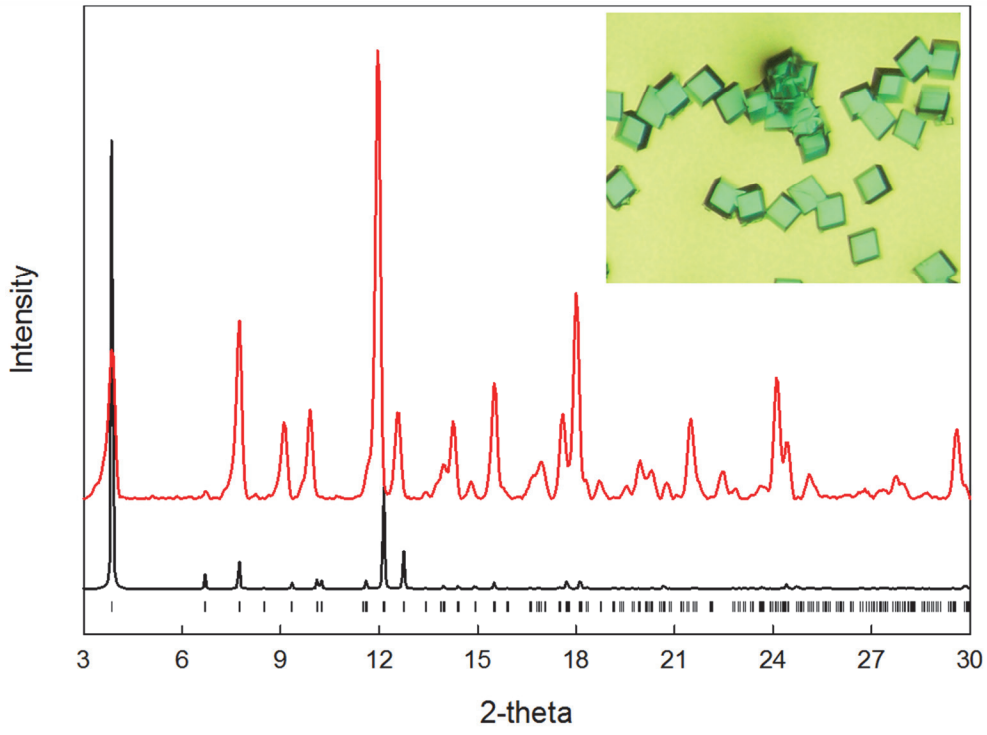

Figure 4.33. The measured (red) and simulated (black) PXRD patterns for $[Cu(dnpdc)(H_2O)]_n(DMA)_4(H_2O)_2$.

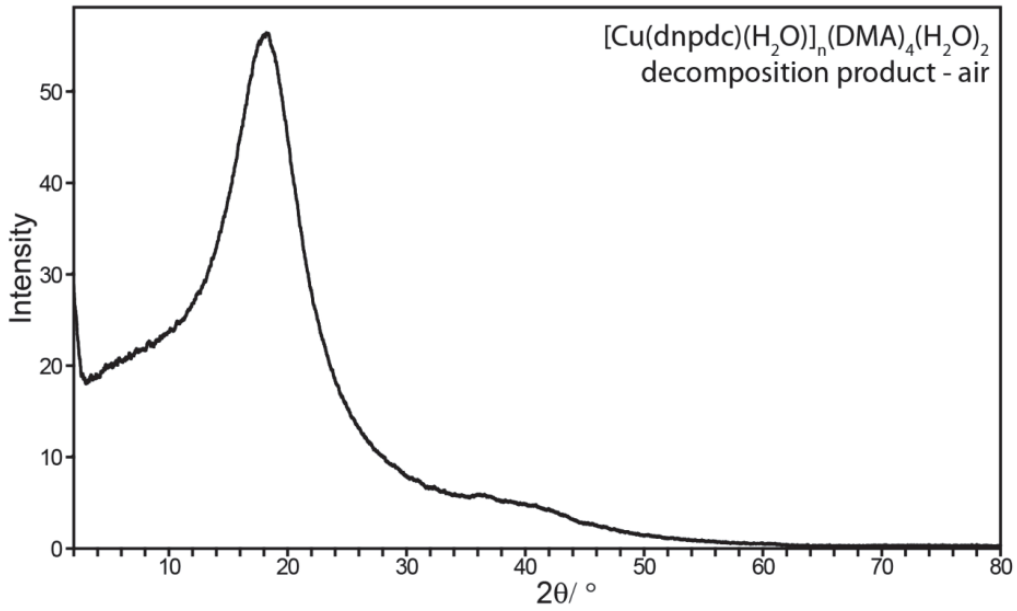

Figure 4.34. PXRD pattern of the decomposition product of $[Cu(dnpdc)(H_2O)]_n(DMA)_4(H_2O)_2$ decomposed in air.

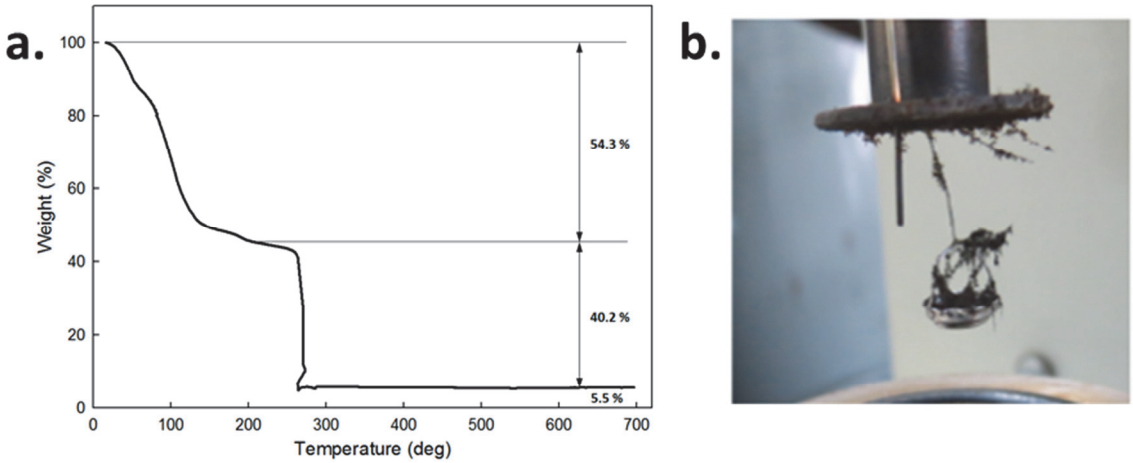

Figure 4.35. TGA thermogram of as prepared $[Cu(dnpdc)(H_2O)]_n(DMA)_4(H_2O)_2$ which was measured in air at a heating rate of 5 °C/min.

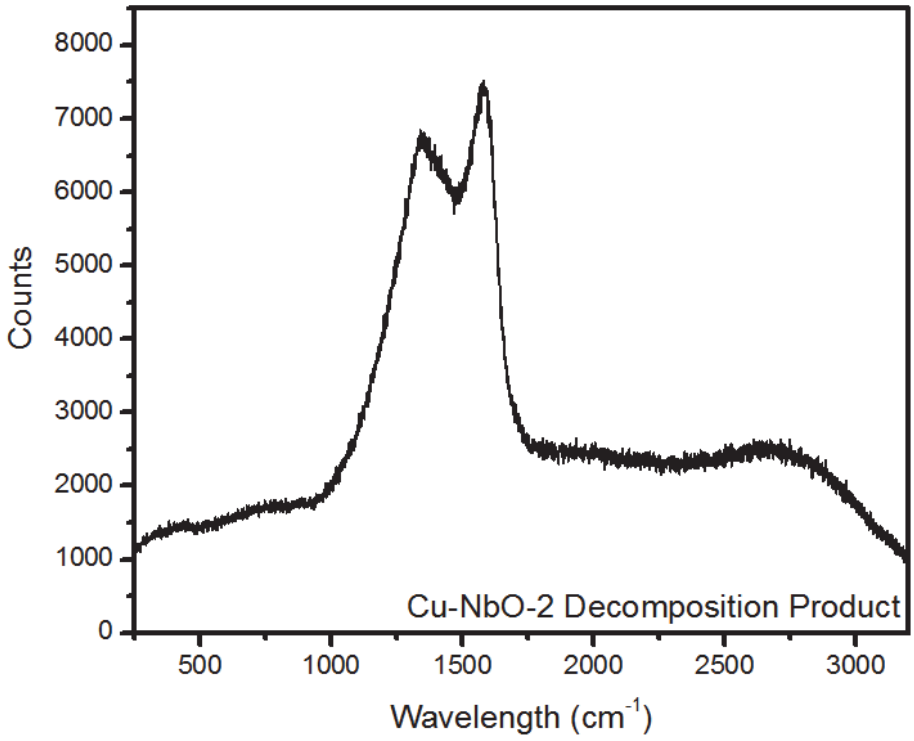

Figure 4.36. Raman spectrum of $[Cu(dnpdc)(H_2O)]_n(DMA)_4(H_2O)_2$ thermally decomposed in air (taken using a 633 nm laser).

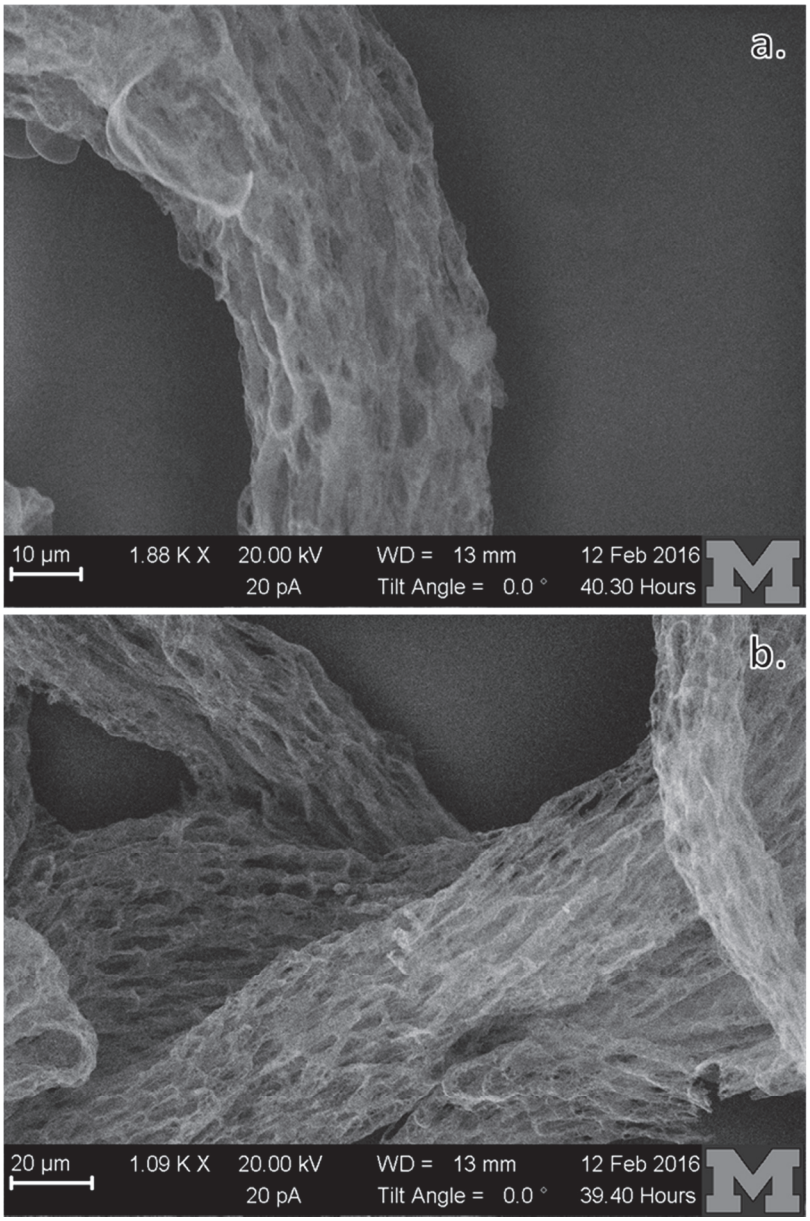

Figure 4.37. SEM images (a-b) of gold-coated $[Cu(dnpdc)(H_2O)]_n(DMA)_4(H_2O)_2$ decomposition product initiated in air.

4.6 References

(1) McDonald, K. A.; Seth, S.; Matzger, A. J. *Cryst. Growth. Des.* **2015**, *15*, 5963.

(2) Zhang, S.; Yang, Q.; Liu, X.; Qu, X.; Wei, Q.; Xie, G.; Chen, S.; Gao, S. *Coord. Chem. Rev.* **2016**, *307*, 292.

(3) Zhang, Q.; Shreeve, J. M. *Angew. Chem., Int. Ed.* **2014**, *53*, 2540.

(4) There are now examples of structure-property relationships where the effects of coordination polymerization on the properties of nitrogen-rich energetic heterocycles have been elucidated.

(5) Klapötke, T. M. *Chemistry of High-Energy Materials*, Walter de Gruyter, Berlin/Boston, 2012, p. 83-85.

(6) Meyer, R.; K¨ohler, J.; Homburg, A., *Explosives*, Wiley-VCH, Weinheim, 2007, p. 131.

(7) Yang, S. J.; Kim, T.; Im, J. H.; Kim, Y. S.; Lee, K.; Jung, H.; Park, C. R. *Chem. Mater*. **2012**, *24*, 464.

(8) Carrasco, J. A.; Romero, J.; Abellán, G.; Hernández-Saz, J.; Molina, S. I.; Martí-Gastaldo, C.; Coronado, E. *Chem. Commun*. **2016**, *52*, 9141.

(9) Salunkhe, R. R.; Kaneti, Y. V.; Kim, J.; Kim, J. H.; Yamauchi, Y. *Acc. Chem. Res*. **2016**, *49*, 2796.

(10) Typically thermolysis/pyrolysis of MOFs leads to carbon supports that are morphologically similar to the parent MOF.

(11) Furukawa, H. ; Kim, J.; Ockwig, N. W.; O'Keeffe, M.; Yaghi, O. M.; *J. Am. Chem. Soc*. **2008**, *130*, 11650.

(12) Jeong, K. S.; Go, Y. B.; Shin, S. M.; Lee, S. J.; Kim, J.; Yaghi, O. M.; Jeong, N. *Chem. Sci*. **2011**, *2*, 877.

(13) Chu, P. K.; Li, L. *Materials Chemistry and Physics*. **2006**, *96*, 253.

(14) Ferrari, A. C.; Robertson, J. *Phys. Rev. B*. **2000**, *61*, 14095.

(15) Sadezky, A.; Muckenhuber, H.; Grothe, H.; Niessner, R.; Pöschl, U.; *Carbon*. **2005**, *43*, 1731.

(16) Low, C. T. J.; Walsh, F. C.; Chakrabarti, M. H.; Hashim, M. A.; Hussain, M. A. *Carbon*. **2013**, *54*, 1.

(17) Dikin, D. A.; Stankovich, S.; Zimney, E. J.; Piner, R. D.; Dommett, G. H. B.; Evmenenko, G.; Nguyen, S. T.; Ruoff, R. S. *Nature*. **2007**, *448*, 457.

(18) Park, S.; An, J.; Jung, I.; Piner, R. D.; An, S. J.; Li, X.; Velamakanni; A.; Ruoff, R. S. *Nano Lett*. **2009**, *9*, 1593.

(19) Gupta, A.; Shaw, B. K.; Saha, S. K. *J. Phys. Chem. C*. **2014**, *118*, 6972.

(20) Weller, T. E.; Ellerby, M.; Saxena, S. S.; Smith, R. P.; Skipper, N. T. *Nat. Phys*. **2005**, *1*, 39.

(21) Lagrange, P.; Setton, R. New Graphite-Donor Compounds and Synthesis. In *Graphite Intercalation Compounds I*, ed. Zabel, H.; Solin, S. A. Springer-Verlag Berlin Heidelberg, New York, 1990, pp 283–304.

(22) Li, S.; Qiu, J.; Lai, C.; Ling, M.; Zhao, H.; Zhang, S. *Nano Energy*. **2015**, *12*, 224.

(23) Dosa, P. I.; Erben, C.; Iyer, V. S.; Vollhardt, K. P. C.; Wasser, I. M. *J. Am. Chem. Soc.* **1999**, *121*, 10430.

(24) For the catalytic effect of metals on decomposition products of endothermic compounds see ref: J. Am. Chem. Soc., Vol. 121, No. 44, 1999.

(25) Zhang, N.; Zhang, J.-Y.; Jia, Q.-X.; Deng, W.; Gao, E.-Q. *RSC Adv*. **2015**, *5*, 70772.

(26) Qin, T.; Gong, J.; Ma, J.; Wang, X.; Wang, Y.; Xu, Y.; Shen, X.; Zhu, D. *Chem. Commun*. **2014**, *50*, 15886.

(27) Pal, T. K.; Katoch, R.; Garg, A.; Bharadwaj, P. K. *Cryst. Growth Des*. **2015**, *15*, 4526.

(28) Zhang, N.; Zhang, J.-Y.; Jia, Q.-X.; Deng, W.; Gao, E.-Q. *RSC Adv*. **2015**, *5*, 70772.

(29) Sheldrick, G. M. *Acta Cryst*. **2008**, *A64*, 112.

(30) Spek, A. L. *Acta Cryst*. **2009**, *D65*, 148.

CHAPTER V

Rendering non-energetic microporous coordination polymers explosive[**]

5.1 Introduction

Explosives and related energetic materials, such as propellants and pyrotechnics, have a large amount of stored chemical energy that can be released with a suitable initiation event.[1,2] Recently, coordination polymers (CPs) have emerged as promising candidates for the synthesis of energetic materials with high energy density.[3-19] The numerous coordination modes of nitrogen-rich linkers can be combined with metal nodes to generate crystalline 1D, 2D, and 3D energetic CPs. The current state of the art in energetic CP design and properties has been reviewed[20-22] and performance is promising, and on par with current energetic materials by some metrics; however these materials suffer from a lack of tunability where the composition is dictated by synthesis, similar to traditional energetic materials. Moreover, oxygen deficiency plagues these materials and few have demonstrated permanent microporosity.[20-22] This is unfortunate as there is potential to make oxygen-balanced materials if oxidizer can be infiltrated into a fuel rich porous structure. An extreme of this, which we explore here, would be to use a guest that has such a positive oxygen balance that fuel rich, non-energetic, frameworks can be used. Microporous coordination polymers (MCPs) have been extensively used to encapsulate guest molecules and therefore the use of these fuel rich MCP scaffolds as hosts for the adsorption of oxidants, should sufficient porosity be available, is viable.[23,24] It is hypothesized that the fuel-rich, non-energetic, MCPs can serve as host frameworks for the incorporation of oxidant guest molecules leading to the molecular scale mixing of fuel and oxidizer. The adsorption of oxidants tetranitromethane (TNM) and hexanitroethane (HNE) into MOF-5 (Metal-Organic Framework-5,[25] $[Zn_4O(BDC)_3]_n$;

[**] McDonald, K. A.; Bennion, J. C.; Leone, A. K.; Matzger, A. J., *Chem. Commun.*, **2016**, *52*, 10862. Adapted by permission of The Royal Society of Chemistry.

BDC = 1,4-benzenedicarboxylate) is demonstrated here to be successful for the development of energetic materials based on the intimate mixing of fuel and oxidant species (Figure 5.1). Furthermore, when considering the oxygen balance of MOF-5 (-93.6%), the inclusion of oxidizing guest molecules, with positive oxygen balances, such as TNM (OB = +49.0%) and HNE (OB = +42.7%), will lead to an energetic material with an overall more neutral oxygen balance compared to current explosives. MOF-5 with adsorbed TNM or HNE is referred to hereafter as MOF-5-TNM and MOF-5-HNE, respectively.

5.2 Results and Discussion

Initially TNM was loaded into MOF-5 by direct contact of liquid TNM with the porous solid. Coating of the outer crystal surfaces resulted in uncontrolled TNM incorporation. For MOF-5-HNE, solid HNE dissolved in pentane was mixed with MOF-5 and the solvent was allowed to evaporate in an open vial at room temperature. This method of loading resulted in a physical mixture of HNE crystals with MOF-5-HNE that had a loading of up to 50 wt%. In order to circumvent the problem of solvent competing with the oxidant for adsorption, vapor diffusion, in the case of MOF-5-TNM, and sublimation, in the case of MOF-5-HNE, were investigated and were found to effectively control composition of the composite. MOF-5-TNM was prepared by placing a 4 mL vial containing MOF-5 (10.0 mg) into a 20 mL vial containing TNM (0.20 mL). The vial was allowed to sit, sealed, at room temperature. MOF-5-HNE was synthesized by placing HNE (25.0 mg) into a Schlenk flask, which also contained a small boat of MOF-5 (10.0 mg). The Schlenk flask was placed under vacuum and the HNE was allowed to sublime and adsorb into the pores of MOF-5. Powder X-ray diffraction (PXRD) shows that the structural integrity of the MCP was retained upon loading of the TNM and HNE oxidants (Figures 5.2 and 5.3).

Thermogravimetric analysis (TGA) was used to quantify the amount of TNM and HNE adsorbed into the MCP and to monitor the amount of oxidant adsorbed as a function of loading time. In addition, the data obtained from TGA experiments was used to calculate the oxygen balance of the loaded MOF-5. As expected, the weight percent of each oxidant loaded into MOF-5 increases with time until the pores are saturated. For

MOF-5-TNM, it was determined that the MCP could adsorb as much as ~55 wt% TNM in as quickly as 3 hours (Figure 5.5a). This translates to an oxygen balance of -14.6 % and can be compared to the oxygen balance of the guest free MOF-5 of -94 %. For MOF-5-HNE, the adsorption of HNE into MOF-5 saturated at ~62 wt%; this translates to an oxygen balance of -8.70 % (Figure 5.5b). The oxygen balances of the composite materials are neutral compared to many existing and commonly used explosive materials (TNT = -73.9 %, RDX/HMX = -21.6 %). In addition, the oxygen balances are among the best reported for energetic coordination polymer-based materials.

In order to quantify the retention of the oxidant guests in the MCP host, vapor pressure of the oxidants were evaluated before and after loading into the MCP. These experiments were carried out by loading the MCP, saturated with oxidant, into crimped aluminum DSC pans with 50 μm holes in their lids. The mass loss of the samples was monitored at 30 °C for MOF-5-TNM and 45 °C for MOF-5-HNE under a 30 mL/min flow of nitrogen gas for 10 hours. Compared to the pure oxidants, the composites exhibit a reduced rate of mass loss, indicating that the volatility of the oxidant is suppressed upon adsorption into the MCP. The volatility was suppressed by ~75× for the MOF-5-TNM system and ~3× for MOF-5-HNE system (Figures 5.6 and 5.7). The suppression of oxidant volatility can be advantageous for improved handling and stability of the energetics.

Sensitivity measurements were conducted to quantify the effects of oxidant adsorption on the impact sensitivity of the resulting MCP-oxidant materials. The measurements were performed using a small-scale drop height apparatus, which utilizes non-hermetic DSC pans to encase a small amount of sample (2.00 mg ± 10%) onto which a 5 lb weight was dropped from a pre-measured distance (see ref 26 for details about the drop height aparatus and Brusten analysis).[26] The oxidant molecules TNM and HNE exhibit a $D_{50}h$, or 50 % probability of detonation, of 34 and 21 cm, respectively on this apparatus whereas MOF-5, as expected, shows no energetic behavior up to the maximum drop height of the apparatus. Adsorption of these oxidants into MOF-5 results in energetics with $D_{50}h$ values of 17 and 7 cm for MOF-5-TNM and MOF-5-HNE, respectively (Figure 5.8). This would classify these materials as primary explosives, or energetics which are extremely sensitive to external stimuli (impact sensitivity greater

than or equal to pentaerythritol tetranitrate, PETN[27]), and can be contrasted with insensitive energetics, known as secondary explosives (Figure 5.8). Here, HNE, a secondary energetic, is transformed to a primary by adsorption into MOF-5. TNM, lying close to the cutoff between primary and secondary energetics, is rendered more sensitive upon adsorption into MOF-5 (example of detonation of MOF-5-TNM by impact shown in Figure 5.8b). This leads to the question of why the sensitivity of the composites increases relative to the individual components, in contrast to previous studies where the sensitivity of the energetic guest is reduced upon encapsulation into the MCP.[19] The increase in sensitivity can be attributed to a decrease in the activation energy for exothermic decomposition upon loading the TNM/HNE oxidants into MOF-5; this follows from the greater exothermicity of the reaction consistent with the Bell-Evans Polanyi principle.[28] As the energetic content increases, the sensitivity is also expected to increase. Considering the facile synthesis by which these primaries can be produced, and bearing in mind the safer transportation of the individual components during shipment, these are an attractive class of on-demand primaries.

In order to evaluate the performance of the saturated MCP-oxidant energetic materials, differential scanning calorimetry (DSC) was employed. Initial experiments were performed using standard hermetically sealed aluminum pans and it was observed that the heat evolution increased as a function of increasing heating rate for both MOF-5-TNM and MOF-5-HNE. It was hypothesized that this heating rate dependence was due to desaturation of oxidant from the MCP framework as a function of temperature. Furthermore, the pressure generated by thermal decomposition of both the oxidants and loaded MCPs exceeded the pressure limit in the sealed pans and, therefore, gas escape from the DSC pans resulted, even using sub-milligram quantities of sample. This problem was overcome with stainless steel, high-pressure, DSC pans. The thermal lag, however, at higher ramp rates prevented the use of the high-pressure pans at ramp rates sufficiently fast to avoid oxidant desaturation. In order to show that incorporation of the oxidants into MOF-5 results in an increased heat release, excess oxidant was added to the DSC pans along with the loaded MCPs resulting in equilibration of oxidant vapor pressure in the pan therefore preventing desaturation of the oxidants from the pores. We theorize that if MOF-5 is not providing any additional heat, then the heat released for the loaded MOF-5

with excess oxidant would decrease relative to the neat oxidant due to the additional mass of MOF-5 in the pan. Thermal decomposition of neat TNM results in the generation of 1146 J g^{-1}. The thermal decomposition of MOF-5-TNM by DSC results in a heat release of 690 J g^{-1} (Figures 5.10 and 5.11). This observation is consistent with TNM escaping from the framework, under these conditions, and decomposing outside of MOF-5. When a small excess of TNM is added to a MOF-5-TNM crystal inside the high pressure DSC pan, the heat is markedly increased from 1146 J g^{-1}, for neat TNM, to 5749 J g^{-1}, for MOF-5-TNM with excess TNM. We attribute the increased heat released, to the oxidant, which is able to react with MOF-5 since escape from the framework is not as favorable under an excess TNM atmosphere. Moreover, the clear shift of the peak temperature in the DSC thermograms from 202 °C, for neat TNM, to 197 °C, for MOF-5-TNM, and associated dramatic peak sharpening is indicative of an increase in the thermal sensitivity of the material. For HNE, thermal decomposition results in a heat release of 2138 J g^{-1}, whereas MOF-5-HNE shows a heat release of 2476 J g^{-1}. This slight increase in the heat released is indicative of an exothermic reaction between MOF-5 and HNE. When excess HNE was added to a high-pressure DSC pan containing MOF-5-HNE, the heat released was increased to 4455 J g^{-1}. We theorize that partial escape of HNE from the framework is suppressed when excess HNE is added, the heat released is even more increased due to retention of HNE in the framework and therefore increased reactivity between MOF-5 and HNE. Analogous to the MOF-5-TNM case, the decomposition temperature of MOF-5-HNE is shifted to a lower temperature relative to HNE. MOF-5-HNE has a peak temperature at 135 °C which is lower than neat HNE (153 °C), indicating increased thermal sensitivity of the oxidant upon incorporation into the MOF-5 lattice. These data indicate that incorporation of the oxidants into MOF-5 leads to increased heat released upon thermal decomposition of loaded MOF-5 relative to the neat oxidants and is consistent with a the framework acting as a fuel for the oxidizing energetic guest.

In light of the observed heating rate dependence, analysis of the decomposition products was performed on residue collected after thermal initiation in the absence of excess oxidant (Figures 5.12-5.15). We hypothesize that the volatility of TNM adsorbed into MOF-5 is not sufficiently suppressed to result in an efficient reaction between fuel and oxidant, particularly upon thermal initiation. Raman spectroscopy and PXRD of the

crystals collected after thermal initiation confirms that the MOF-5 crystal structure is still intact (Figures 5.12 and 5.13). Analogous to the previously discussed decomposition product analysis, drop test pans were opened and analysis of the residue coating the inside of the pan was performed to highlight the differences between these materials behavior to initiation by impact and thermal initiation methods (Figures 5.16 and 5.17). For MOF-5-TNM the decomposition product by impact was determined by Raman spectroscopy to be a mixture of carbon and un-reacted MOF-5 (Figure 5.16). These data demonstrate that MOF-5-TNM does not undergo efficient reaction by impact or thermal initiation under the conditions explored, and this is doubtless due in part to the very small scale of the tests. HNE, having much lower volatility than TNM is likely to remain intimately mixed for efficient reaction with MOF-5. This is evident by noting that the heat released for MOF-5-HNE alone is higher than pure HNE in contrast to TNM/MOF-5-TNM. We hypothesize that MOF-5-HNE results in a more efficient reaction between fuel and oxidant upon both impact and thermal initiation. MOF-5-HNE is decomposed substantially into a mixture of carbon and zinc oxide upon thermal initiation; this was confirmed by Raman spectroscopy and PXRD (Figures 5.14 and 5.15). The same was shown to be true for MOF-5-HNE initiated by impact (Figure 5.17).

The performance of an energetic material can either be determined experimentally with large-scale detonations or through the use of a thermochemical computational codes that predict detonation properties (velocity, pressure, etc.). Cheetah 7.0,[29] which utilizes both chemical (molecular formula/density) and thermodynamic (heat of formation) properties to calculate the performance of an energetic material, was employed here (see Experimental Methods section). Both MOF-5-TNM (5243 m/s) and MOF-5-HNE (6160 m/s) are predicted to have detonation velocities slightly below that of their pure oxidants (6194 m s^{-1} for TNM and 7118 m s^{-1} for HNE). When compared to commonly used primary energetic materials, lead azide (7244 m s^{-1}) and lead styphnate (6500 m s^{-1}), both MOF-5-TNM and MOF-5-HNE have good performance. Considering the decreased toxicity of these composite materials, these calculations highlight the potential for use of these MCP energetic composites as replacements for lead based primaries; however, there are other factors, in conjunction with detonation velocity and sensitivity that need to be considered. Future work may require a direct comparison of how the physical and

chemical properties of the composites compares to initiators such as lead azide and lead styphnate.

5.3 Conclusions

Employing non-energetic MCPs as hosts (fuel) for the adsorption of oxidant molecules enables the intimate and molecular scale mixing of fuel and oxidizer on a level that is not commonly achievable in traditional energetic mixtures. The adsorption of the oxidants TNM and HNE into MOF-5 results in increased heat released upon decomposition, which shows potential for utilization of this method as a platform to develop high-performance energetic materials. Moreover, the increased sensitivity of MOF-5-TNM and MOF-5-HNE suggests that these materials may function as replacements of lead based initiators. This simple strategy can be applied to other MCPs and oxidants for the further development of energetic materials with high density, desirable oxygen balance, and increased heats of detonation. We are extending this work to investigate an array of MCP-oxidant mixtures to understand how to develop both high-performance primary and high-performance secondary energetic materials based on the adsorption of oxidants into non-energetic MCPs.

5.4 Experimental Methods

Caution*: Although no unplanned detonations were encountered during this work, TNM, HNE, MOF-5-TNM and MOF-5-HNE are all dangerous explosives. Proper safety practices and equipment was used to prevent an explosion due to friction, heat, static shock, or impact. Be aware that the potential for severe injury exists if these materials are handled improperly.*

Synthesis of MOF-5. MOF-5 was synthesized by a method previously reported in the literature.[30]

Activation. Samples were activated by exposure to a dynamic vacuum (10^{-2} Torr) for 24 hours.

Synthesis of Hexanitroethane (HNE). HNE was synthesized by a method previously reported in the literature.[31]

MOF-5-TNM. For the adsorption of TNM, 10.0 mg of MOF-5 was weighed into a 4 mL vial in an N_2 filled glovebox. Outside of the glovebox, TNM (0.20 mL) was added to a 20 mL scintillation vial, capped, and allowed to come to equilibrium with the atmosphere in the vial. The 4 mL vial containing the MOF-5 was removed from the glovebox, opened to air, inserted into the 20 mL vial containing TNM, and capped. TNM was allowed to vaporize, come to equilibrium with the chamber, and adsorb into MOF-5 for variable amounts of time. To stop the adsorption, the 4 mL vial (containing MOF-5-TNM) was removed from the chamber and capped.

MOF-5-HNE. For the adsorption of HNE, 10.0 mg of MOF-5 was weighed into a 4 mL vial in a N_2 filled glovebox. The sample was then removed from the glovebox and transferred to a small aluminium boat. This boat was inserted into a schlenk tube containing 25.0 mg of HNE. The schlenk tube was connected to a vacuum line and carefully evacuated to 50 mTorr, then closed. HNE was allowed to sublime in the chamber and adsorb into MOF-5 for variable amounts of time. The adsorption was stopped by releasing the vacuum in the chamber, the product (MOF-5-HNE) was collected in a 4 mL vial, and capped.

Powder X-ray diffraction. Powder X-ray diffraction (PXRD) patterns were collected using a Rigaku R-axis Spider diffractometer with an image plate detector and graphite monochromated Cu-Kα radiation (1.5406 Å). The patterns were collected with the tube operating at 40 kV and 44 mA. Images were collected in transmission mode with χ set at 45°, ϕ rotating at 10°/min, and ω oscillating between 5° and 50° to minimize the effects of preferred orientation. Integration of the resulting images was performed in the AreaMax (2.0) software package with a step size of 0.1 in 2θ.

Gas sorption measurements. Sorption experiments were carried out using a NOVA *e*-series 4200 surface area analyser (Quantachrome Instruments, Boynton Beach, Florida, USA). N_2 (99.999%) was purchased from Cryogenic Gases and used as received. For N_2 measurements, a glass sample cell was charged with ~20 mg sample and analysed at 77 K. Sorption isotherms were collected in the NOVAwin software.

Thermogravimetric Analysis. A TA Instruments Q50 TGA was used to obtain thermogravimetric data in which the analyte was heated from ~25 °C to 600 °C at a rate of 10 °C/min and analysed in a platinum pan under flowing nitrogen.

Vapor pressure measurements. Vapour pressure experiments (shown in Figures 5.6 and 5.7) were performed as previously described.[26] Here, the TGA was heated to 30 °C for MOF-5-TNM and 45 °C for MOF-5-HNE and held for 10 hours. In this case, the degree by which the vapour pressure was suppressed was calculated by dividing the slope of the weight loss of the pure oxidant by the slope of weight loss of the MCP-oxidant mixture.

Differential Scanning Calorimetry. Thermograms of each sample were recorded on a TA Instruments Q10 DSC. All experiments were run using a Tzero™ DSC High Pressure Capsule Kit and studied under a nitrogen purge with a heating rate of 20 °C/min, covering the temperature range of ~100 °C to ~300 °C. Calibration of the instrument was performed using an indium standard. Thermograms were analysed using TA Universal Analysis 2000, V 4.5A.

Raman Spectroscopy. Raman spectra were obtained using a Renishaw inVia Raman microscope equipped with a CCD detector, 785 nm laser, 1200 lines/mm grating, and 65 μm slit was used for collecting data. Spectra were collected using a static scan mode and analysed using the Wire 4.2 software package. Calibration of the instrument was performed using a silicon standard for all experiments.

Cheetah Calculations

The values that were important for evaluating the performance of the oxidants (TNM/HNE), MOF-5, and the composite materials were density, molecular formula, and heat of formation.[32] These values were plugged into Cheetah 7.0 and used to determine the oxygen balance and detonation velocity. The relative ratios of the oxidants to MOF-5 were evaluated using TGA and used to determine the molecular weight and empirical formula of the composite materials. The heat of formation of the oxidants were available through Cheetah and the MOF-5 heat of formation was taken from the literature.[32] The total heat of formation for the composite was estimated as shown below:

$$\Delta Hf{-}composite = \Delta Hf{-}oxidant + \Delta Hf{-}MOF(MW\ contribution\ of\ MOF\ from\ composite/MW\ of\ pure\ MOF)$$

The density of the composites was determined using the following calculation:

$$Density\ (g\ cm^{-3}) = density\ of\ MOF + [density\ of\ MOF \times ratio\ of\ oxidant\ to\ MOF]$$

5.5 Figures

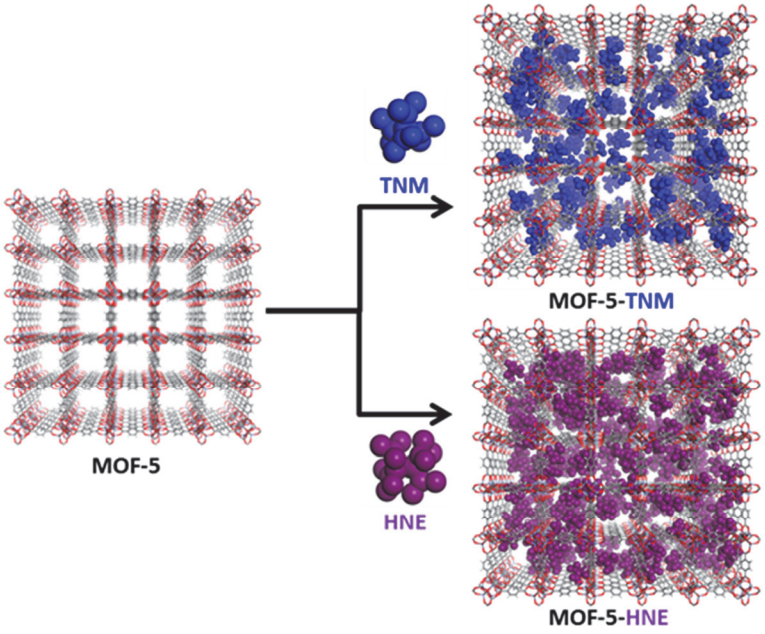

Figure 5.1. Illustration of the adsorption of TNM (blue) and HNE (purple) into MOF-5 resulting in MOF-5-TNM and MOF-5-HNE. See section 5.4 for more details.

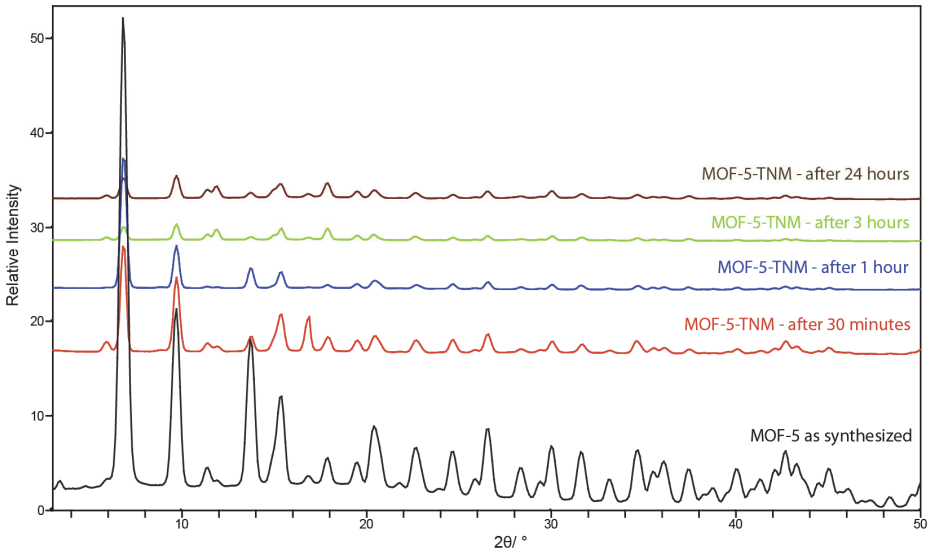

Figure 5.2. Powder X-Ray diffraction patterns collected to monitor the structural integrity of MOF-5 as a function of TNM loading – As synthesized MOF-5 (black), MOF-5-TNM after 30 minutes (red), MOF-5-TNM after 1 hour (blue), MOF-5-TNM after 3 hours (green), and MOF-5-TNM after 24 hours (brown).

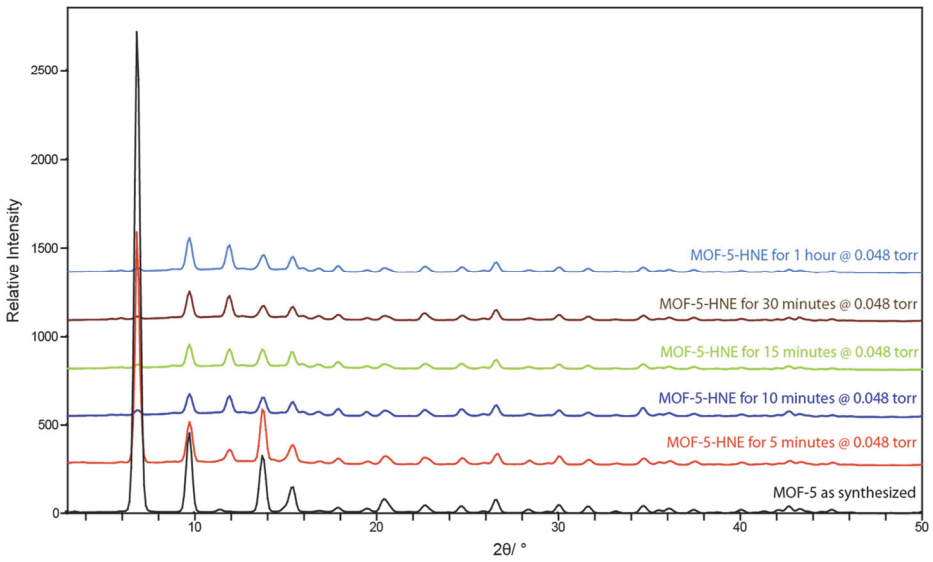

Figure 5.3. Powder X-Ray diffraction patterns collected to monitor the structural integrity of MOF-5 as a function of HNE loading at 0.048 torr – As synthesized MOF-5 (black), MOF-5-HNE after 5 minutes (red), MOF-5-HNE after 10 minutes (blue), MOF-5-HNE after 15 minutes (green), MOF-5-HNE after 30 minutes (brown), and MOF-5-HNE after 1 hour (light blue).

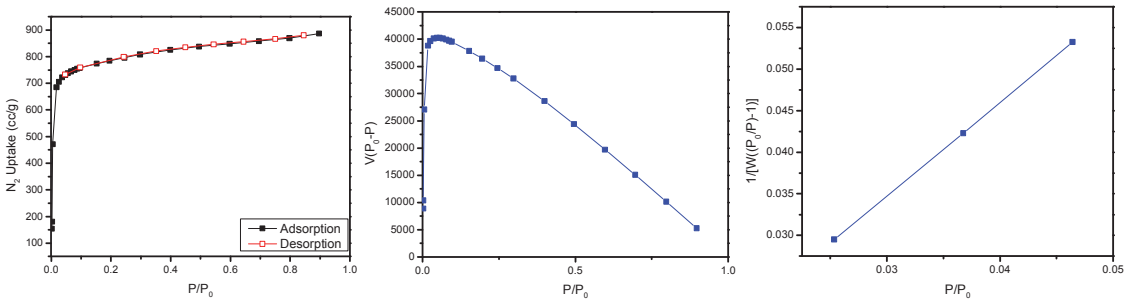

Figure 5.4. (left) Nitrogen sorption isotherm collected on MOF-5, (middle) Consistency criterion plot for determining the P/P_o range for BET analysis,[33] and (right) BET plot used to calculate the surface area of MOF-5 (3087 m^2g^{-1})

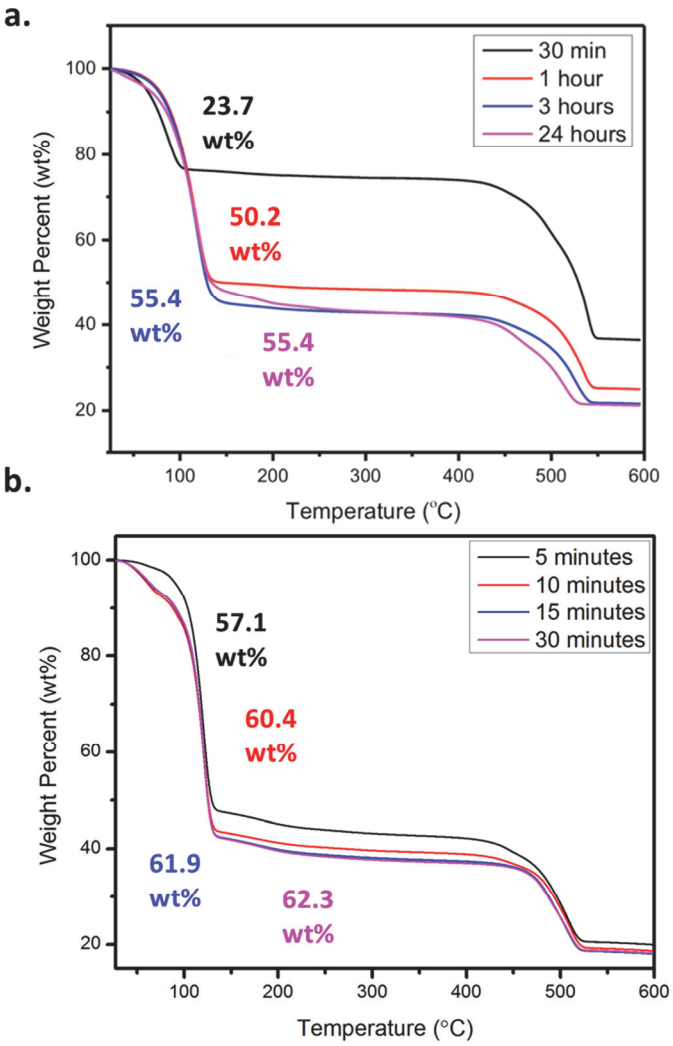

Figure 5.5. Thermogravimetric Analysis (TGA) of the adsorption of TNM (a) and HNE (b) into MOF-5 carried out for different periods of time.

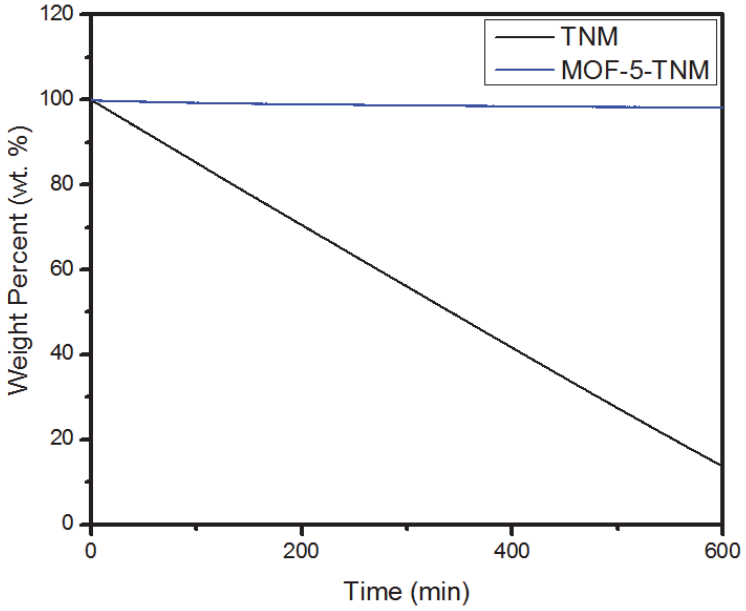

Figure 5.6. Plot of the weight percent loss as a function of time for TNM (black) and MOF-5-TNM (blue).

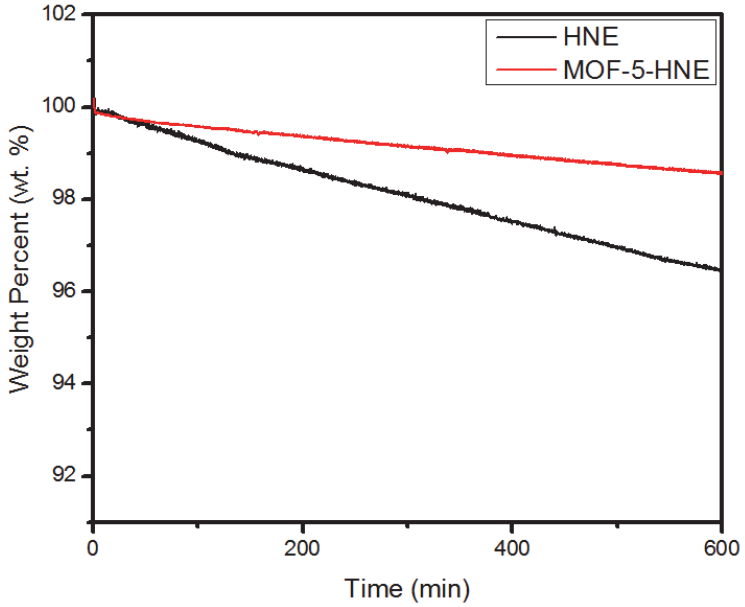

Figure 5.7. Plot of the weight percent loss as a function of time for HNE (black) and MOF-5-HNE (red).

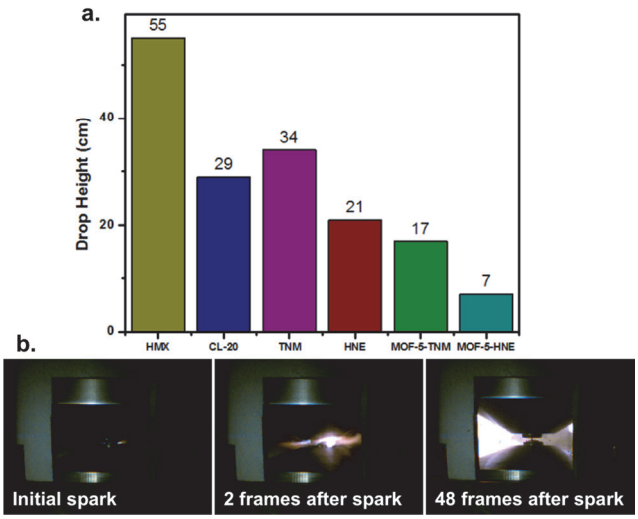

Figure 5.8. (a) Graph comparing the sensitivity measurements for the determination of the D50h, or 50 % probability of detonation, for HMX, CL-20, TNM, HNE, MOF-5-TNM, and MOF-5-HNE and (b) High speed video of the drop test of MOF-5-TNM in an aluminum pan at 35,000 frames per second showing the detonation from spark to 48 frames later (full video available).

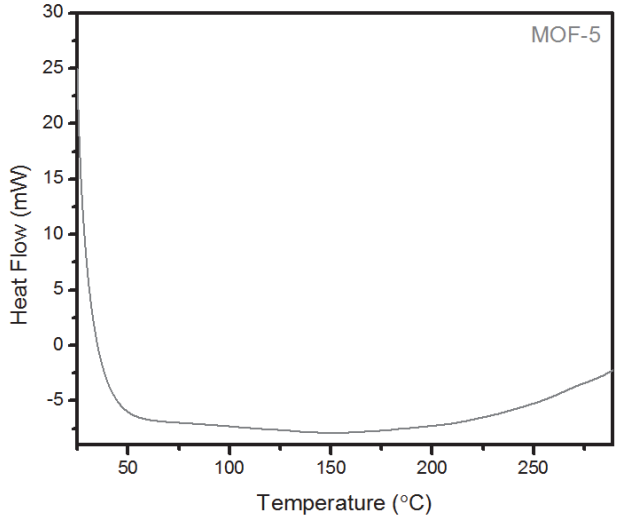

Figure 5.9. DSC of thermogram of MOF-5 at 20 °C min^{-1} in the high-pressure pans

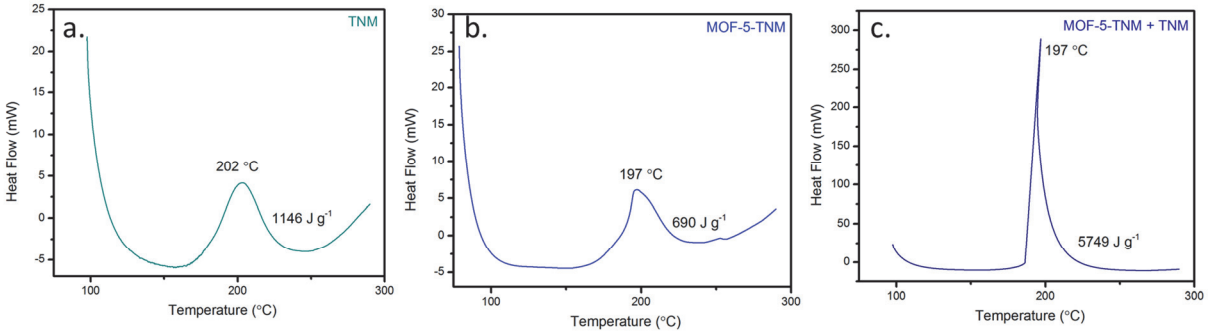

Figure 5.10. DSC of thermograms of TNM (0.754 mg), MOF-5-TNM (1.01 mg), and MOF-5-TNM (0.650 mg) with excess TNM (0.786 mg) at 20 °C min^{-1} in the high-pressure pans

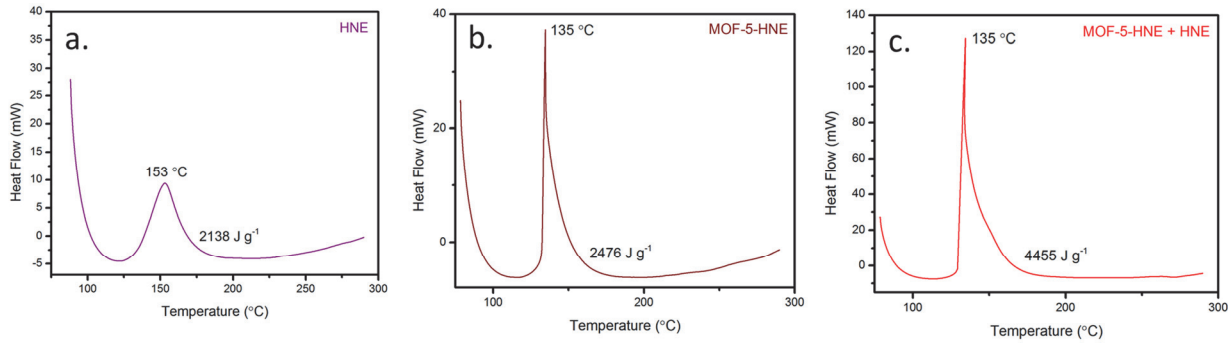

Figure 5.11. DSC of thermograms of HNE (0.460 mg), MOF-5-HNE (0.460 mg), and MOF-5-HNE (0.426 mg) with excess HNE (0.514 mg) at 20 °C min^{-1} in the high-pressure pans

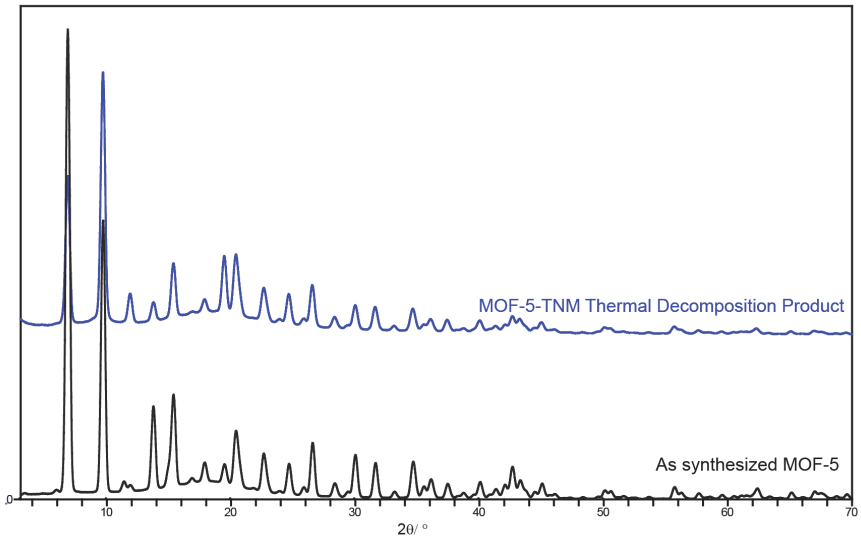

Figure 5.12. PXRD of as synthesized MOF-5 (black) and the thermal decomposition product of MOF-5-TNM (blue) showing a retention of the crystal structure after thermal initiation

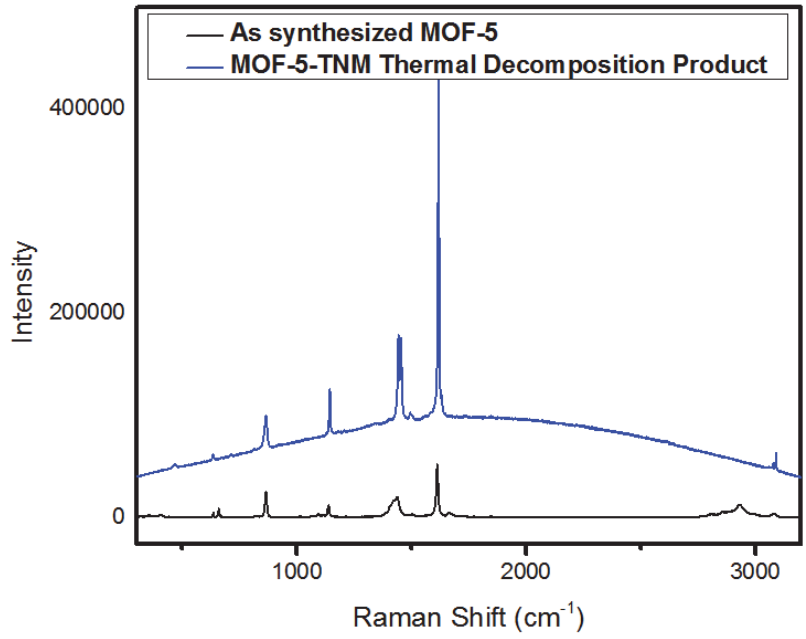

Figure 5.13. Raman Spectra of as synthesized MOF-5 (black) and the thermal decomposition product of MOF-5-TNM (blue)

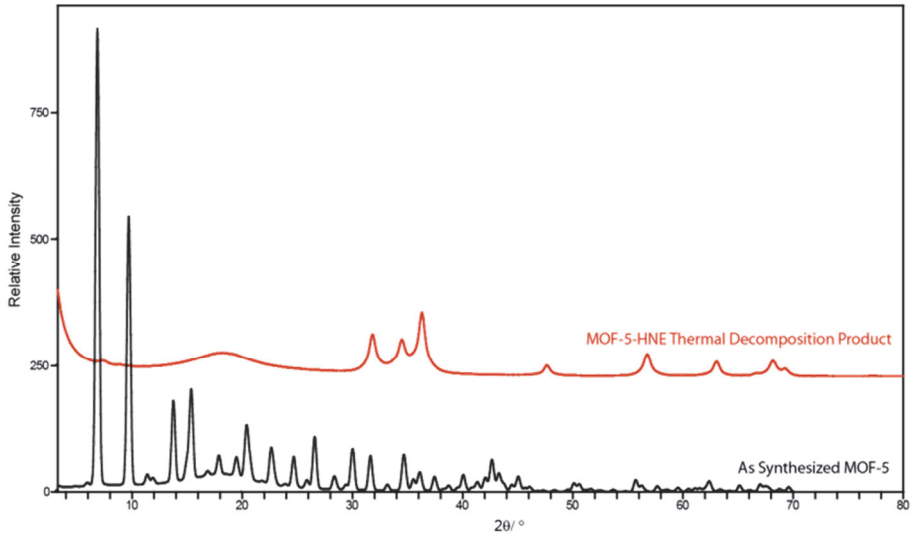

Figure 5.14. PXRD of as synthesized MOF-5 (black) and the thermal decomposition product of MOF-5-HNE (red) showing the conversion of MOF-5-HNE to a mixture of carbon and zinc oxide

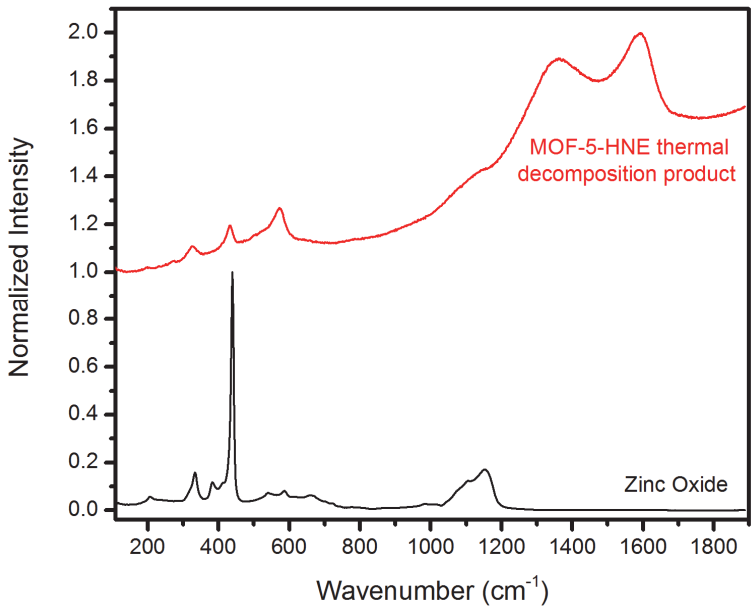

Figure 5.15. Raman spectra of zinc oxide (black) and the thermal decomposition product of MOF-5-HNE (red) showing the conversion of MOF-5-HNE to a mixture of carbon and zinc oxide

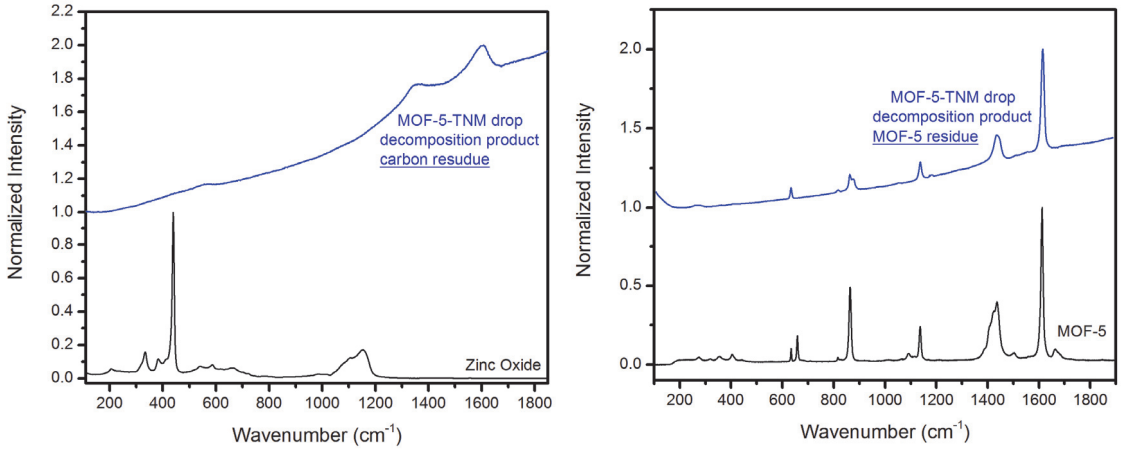

Figure 5.16. Raman Spectra of the impact decomposition products for MOF-5-TNM: (left) MOF-5-TNM decomposition product (carbon residue, blue) and Zinc oxide (black) for comparison and (right) MOF-5-TNM decomposition product (MOF-5 residue, blue) and MOF-5 for reference (black).

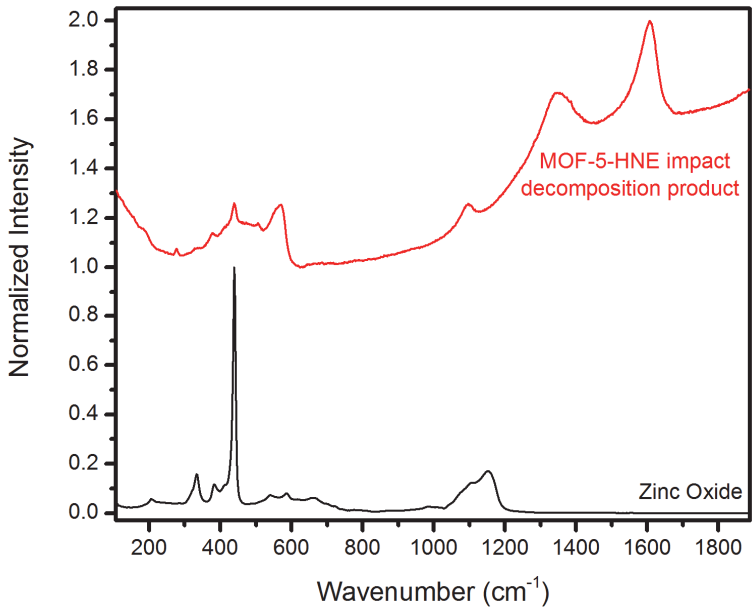

Figure 5.17. Raman spectra of zinc oxide (black) and the decomposition product of MOF-5-HNE (red) after impact showing the conversion of MOF-5-HNE to a mixture of carbon and zinc oxide

5.6 References

(1) Steinhauser, G.; Klapötke, T.M.*Angew. Chem. Int. Ed*. **2008**, *47*, 3330.

(2) Meyer, R.; Köhler, J.; Homburg, A. Explosives, Wiley-VCH, Weinheim, 2007, p. 131.

(3) Li, S.; Wang, Y.; Qi, C.; Zhao, X.; Zhang, J.; Zhang, S.; Pang, S. *Angew. Chem. Int. Ed.* **2013**, *52*, 14031.

(4) Zhang, Q.; Shreeve, J. M. *Angew. Chem. Int. Ed*. **2014**, *53*, 2540.

(5) Blair, L. H.; Colakel, A.; Vrcelj, R. M.; Sinclair, I.; Coles, S. J. *Chem. Commun.* **2015**, *51*, 12185.

(6) Bushuyev, O. S.; Peterson, G. R.; Brown, P.; Maiti, A.; Gee, R.H.; Weeks, B. L.; Hope-Weeks, L. J. *Chem. Eur. J.* **2013**, *19*, 1706.

(7) Zhang, S.; Liu, X.; Yang, Q.; Su, Z.; Gao, W.; Wei, Q.; Xie, G.; Chen, S.; Gao, S. *Chem. Eur. J.* **2014**, *20*, 7906.

(8) Lin, J.-D.; Wang, S.-H.; Cai, L.-Z.; Zheng, F.-K.; Guo, G.-C.; Huang, J.-S. *Cryst. Eng. Comm* **2013**, *15*, 903.

(9) Wang, S.-H.; Zheng, F.-K.; Wu, M.-F.; Liu, Z.-F.; Chen, J.; Guo, G.-C.; Wu, A. Q. *Cryst. Eng. Comm*. **2013**, *15*, 2616.

(10) Feng, Y.; Liu, X.; Duan, L.; Yang, Q.; Wei, Q.; Xie, G.; Chen, S.; Yang, X.; Gao, S.; *Dalton Trans*. **2015**, *44*, 2333.

(11) Jiang, C.; Yu, Z.; Wang, S.; Jiao, C.; Li, J.; Wang, Z.; Cui, Y. *Eur. J. Inorg. Chem.* 2004, ***2004***, 3662.

(12) Liu, X.; Gao, W.; Sun, P.; Su, Z.; Chen, S.; Wei, Q.; Xie, G.; Gao, S. *Green Chem*. **2015**, *17*, 831.

(13) Bushuyev, O. S.; Brown, P.; Maiti, A.; Gee, R. H.; Peterson, G. R.; Weeks, B. L.; Hope-Weeks, L. J. *J. Am. Chem. Soc.* **2012**, *134*, 1422.

(14) Shunguan, Z.; Youchen, W.; Wenyi Z.; Jingyan, M. *Propellants Explos. Pyrotech.* **1997**, *22*, 317.

(15) Yang, L.; Wu, B.; Zhang, T.; Liu, Z.; Zhang, J. *Propellants Explos. Pyrotech*. **2010**, *35*, 521.

(16) Wang, S.-W.; Yang, L.; Feng, J.-L.; Wu, B.-D.; Zhang, J.-G.; Zhang T.-L.; Zhou, Z.-N. *Z. Anorg. Allg. Chem.* **2011**, *637*, 2215.

(17) Wang, Q.; Feng, X.; Wang, S.; Song, N.; Chen, Y.; Tong, W.; Han, Y.; Yang, L.; Wang, B. *Adv. Mater.* **2016**, *28*, 5837.

(18) Tang, Y.; He, C.; Mitchell, L. A.; Parrish, D. A.; Shreeve, J. M. *Angew. Chem. Int. Ed.* **2016**, *55*, 5565.

(19) Nelson, A. P.; Trivedi, N. J. US8197619B1, 2012.

(20) McDonald, K. A.; Seth, S.; Matzger, A. J. *Cryst. Growth Des.* **2015**, *15*, **5963**.

(21) Zhang, S.; Yang, Q.; Liu, X.; Qu, X.; Wei, Q.; Xie, G.; Chen, S.; Gao, S. *Coord. Chem. Rev*. **2016**, *307*, 292.

(22) Zhang, J.; Shreeve, J. M. *Dalton Trans*. **2016**, *45*, 2363.

(23) Allendorf, M. D.; Foster, M. E.; Léonard, F.; Stavila, V.; Feng, P. L.; Doty, F. P.; Leong, K.; Ma, E. Y.; Johnston, S. R.; Talin, A. A. *J. Phys. Chem. Lett.* **2015**, 6, 1182.

(24) Cui, Y.; Li, B.; He, H.; Zhou, W.; Chen, B.; Qian, G. *Acc. Chem. Res*. **2016**, *49*, 483.

(25) Li, H.; Eddaoudi, M.; O'Keeffe, M.; Yaghi, O. M. *Nature* **1999**, *402*, 276.

(26) Landenberger, K. B.; Bolton, O.; Matzger, A. J. *J. Am. Chem. Soc.* **2015**, 137, 5074.

(27) Manner, V. W.; Tappan, B. C.; Scott, B. L.; Preston, D. N.; Brown, G. W. *Cryst. Growth Des.* **2014**, *14*, 6154.

(28) Roy, S.; Goedecker, S.; Hellmann, V. *Phys. Rev. E*. **2008**, *77*, 056707.

(29) Sandia JCZS product library revision 32 of Cheetah 7.0 was used for the calculations.

(30) Li, H.; Eddaoudi, M.; O'Keeffe, M.; Yaghi, O. M. *Nature* **1999**, *402*, 276.

(31) Golod, E. L.; Bagal, L. I. *Журнал органической химии*, **1994**, *30*, 29.

(32) Hughes, J. T.; Navrotsky, A. *J. Am. Chem. Soc.* **2011**, 133, 9184.

(33) Walton, K. S.; Snurr, R. Q. *J. Am. Chem. Soc.* **2007**, *129*, 8552.

CHAPTER VI

Conclusions and Outlook

Metal-organic frameworks (MOFs) represent a promising class of functional porous polymeric materials that have seen immense research attention in the last few decades. The research conducted herein presents novel methods for the development of hybridized composite materials (Chapters 2 and 3). These composite materials show promise to combat some of the commonly known drawbacks of MOFs such as difficult processability, organic phase immiscibility, and poor hydrolytic stability. Additionally, the studies presented herein also provide a fundamental understanding of the effects of coordination polymerization on the decomposition pathway of MOFs composed of nitrated-aromatic energetic linkers. Nitrated-aromatic motifs are commonly observed in traditional molecular organic energetics; however, most energetic coordination polymers (CPs) and MOFs reported thus far in the literature are composed of nitrogen rich heterocycles (Chapter 4). In the aforementioned study, the concept of intimate mixing of copper and nitrated linker in the MOF resulting in efficient reactivity during decomposition leads to the development of a new method to render non-energetic, fuel-rich MOFs explosive (Chapter 5).

The hybridization of MOFs with polymers has led to the development of many novel approaches to improve upon the drawbacks of this class of materials. Hybridization of highly porous and tunable MOFs with processable polymers has enabled the development of composite membranes with desirable attributes stemming from the individual components. One challenge for the fabrication of MOF-polymer hybrids is that polymer intrusion into the internal pore space is often problematic for optimal utilization of the high internal surface area of the MOF. This is important in membrane-mediated separations because the highly porous structure of MOFs can impart both selectivity and

permeability in mixed matrix membranes (MMM), where MOFs are annealed into polymer membranes. The first approach to MOF-polymer hybridization presented herein demonstrates a method for polymer coating with controlled of depth of polymer intrusion into the internal void space. This is achieved through a combination of core-shell formation and post-synthetic modification. The core-shell approach to polymer coating enables the selective tethering of initiators to the outer shell of the MOF crystal. The thickness/density of the outer shell can be controlled by the amount of crystallization time the shell is allowed to form during core-shell formation. Here, amine groups, located on the outer shell enable tethering of initiators for atom transfer radical polymerization (ATRP) of vinyl-type monomers. The co-localization of shell with polymer, shown by cross-sectional Raman mapping, demonstrates that this synthetic approach to polymer coating works to prevent polymer incorporation into the internal core. Restricting polymer grafting to the outer shell leads to a minimal surface area reduction for these composites; this reduction is primarily attributed to the additional mass of the tethered polymer chains. This route to polymer coating enables precise control over polymer incorporation. Furthermore, the tethered polymer can potentially modulate the accessibility of guests into the internal core, which may increase selectivity while also optimally increasing permeability when these hybrids are incorporated into a MMM. The hydrolytic stability of the polymer@MOF@MOF composites was shown to be minimally improved presumably due to imperfections on the shell that enable the direct diffusion of water directly into the core.

The extension of the above hybridization method to PS@IRMOF-3@MOF-5 (PS = polystyrene) revealed that polystyrene could be directly grafted from initiator-free MOF-5. This resulted in the development of a facile new approach to MOF-polymer hybridization where PS is distributed evenly throughout the MOF, as evidenced by cross-sectional Raman mapping. Thermogravimetric analysis (TGA) and N_2 sorption isotherms revealed that polymer incorporation and surface area could be precisely controlled. The even distribution of polymer throughout the MOF prevents problems with shell defects that were observed with the core-shell approach to hybridization. The hydrolytic stability of the composite after 24 hours of polymerization (MOF-5-PS-24 h) is greatly enhanced, lasting greater than 3 months at 53 % relative humidity with minimal erosion of surface

area. Contraction of the pore-size due to polymer incorporation can potentially improve the packing of guest molecules during gas adsorption. This was shown to be true when comparing the CO_2 adsorption capacity of pristine MOF-5 to the MOF-5-polystyrene composites. The CO_2 capacity of the MOF-5-PS-24 h composite is higher than pristine MOF-5 and it was later shown that the optimal reaction time to achieve the highest CO_2 capacity was 8 h. This simple protocol for MOF-polymer hybridization works for a range of MOFs, functionalized styrenes, and polymer compositions. This protocol represents a generalizable approach for facile hybridization that can be extended to a range of high performance MOFs for improvement of stability, adsorption capacity, and processability.

This thesis also introduces a recently new application of CPs and MOFs as energetic materials. Traditional examples of energetic molecules, such as 2,4,6-trinitrotoluene (TNT), contain nitrated aromatic motifs; however, the vast majority of energetic CPs and MOFs in the literature are composed of nitrogen-rich heterocycles. With increasing interest in the field of energetic CPs and MOFs, the effect of coordination polymerization on the decomposition pathway of nitrogen-rich heterocyles is becoming well understood. However, the effects of coordination polymerization on the decomposition pathway of CPs and MOFs composed of more traditional nitrated aromatic energetic linkers are not well understood. CuNbO-1, composed of copper paddlewheels and 2,2′,6,6′-tetranitro-4,4′-biphenyldicarboxylate, exhibited an unusual thermal decomposition pathway consisting of deflagration leading to anisotropic decomposition forming metal-carbon composites. Powder X-ray diffraction (PXRD) and Energy Dispersive X-ray Spectroscopy (EDS) revealed that deposited copper on the carbon was highly dispersed. Raman spectroscopy and transmission electron microscopy (TEM) revealed that the anisotropic carbon support was mostly amorphous with a small amount of graphitized carbon. This decomposition pathway differs dramatically from the decomposition of the nitro-functionalized linker alone, highlighting the catalytic effect of the metal. This was further investigated by decomposition gas analysis, which leads to the proposition that copper catalyzes the conversion of CO to CO_2 during decomposition allowing for the limited number of oxygen atoms to be used for the oxidation and more of the carbon in the material to be left as soot. The influence of the MOF structure on the anisotropic decomposition was also shown to be critical highlighting the effect of

intimate mixing on the decomposition pathway. The high dispersion of copper on the anisotropic carbon support suggests the future application of these types of materials toward the development of metal-carbon composites for heterogeneous catalysis. The high compositional tunability of MOFs can be used to generate a range of heterogeneous catalysts by this method.

The importance of intimate mixing for efficient reactivity highlighted in the study summarized above led to the development of a novel method for the synthesis of energetic MOFs. This method enables the use of the vast library of available carbon-rich MOFs to act as fuel, where pores can be infiltrated with oxidant molecules, leading to an energetic composite. Here, the non-energetic fuel and oxidant are mixed on a molecular level, which is not typically achieved in traditional energetic mixtures. As a prototype system, MOF-5 was chosen since it is commonly known to be non-energetic. Adsorption of TNM and HNE resulted in suppressed vapor pressure of these volatile guests allowing for optimal molecular mixing of fuel and oxidizer. This method results in increased heat released upon decomposition of the energetic composites. Furthermore, the composites have increased thermal and impact sensitivities when compared to the pure oxidants. MOF-5-TNM and MOF-5-HNE act as primary energetic materials. Not only does this represent a novel method for the development of high-performance energetic composites, but also this method allows for the safe transportation of the individual components that can be easily combined at the source to develop a sensitive initiator. Moreover, these materials, and other combinations of fuel and oxidizer that result in primary energetics, can potentially be used as lead-free initiators, where common primary energetics used today are lead azide and lead styphnate.